Model-based Feature Engineering of Atrial Fibrillation

Moghaddasi, Hanie

DOI
10.4233/uuid:36d20140-0563-4fef-a49b-3f548e604c6c

Publication date
2024

Document Version
Final published version

Citation (APA)
Moghaddasi, H. (2024). *Model-based Feature Engineering of Atrial Fibrillation*. [Dissertation (TU Delft), Delft University of Technology]. https://doi.org/10.4233/uuid:36d20140-0563-4fef-a49b-3f548e604c6c

Important note
To cite this publication, please use the final published version (if applicable).
Please check the document version above.

MODEL-BASED FEATURE ENGINEERING OF ATRIAL FIBRILLATION

MODEL-BASED FEATURE ENGINEERING OF ATRIAL FIBRILLATION

Dissertation

for the purpose of obtaining the degree of doctor
at Delft University of Technology
by the authority of the Rector Magnificus, Prof. dr. ir. T.H.J.J. van der Hagen,
chair of the Board for Doctorates
to be defended publicly on
Tuesday 18 June 2024 at 15:00 o'clock

by

Hanie MOGHADDASI KELISHOMI

Master of Science in Biomedical Engineering,
Amirkabir University of Technology, Tehran, Iran
born in Ghazvin, Iran

This dissertation has been approved by the promotors.

Composition of the doctoral committee:

Rector Magnificus,	chairperson
Prof. dr. ir. A.J van der Veen,	Delft University of Technology, *promotor*
Prof. dr. N.M.S de Groot,	Erasmus University Medical Center, Delft University of Technology, *promotor*
Dr. B. Hunyadi,	Delft University of Technology, *copromotor*

Independent members:

Prof. dr. ir. W.A. Serdijn	Delft University of Technology
Prof. dr. ir. A.C. Schouten	Delft University of Technology
Prof. dr. P. Laguna Lasaosa	Universidad de Zaragoza, Spain
Dr. R. Vullings	TU Eindhoven
Dr. ir. R.C. Hendriks	Delft University of Technology, reserve member

Keywords: Atrial Fibrillation, Electrocardiogram, Poincaré, Vectorcardiogram, Atrial Activity, Dominant Frequency, Electrogram, Action Potential, Body Surface Potentials, Rank Analysis, Singular Value Decomposition

This research was funded in part by the Medical Delta Cardiac Arrhythmia Lab (CAL), the Netherlands.

Printed by: Gildeprint

ISBN 978-94-6496-131-7

An electronic copy of this dissertation is available at
https://repository.tudelft.nl/.

To my parents,
for all their love and patience

To my Ali,
from whom my every heartbeat is initiated

CONTENTS

SUMMARY

Atrial Fibrillation (AF) is the most common tachyarrhythmia in the heart. Irregular RR intervals and the absence of a P wave before the QRS complex characterize AF. Although many studies have been done to detect atrial fibrillation, many aspects of this intricate disease need further analysis. AF is often diagnosed by the interpretation of multi-lead electrocardiograms (ECGs), which provide a non-invasive comprehensive evaluation of cardiac electrical activity. However, due to the poor spatial resolution of ECG recordings, the characteristics of AF cannot be fully demonstrated by using multi-lead ECG solely. Better spatial resolution is obtained by using high-resolution epicardial electrograms measured directly at the surface of the heart. The combination of multi-lead ECGs and high-resolution electrograms should provide a more detailed view of atrial fibrillation. To analyze such data, we first need to derive relevant features that can reduce the data and capture their essence. An initial aim of this research is to increase the accuracy of AF detection and identification of electropathological regions within the heart using the derived features. The ultimate goal is to (non-invasively) monitor the progression of atrial fibrillation through its subsequent stages.

In the first part of this thesis, we develop a method to monitor the progression of atrial fibrillation, aiming to improve the severity detection of AF. Analyzing multi-lead ECG allows to distinguish between short-lasting AF and long-lasting AF. Our method considers rhythmic and morphological changes, enabling severity detection of atrial fibrillation within the AF episodes. The results show a clear difference between the extracted features at different stages of AF. Moreover, these features can effectively capture the chaotic pattern noted in the ECG, both in terms of rhythm and morphology.

In the next part, to explain the chaotic pattern observed in the ECG, we go deeper from the surface of the body to the surface of the heart, and model the wavefront propagation as observed on the electrogram, affecting the initiation and maintenance of AF. We develop a feature to detect differences in action potential morphology, abnormal wavefront propagation, and conduction blocks. The feature consists of a location-dependent map based on the normalized singular values of a transformed data matrix, which is able to highlight the abnormal morphologies, inhomogeneities, and blocks in the tissue. We further designed a vest to measure electrograms and body surface potentials simultaneously, to enable the translation of the (invasive) electrogram analysis to non-invasive diagnosis. Our results show that the normalized second singular value is a promising indicator to detect AF in a multimodal measurement as well as a single modality measurement.

In the final part, we focus on the clinical application of the developed method to detect the severity of atrial fibrillation in patients with a history of AF during a sinus rhythm episode. Our results demonstrate that the spatial variation of atrial potential waveforms can be revealed by the features extracted from the singular value decomposition of the

absolute frequency spectrum of the epicardial measurements. These features show a clear difference between different stages of AF, emphasizing the action potential morphology dispersion.

SAMENVATTING

Atriumfibrillatie (AF) is de meest voorkomende tachyaritmie in het hart. Normaal gesproken begint de elektrische activiteit in het hart vanuit de sinusknoop (SA-knoop) en verspreidt zich door het weefsel. Echter, in het geval van AF, initiëren en onderhouden andere triggerpunten de elektrische activiteit in het hart, resulterend in chaotische elektrische activiteit. Onregelmatige RR-intervallen en het ontbreken van een P-golf voor het QRS-complex kenmerken AF. Hoewel er veel onderzoeken zijn uitgevoerd om atriumfibrillatie te detecteren, vereisen veel aspecten van deze complexe ziekte verder onderzoek. AF wordt gediagnosticeerd door interpretatie van meer-kanaals elektrocardiogrammen (ECG's), die een niet-invasieve uitgebreide evaluatie van de elektrische activiteit van het hart bieden. Echter, vanwege de beperkte ruimtelijke resolutie van ECG-opnamen kan het onderliggende mechanisme van AF niet volledig worden begrepen door alleen multi-lead ECG's te gebruiken. Een betere resolutie wordt verkregen door epicardiale elektrogrammen die rechtstreeks aan het oppervlak van het hart worden gemeten. Het combinatie van multi-lead ECG's en hoge-resolutie elektrogrammen zouden een beter begrip van het mechanisme van atriumfibrillatie moeten opleveren. Om zulke data te analyseren moeten we die data eerst samenvatten door middel vanrelevante kenmerken die de hoeveelheid data reduceren maar hun essentie bewaren. Een eerste doel hiervan is om de nauwkeurigheid van de detectie van AF en de identificatie van elektropathologische gebieden binnen het hart te vergroten. Uiteindelijk willen we een (niet-invasieve) methode om de voortgang van AF te kunnen monitoren.

In het eerste deel ontwikkelen we een methode om de progressie van atriumfibrilleren te monitoren, met als doel de detectie van de ernst van AF te verbeteren. Het analyseren van multi-lead ECG stelt ons in staat om een onderscheid tussen kortdurende AF en langdurige AF te maken. Onze methode houdt rekening met ritmische en morfologische veranderingen, waardoor de ernst van atriale fibrillatie binnen de AF-episodes kan worden gedetecteerd. De resultaten laten een duidelijk verschil zien tussen de geëxtraheerde kenmerken in verschillende stadia van AF.

Om het chaotische patroon dat in het ECG wordt waargenomen te verklaren, gaan we in de volgende stap dieper van het oppervlak van het lichaam naar het oppervlak van het hart, en modelleren de voortplanting van de contractiegolf, die de initiatie en het behoud van AF beïnvloedt. We ontwikkelen een kenmerk die de verschillen in actiepotentiaalmorfologie, abnormale golffrontvoortplanting en geleidingsblokken kan samenvatten. Dit kenmerk is een locatieafhankelijke kaart gebaseerd op de genormaliseerde singuliere waarden van een getransformeerde datamatrix, waarmee abnormale morfologieën, inhomogeniteiten en blokkades in het weefsel aangegeven worden. We hebben ook een vest ontworpen om tegelijkertijd elektrogrammen en lichaamsoppervlakpotentialen te meten, zodat de (invasieve) analyse van elektrogrammen vertaald kan worden naar niet-invasieve diagnoses. Onze resultaten laten zien dat de genormaliseerde

tweede singuliere waarde een veelbelovende indicator is om AF te detecteren in zowel een multimodale meting als een enkele modaliteitsmeting.

In het laatste deel concentreren we ons op de klinische toepassing van de ontwikkelde methode om de ernst van atriumfibrilleren te detecteren bij patiënten met een voorgeschiedenis van AF tijdens een sinusritme-episode. Onze resultaten tonen aan dat de ruimtelijke variatie van atriale potentiële golfvormen kan worden onthuld door de kenmerken die zijn geëxtraheerd uit de singuliere waarde-ontleding van het absolute frequentiespectrum van de epicardiale metingen. Deze kenmerken laten een duidelijk verschil zien tussen verschillende stadia van AF, wat de spreiding van de actiepotentiaalmorfologie benadrukt.

1

INTRODUCTION

1.1. RESEARCH MOTIVATION

The heart, with its complex electrical and mechanical system, is an essential component of the cardiovascular system, ensuring the proper functioning and circulation of blood throughout the body. Coordinated electrical signals initiate and regulate the heart's contraction and relaxation, allowing it to efficiently pump blood and support essential body activities. However, certain cardiac arrhythmias, like atrial fibrillation (AF), interfere with this harmonious electrical activity, leading to disrupted heart rhythms.

Atrial fibrillation (AF) is the most common and sustained arrhythmia in the heart, affecting 2% of the world's population, increasing the mortality rate and cost of health care [1]. One out of four individuals is expected to experience AF in their lifetime [1]. AF is characterized by the rapid and irregular electrical activity within the heart [2]. This disrupted rhythm creates asynchronous contraction of the atria, leading to impaired blood pumping and raising the risk of serious complications, including stroke, heart failure, and diminished quality of life for those affected.

AF is a progressive disease characterized by an increased risk for recurrent or persistent episodes of irregular heart rhythm. It can deteriorate over time, increasing the frequency, length, and severity of the episodes. AF can be classified into four groups ranging from short-lasting episodes to long-lasting episodes, as paroxysmal, persistent, long-lasting persistent, and permanent AF (shown in Fig. 1.1). Moreover, it is the most frequent complication reported in patients without a pre-existing history of AF following cardiac surgery, referred to as *de novo*. Such cases usually can be considered as paroxysmal AF, although occasionally this turns into persistent AF. Induced AF represents another category of AF that arises due to an external trigger signal. Unlike spontaneous AF, which occurs naturally, induced AF allows for controlled experimental conditions where specific triggers or interventions can be employed to initiate AF. This offers researchers greater flexibility and could be beneficial in demonstrating the characteristics of different types of AF.

The electrical propagation in the heart during normal sinus rhythm (SR) follows a synchronized pattern, beginning with the initiation of an electrical signal by the sinoatrial (SA) node. This signal propagates across the atria, causing them to

1

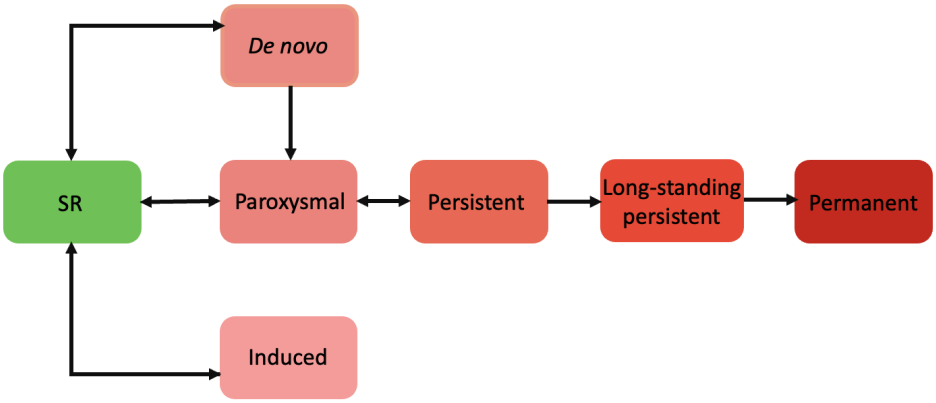

Figure 1.1: The progression of AF severity and its various types. We did not use an extra arrow from *de novo* to persistent AF to avoid complications in this figure. Instead, the path from *de novo* to persistent AF is shown via paroxysmal AF.

contract and pump blood into the ventricles. It then reaches the atrioventricular (AV) node, which allows the signal to pass through to the ventricles [3]. In atrial fibrillation, however, the electrical propagation becomes chaotic and disorganized. Multiple irregular signals fire simultaneously within the atria, leading to ineffective atrial contractions and an irregular heart rate [4].

AF is a progressive complex arrhythmia that involves multiple factors, including electrical, structural, and functional abnormalities in the atrium [5]. The progression of AF involves a transition from a triggered-driven arrhythmia, characterized by AF initiation in response to specific stimuli, to a substrate-mediated arrhythmia with structural or functional changes in the atria [6]. Therefore, the timely detection of AF is crucial for diagnosis and treatment.

According to current cardiology guidelines, the standard method for detecting AF is typically a 12-lead electrocardiogram (ECG) [7]. ECG provides a non-invasive comprehensive evaluation of cardiac electrical activity by capturing the overall electrical signals generated by the heart. The basic level of AF detection is to classify the ECG recordings into two categories: SR and AF. Despite extensive research on this classification, current methods do not provide sufficient information about the severity of AF. Severity detection could be informative and valuable for AF treatment. For example, the success rate of one of AF's common treatments (ablation therapy) for paroxysmal patients is between 70% and 80%, while this rate drops to 45%-60% for persistent patients. This shows the importance of AF severity detection in the treatment process. Some studies compared self-terminating and sustained AF [8, 9], or paroxysmal versus persistent AF [10]. However, the severity detection of AF based on purely AF episodes (i.e., without SR) using comprehensive information on multi-lead ECG is not well-addressed. Therefore, further investigations in this specific case are needed.

Despite all the advantages of using ECG (and multi-lead ECG), ECG has limitations

in demonstrating different stages of AF. Firstly, ECG has limited spatial resolution, which only gives a general overview of the heart's electrical activity without detailed information about specific atrial regions involved in AF initiation and maintenance. Thus, standard ECG recordings may not adequately capture localized electrical abnormalities or focal triggers. In addition to its spatial limitations, ECG also lacks the ability to provide detailed information on the atrial remodeling that occurs in the progression of AF. ECG recordings do not directly detect electrical changes or conduction abnormalities in the atria causing AF progression. These important aspects of atrial remodeling, which play a critical role in the maintenance of AF [11], are not detectable through surface ECG measurements. These limitations highlight the need for complementary techniques, such as intra-operative electrograms (EGM), which can provide detailed information through high spatial-resolution recordings.

Intra-operative electrograms allow for detailed insight into conduction properties, activation patterns, tissue characteristics, abnormal conduction pathways, and localized sources contributing to AF. By recording electrograms from the surface of the heart, it becomes possible to analyze conduction velocities, conduction delays, and activation patterns. These measurements aid in the identification of conduction abnormalities, such as slowed conduction or conduction block, and can provide valuable insights into the mechanisms underlying complex arrhythmias such as AF. There has been extensive research on the EGM analysis regarding conductivity-based parameters leading to AF. However, during an SR episode, conduction parameters do not serve as distinguishable markers for severity detection of AF [12, 13]. To overcome this, some research showed that morphology-based markers could be a promising tool to study condition disorders[14, 15]. We believe that going further in analysing the morphology of the electrograms could be useful in the severity detection of AF and finding electropathological regions.

The primary goal of this thesis is to conduct research aimed at improving the severity detection of atrial fibrillation. To achieve this goal, we have developed a signal processing framework that utilizes ECG and EGM signals to enhance the severity detection of AF. Subsequently, we propose relevant features for AF detection and identification of electropathological regions within the heart. The overall structure of our work adopts careful feature engineering, as the basis of subsequent machine learning-based classification. The block diagram presented in Fig. 1.2 illustrates the process flow.

The input signal represents the trigger signal for the electrical activity in the heart, which propagates through the cardiac tissue and generates epicardial potentials upon reaching the epicardium. Here, we use data recorded from two levels of measurement. Let us consider multi-channel measurements for each of these levels. We assume an LTI (Linear Time Invariant) system, denoted as $h_{EGM}(t)$, which models the spatiotemporal low-pass filter related to the normal propagation of the electrical activity or AF substrate for signal propagation at a given time. At the first level of measurement, high-resolution epicardial electrode arrays record epicardial EGMs, resulting in $y_1(t)$. To demonstrate the propagation of electrical activity from the cells to the epicardial level, we have developed a method that uses the EGMs to identify electropathological regions within the atrium. Subsequently, we proposed

1

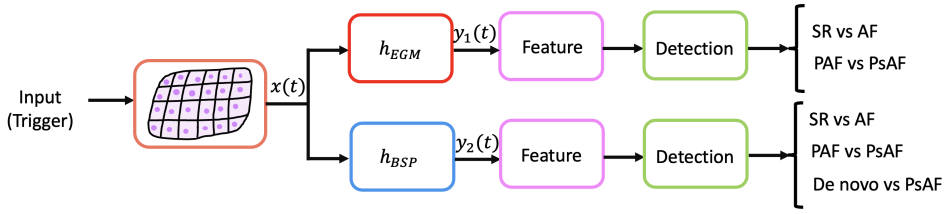

Figure 1.2: The signal processing framework developed in this thesis.
Paroxysmal AF (PAF), persistent AF (PsAF)

features that could help diagnose the progression of AF.

At the second level of measurements, the electrical activity of the heart is recorded through low-resolution ECGs or in general body surface potentials (BSP) on the surface of the body, resulting in $y_2(t)$. The estimation of the h_{BSP} filter involves determining the lead field and electrode model, which require knowledge of the geometric information of the electrodes. However, during open-heart surgery or minimally invasive procedures, this geometric information is not readily available.

As a result, due to the lack of geometrical information, alternative methods are needed to analyze the electrical activity in the heart. These models serve as substitutes to compensate for the lack of complete information regarding the electrode geometry and lead field. As an alternative approach, we propose extracting features from raw ECG data which serve as sufficient statistics [16] derived from the observations, providing comprehensive information on the system, aiming to increase the accuracy of AF severity detection.

Therefore, the primary purpose of this thesis is to improve the severity detection of atrial fibrillation. We believe that severity detection starts from revealing the nature of the data. Using different measurement levels helps us increase our knowledge about the heart's electrical activity, aiming to conduct a comprehensive study that can distinguish the characteristics of different stages of AF.

1.2. RESEARCH OBJECTIVES

This project aims to improve our knowledge of the complex electrical abnormalities that contribute to the initiation and maintenance of AF by utilizing the combined experience of engineers and medical professionals through responding three crucial AF-related research concerns. This is accomplished by a thorough examination of electrophysiological data, computer modelling, and experimental investigations.

Considering different types of AF (Fig. 1.1) and their respective characteristics, it is crucial to emphasize the importance of timely and accurate detection of AF, along with assessing its severity, as these factors play a vital role in effective management and improved outcomes.

In the context of detecting the severity of AF, two specific scenarios pose more

significant challenges. The first challenge is distinguishing the progression of AF when the patient develops AF. However, the visual inspection of the surface ECG is unable to determine the severity of AF. The second challenge is when the patient has a normal sinus rhythm and has experienced an AF episode in the past. In the latter case, electropathological regions could initiate AF, while the recorded surface ECG can not reveal them due to its low spatial resolution. Therefore, considering these challenges, the main research objective of this thesis is to address three key research questions:

Q1. Can we distinguish different stages of AF progression using multi-lead ECG measurements?

The first research question is to quantify the progression of AF. This involves analyzing multi-lead ECG signals to detect the severity of AF and track its evolution from shorter-lasting AF, such as paroxysmal AF, to more prolonged and persistent forms, such as persistent AF. Indeed, in the first research question, we will address the first challenge in the severity detection of atrial fibrillation by finding characteristics of AF within the AF episodes. To this end, we have identified distinctive features that provide insights into the characteristics of atrial fibrillation. However, the limitations of the multi-lead ECG prevent a detailed analysis of regional electropathology. To overcome this limitation, we go deeper into the surface of the heart and use high-resolution EGM signals to detect regions representing variations in atrial potential within the cardiac tissue. This approach allows us to explore the electropathological aspects at a more localized level. Then a follow-up question will be:

Q2. Can we develop a simple and practical tool to effectively capture the differences in atrial potential morphology or abnormal wavefront propagation, thereby enabling the identification of electropathological areas specific to AF?

In this context, our initial focus is on developing a tool to identify the electropathological regions within the heart. Then subsequent questions would be:

Q2.1. Can we propose discriminative features to effectively detect electropathological regions on the epicardial measurements?

Q2.2. Can we use the same features to distinguish between SR and AF using body surface potentials?

As the next step, we are interested in the clinical application of the proposed method. Therefore, we address one of the most challenging clinical questions as:

Q3. Can we derive relevant features based on the EGM analysis to accurately assess the severity of AF in patients with a history of AF, during SR?

Different characteristics of AF would be better revealed if these research questions could be successfully addressed. Eventually, these characteristics could help develop better diagnostic techniques and treatment plans.

1.3. OUTLINE OF THE THESIS

This section presents an overview of the dissertation's structure and highlights the contributions made in each chapter. Fig. 1.3 illustrates the problem formulation into different chapters. To address the research questions listed in Section 1.2, the

1

investigation begins with the utilization of multi-lead ECGs. As the study progresses, it goes deeper into the analysis of multi-lead EGMs to detect AF and gain insights into its underlying electropathology. By employing a comprehensive approach that incorporates both ECG and EGM data, this research aims to unveil valuable information about the characteristics of AF.

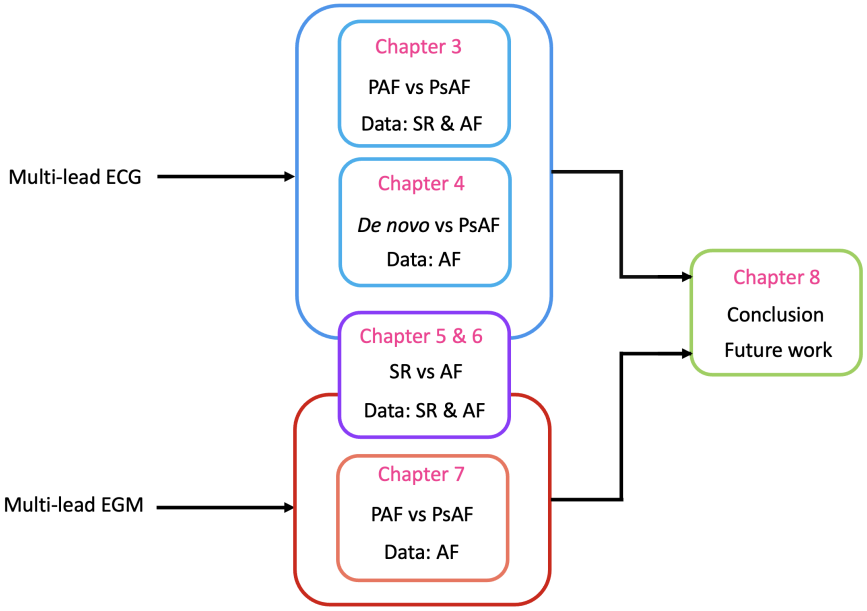

Figure 1.3: The topic of different chapters in the severity detection of atrial fibrillation. Here, blue denotes multi-lead ECGs have been used, red denotes EGMs have been used, and purple color (blue+red) denotes both ECGs and EGMs have been used for the analysis.

1.3.1. CHAPTER 2: RESEARCH BACKGROUND

This chapter serves as a comprehensive introduction to the essential background knowledge required for understanding this dissertation. We first explain the heart's physiology and anatomy, focusing on its electrical conduction system. Additionally, we explore monitoring systems used to evaluate heart conditions and focus on two types of signals: ECG and intra-operative EGM.

Moving forward, we present an in-depth examination of atrial fibrillation, including its different types, underlying mechanisms, and characteristic manifestations on ECG and EGM. We then explore various methods employed for detecting and classifying AF, primarily focusing on using ECG signals.

Furthermore, we provide an overview of action potential and atrial potential modeling, shedding light on the principles and approaches involved in representing the electrical activity of the heart. We also explore the concept of cardiac

mapping and discuss the diverse measures derived from this technique that aid in understanding and analyzing cardiac electrical patterns.

1.3.2. CHAPTER 3: SEVERITY DETECTION OF ATRIAL FIBRILLATION: PAROXYSMAL VS PERSISTENT

In this chapter, a framework is developed to differentiate between two types of atrial fibrillation, namely paroxysmal and persistent AF. This step is important because ECG recordings usually contain both SR and AF episodes, and distinguishing between different stages of AF could be beneficial for early diagnosis. The framework utilizes multi-lead ECGs obtained from both SR and AF episodes. The multi-lead ECG is segmented to focus on the atrial activity. Then, in order to extract the morphological characteristics of each type of AF (i.e., paroxysmal and persistent AF), we use a canonical polyadic decomposition (CPD), which extracts unique characteristics of paroxysmal and persistent AF. This framework serves as the initial step in AF detection and partially answers research question Q1 when the ECG contains both SR and AF episodes. Using CPD, we decomposed the original tensor into three loading vectors: time, heartbeat, and channel, which provide insight into the variability of the multi-lead ECG in the temporal morphologies, heartbeats, and channels. The time loading vector can be employed to determine the severity of AF by providing the time series pattern of either an arrhythmia or a normal P wave.

1.3.3. CHAPTER 4: SEVERITY DETECTION OF ATRIAL FIBRILLATION: *de novo* VS PERSISTENT

In this chapter, we continue on research question Q1 by focusing on the severity detection of atrial fibrillation and specifically differentiating between *de novo* post-operative AF (as an example of short-lasting AF) and persistent AF (as an example of long-lasting AF). Our analysis is conducted solely on AF episodes to gain insights into the severity differences between these two types. The focus of this chapter is to find specific characteristics of AF for different degrees of AF, within an AF episode. This classification is important since the severity of AF is not detectable by the visual inspection of the surface ECG during an AF episode. Given the nature of this arrhythmia, we propose a method that utilizes discriminative features derived from multi-lead ECG data, including rhythmic and morphological changes from the multi-lead ECG. The results demonstrate the effectiveness of the proposed features in revealing the severity of AF.

1.3.4. CHAPTER 5: A SINGULAR-VALUE-BASED MARKER FOR THE DETECTION OF ATRIAL FIBRILLATION

In the previous chapter, we extracted the chaotic nature of AF by groups of features, including the morphological and rhythmic changes. In this chapter, we go deeper to the surface of the heart to explore the underlying factors responsible for this chaotic nature. Here, we focus on answering the second research question (Q2) by developing a method that quantifies and detects the extent of atrial potential

variation. This method serves as a marker to differentiate between SR and AF. Ultimately, this marker holds the potential for identifying electropathological regions within the atrium.

Our research reveals that changes in the singular values of the epicardial measurement matrix provide an effective description of the diversity in the morphology of atrial potential across a single heartbeat. This method provides insights into areas of potential fractionation and block. In Chapter 5, we evaluate the proposed method on simulated tissues in different scenarios.

1.3.5. CHAPTER 6: EVALUATION OF THE SINGULAR-VALUE-BASED MARKER ON CLINICAL DATA

In this chapter, we evaluate the proposed method in Chapter 5 on clinical data. We provide the assessment from two types of clinical data. Additionally, to extend our proposed method on the non-invasive measurements, we conducted an experiment simultaneously measuring EGMs and a multi-lead electrocardiogram ECG, comparing the severity analysis at the surface of the heart with the surface of the body. Overall, the singular value-based features proved to be valuable indicators for detecting and evaluating AF. More importantly, the proposed method has the potential to identify electropathological regions within the tissue.

1.3.6. CHAPTER 7: SEVERITY DETECTION OF ATRIAL FIBRILLATION: DURING SINUS RHYTHM

This chapter focuses on answering Q3 with one specific practical application of the singular-value-based marker for the detection of AF severity. Although electropathological features obtained from intra-operative epicardial measurements, like conduction block (CB), is frequently used to evaluate the severity of AF, they do not reveal significant distinctions between various stages of AF development during sinus rhythm. To address this limitation, we use the method developed in Chapter 5 and propose rank-related features to enhance AF severity detection. Based on the method developed in the previous chapter, we derive two novel features that improve the AF severity detection.

1.3.7. CHAPTER 8: CONCLUSIONS AND FUTURE WORK

The contributions made in this dissertation are summarised in this chapter, together with the accompanying conclusions. It also includes any unanswered questions that remain after conducting this research and offers suggestions for possible future courses that could be taken to address these issues.

1.4. RESEARCH CONTEXT: MEDICAL DELTA CARDIAC ARRHYTHMIA LAB

This project is funded in part by the Medical Delta Cardiac Arrhythmia Lab (CAL). Medical Delta is an organization that fosters collaboration between Leiden

University Medical Center, TU Delft, and Erasmus Medical Center. The CAL's primary purpose is to develop methods to reduce cardiac arrhythmias by understanding the electropathology of the disease. Knowledge of the location of electropathological regions can then be used to improve cardiac diagnosis and treatment. This project is one of the projects in this scope as a collaboration between the TU Delft and the Erasmus Medical Center, aiming to improve the severity detection of atrial fibrillation.

1.5. LIST OF PUBLICATIONS

This section provides a comprehensive listing of all the papers that have been submitted and published throughout the duration of the Ph.D. program.

JOURNAL

1. **H. Moghaddasi**, R. C. Hendriks, A. J. van der Veen, N. M. S. de Groot, and B. Hunyadi, *Classification of De novo post-operative and persistent atrial fibrillation using multi-channel ECG recordings*, Computers in Biology and Medicine, 143, 105270, 2022.

2. **H. Moghaddasi**, R. C. Hendriks, B. Hunyadi, M. Schie, P. Knop, N. M. S. de Groot, and A. J. van der Veen, *A Singular-value-based Marker for the Detection of Atrial Fibrillation Using High-resolution Electrograms and Multi-lead ECG*, (Submitted).

CONFERENCE

1. **H. Moghaddasi**, A. J. van der Veen, N. M. S. de Groot, and B. Hunyadi, *Tensor-based Detection of Paroxysmal and Persistent Atrial Fibrillation from Multi-channel ECG*, 28th European Signal Processing Conference (EUSIPCO), pp. 1155-1159, 2020, IEEE.

2. B. Abdikivanani, **H. Moghaddasi**, R. C. Hendriks, B. Hunyadi, and C. Varon, *Spatio-Temporal Feature Engineering for the Classifi-cation of 12-lead ECG Recordings*, Computing in Cardiology, 2020, Abstract.

3. **H. Moghaddasi**, R. C. Hendriks, A. J. van der Veen, N. M. S. de Groot, and B. Hunyadi, *Novel Rank-based Features of Atrial Potentials for the Classification Between Paroxysmal and Persistent Atrial Fibrillation*, Computing in Cardiology (CinC) conference, 2022, IEEE.

SYMPOSIUM

1. **H. Moghaddasi**, B. Hunyadi, A. J. van der Veen, N. M. S. de Groot, and R. C. Hendriks, *Model-based characterization of de novo POAF and persistent AF using 12-lead ECG signals*, 8th Dutch Bio-Medical Engineering Conference, 2021

2. **H. Moghaddasi**, B. Hunyadi, A. J. van der Veen, N. M. S. de Groot, and R. C. Hendriks, *Surface Electrocardiogram Reconstruction Using Intra-operative Electrograms*, 42nd WIC Symposium on Information Theory and Signal Processing in the Benelux (SITB 2022), 2022.

3. **H. Moghaddasi**, R. C. Hendriks, A. J. van der Veen, N. M. S. de Groot, and B. Hunyadi, Novel Rank-based Features OF Atrial Potentials for the Classification Between Paroxysmal and Persistent Atrial Fibrillation, 9th Dutch Bio-Medical Engineering Conference, 2023

INTERNAL TECHNICAL REPORTS

1. **H. Moghaddasi**, B. Hunyadi, A. J. van der Veen, N. M. S. de Groot, and R. C. Hendriks, *Surface ECG Reconstruction Using Intra-operative Electrograms-Conditions and Limitations*, 2022.

2

BACKGROUND AND FUNDAMENTALS

In Chapter 1, we provided an overview of the main objectives and the research questions we aim to address in this thesis. Chapter 2 offers essential background information to provide greater detail to the research questions. We start with clarifying the medical definitions which are employed in the thesis. Here, we mainly focus on the heart's electrical conduction system and monitoring modalities. Then, we explain the characteristics of atrial fibrillation and its diagnostic methods. Finally, we examine the action potential propagation and electrical activity modeling in the heart to improve the diagnostic performance of AF. The general sources for the medical terms explained in this chapter are derived from references [17, 18].

2.1. ANATOMY AND PHYSIOLOGY OF THE HEART

2.1.1. HEART'S ANATOMY AND ITS FUNCTION

The heart is a muscular organ in the chest cavity with four chambers, namely two atria (upper chambers) and two ventricles (lower chambers). From the functional point of view, we can divide the heart into two sides: right and left. Deoxygenated blood is directed into the right side of the heart, from where it is subsequently pumped to the lungs for oxygenation. On the other hand, the left side of the heart is responsible for pumping oxygenated blood to supply the organs with oxygen and nutrients.

The heart's function is to pump blood throughout the body, ensuring the oxygen and nutrients are transported to all organs while the waste products are removed from them. This is achieved by the cardiac cycle, a series of synchronized contractions. During the cardiac cycle, the heart goes through two separate stages: diastole and systole. The heart relaxes during diastole, allowing blood from the veins to flow into the atria. This blood is then sent to the ventricles. Subsequently, during the systole, the ventricles contract and send blood into the arteries [19].

2.1.2. CONDUCTION SYSTEM IN THE HEART

The heart's conduction system starts from the sinoatrial (SA) node, where action potentials (AP) are generated as electrical impulses that initiate each heartbeat. These action potentials propagate through the atria, causing atrial contraction and facilitating blood flow into the ventricles. Moving through specialized pathways, such as the Bundle of His and Purkinje fibers, the action potentials activate different regions of the ventricles. This coordinated activation leads to synchronized ventricular contraction, enabling effective ejection of blood into the pulmonary artery and aorta, thus supporting proper circulation throughout the body.

It is important to note that action potentials show distinct characteristics at various locations within the heart (compare the APs at the SA node and contractile myocardium in Fig. 2.1). The action potentials in the SA node are relatively short without a plateau phase. In contrast, the action potentials in contractile myocardium are stimulus-dependent with a longer duration. During the action potential, there is a refractory period, which is divided into phases: absolute and relative refractory. During the absolute refractory period, no stimulus can trigger an action potential, while during the relative refractory period, the generation of a new action potential depends on the strength of the stimulus. [17].

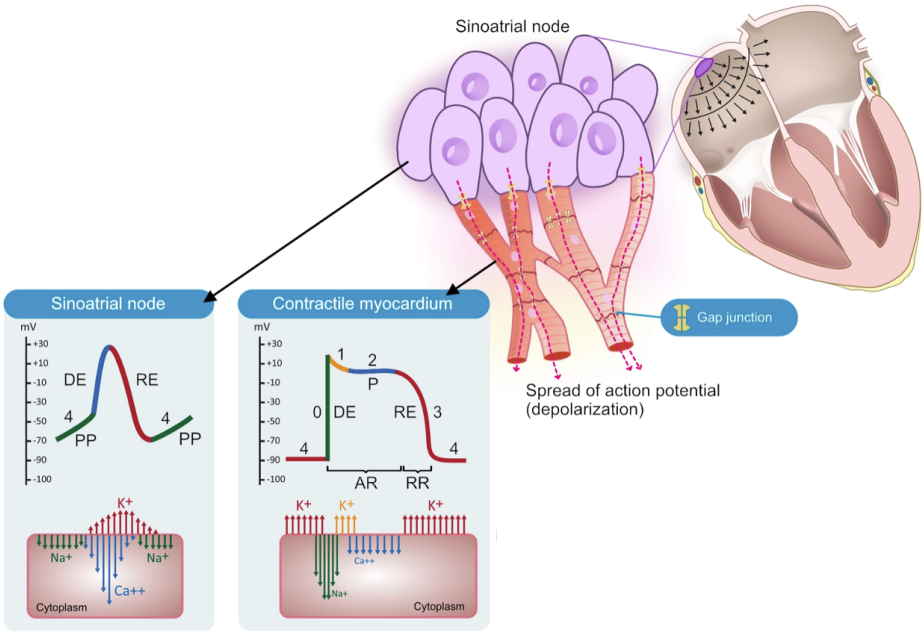

Figure 2.1: Action potential propagation in the heart
P = Plateau phase, RE = Repolarization, DE = Depolarization, PP = Pacemaker Potential, RR = Relative refractory period, AR = Absolute refractory period (adapted from [20])

2.1.3. ELECTRICAL ACTIVITY MEASUREMENT OF THE HEART

The electrical activity of the heart can be measured by different techniques that provide insights at different levels of measurement. An ECG is a non-invasive measurement technique that assesses the electrical activity generated by the heart from the surface of the body. The ECG provides a general overview of the heart at a few spots on the surface of the body. To study the electrical activity in the heart in more spatial detail, a more invasive measurement method called an electrogram is used. Unlike ECG, electrograms are recorded from the surface of the heart and provide a more localized view of the electrical activity at the surface of the heart. At an even more granular level, measurement systems are used to evaluate the electrical activity of the heart at the cellular level. These systems commonly use patch clamp techniques, which involve sealing off individual heart cells with tiny glass micropipettes. However, this thesis only concentrates on the measurements obtained from the surface of the body and the surface of the heart. Fig. 2.2 summarises our approach throughout the thesis. We embark on a comprehensive exploration, beginning from the surface of the heart[1] and delving deeper into both the heart tissue and cellular level[2].

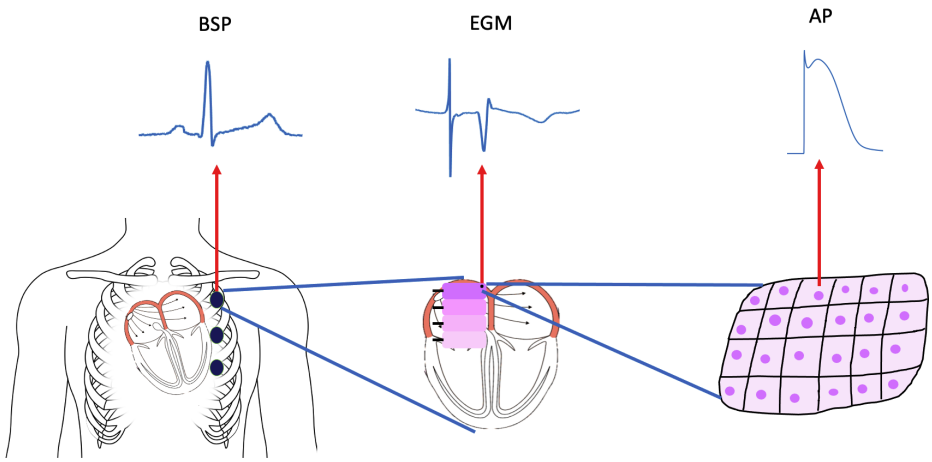

Figure 2.2: Different levels of observation

2.1.4. ELECTROCARDIOGRAM

The electrocardiogram (ECG) shows a general overview of the electrical activity of the heart, and consists of 3 main phases, namely, P wave, QRS complex, and T wave (Fig. 2.3 A). The P wave is generated by the atrial depolarization,

[1] Electrical signal measurements from the surface of the heart are generally called body surface potentials (BSP).

[2] Note that our analysis at the cellular level is based on simulations.

which initiates the atrial contraction. The beginning of ventricular contraction is represented by the QRS complex corresponding to ventricular depolarization. The T wave denotes ventricular repolarization, which denotes the ventricles' recovery phase. When taken as a whole, these elements provide details regarding the timing, progression, and duration of cardiac electrical events. A multi-lead ECG enhances the diagnostic capability by employing multiple electrode placements, allowing for a more comprehensive assessment of the heart's electrical activity from different angles and perspectives. The 12-lead ECG configuration is the most often used technique for multi-lead ECG. This method involves positioning ten electrodes on

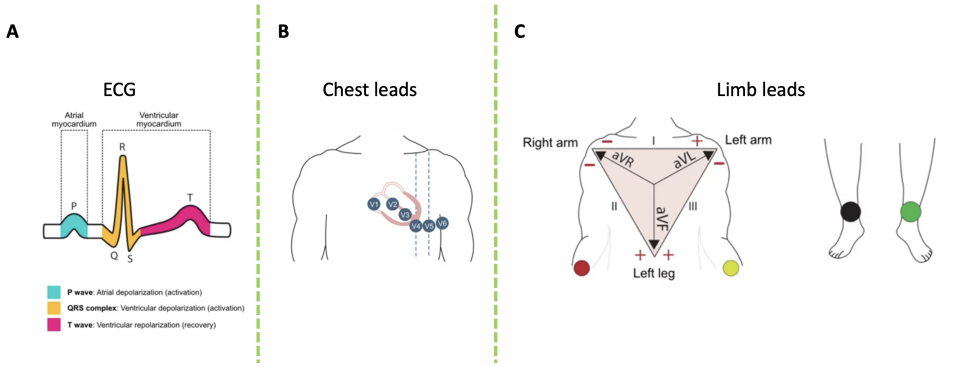

Figure 2.3: ECG and 12-lead electrode placement, A) Different phases of the ECG, B) Chest leads, C) Limb leads (adapted from [21])

the chest and limbs to record electrical activity from various angles. The chest leads are shown in Fig. 2.3.B, resulting in $V1-V6$, and the limb leads are shown in Fig. 2.3.C, resulting in I, II, III, aVR, aVL, and aVF. The positioning of the electrodes plays a crucial role in multi-lead ECG analysis. Fig. 2.4 illustrates two out of the twelve ECG signals, demonstrating distinct signal morphologies on each lead. These variations in morphology provide valuable information about the cardiac condition and aid in diagnostic interpretation. For example, the enlarged or absence of a P wave, widened or irregular QRS complex, inverted or flattened T wave, the elevation of the ST segment, and prolongation of the QT intervals are instances of variations in the ECG morphology which each is related to a specific cardiac disease.

2.1.5. ELECTROGRAM

Electrograms (EGM) obtained from the epicardium provide a direct measurement of the electrical activity from the surface of the heart. These measurements can be taken during open-heart surgery, minimally invasive procedures, through catheters or by the use of cardiac implanted devices. EGM traces can be separated into two distinct phases: atrial activity and ventricular activity.

The analysis of EGMs involves examining both the morphology and time characteristics. Time analysis focuses on a critical parameter known as the local activation time (LAT), which indicates the moment when the cell beneath the

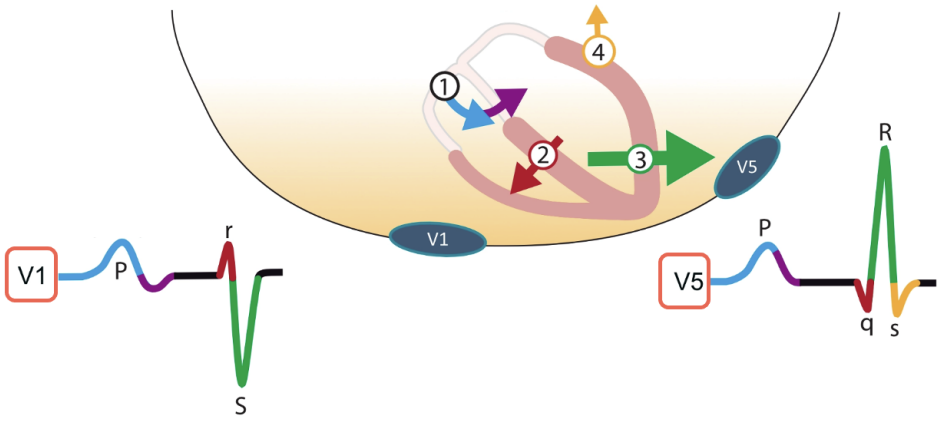

Figure 2.4: The effect of the electrode placement on the multi-lead ECG (adapted from [21])

electrode becomes activated. Specifically, the LAT is defined as the time when the cell's depolarization phase reaches a membrane potential of -40mV (shown in Fig. 2.5).

From a morphological perspective, it is essential to evaluate various features of the atrial activity duration. This includes analyzing single potentials (SP), double potentials (DP), and fractionated potentials (FP). These characteristics provide valuable information about the electrical behavior and abnormalities within the atrial region of the heart.

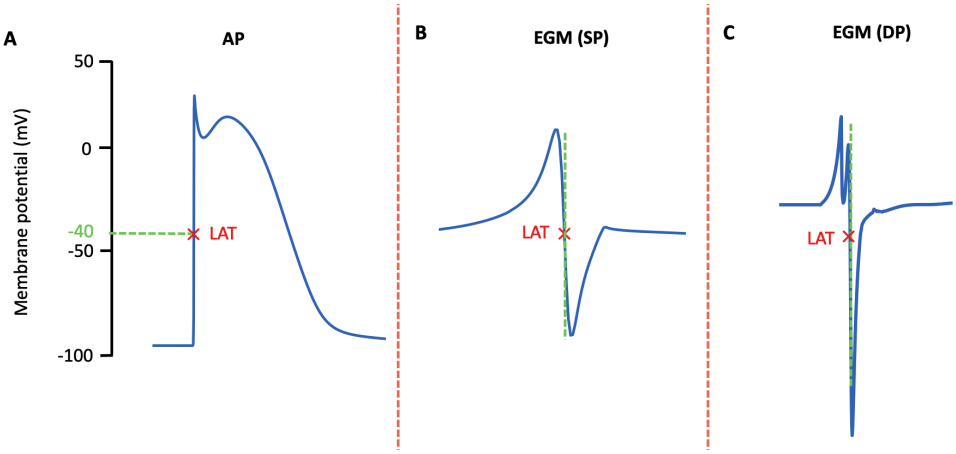

Figure 2.5: Action potential and electrograms, A) AP B) EGM with single potential, and C) EGM with double potential. (The AP and EGMs are generated from the simulation described in Section 5.2.6)

2.1.6. SINUS RHYTHM

Sinus rhythm (SR) is the normal and regular rhythm in the heart where the electrical activity starts from the SA node and propagates through the tissue. During an SR episode, the ECG shows three main phases: P wave, QRS complex, and T wave. The typical values for resting heart rate (HR) vary by age group. Newborns often have a resting HR of 120 to 160 beats per minute, while adults typically have a resting HR between 60 and 100 beats per minute. Besides, in a resting state, the RR interval (the time between two consecutive R peaks) is relatively constant, creating a regular heart rhythm. Note that there are a few metrics to quantify the heart rate variability (HRV), such as the standard deviation of normal-to-normal intervals (SDNN). The variation of SDNN between 50 ms and 100 ms is considered a normal range of HRV in healthy people [22].

2.1.7. CARDIAC ARRHYTHMIA

An irregularity in the heart's electrical activity that disrupts the usual rhythm is referred to as cardiac arrhythmia. Arrhythmias can be systematically classified by considering their origin, mechanism, and specific characteristics. A fundamental categorization involves distinguishing between atrial arrhythmias and ventricular arrhythmias. Atrial arrhythmias originate in the atria, whereas ventricular arrhythmias arise in the ventricles. This categorization enables a clear distinction between irregular heart rhythms originating from the upper chambers (atria) and the lower chambers (ventricles) of the heart.

2.2. ATRIAL FIBRILLATION

2.2.1. DEFINITION OF ATRIAL FIBRILLATION

Atrial fibrillation (AF) is a cardiac arrhythmia that can be defined by rapid, chaotic electrical activity in the atria, causing irregular and accelerated contractions of the ventricles. The significant symptoms of AF are chest pain, fatigue, palpitations (fast heartbeats), shortness of breath, and syncope (fainting) [23, 24]. AF increases the chances of heart-related complications, such as stroke. It also increases the mortality rate by two times in comparison to people without AF (according to a study on patients between the years 1980 and 2000 reported in [25]).

VISUALIZING ATRIAL FIBRILLATION

On an ECG, AF is characterized by the absence of specific P waves and the presence of irregularly between the RR intervals [2, 26]. An ECG and an EGM signal of one patient during AF and SR episodes are shown in Fig. 2.6. In the SR episode, the P waves preceding the QRS complex, alongside constant RR intervals can be seen on the ECG. On the EGM, one can observe single atrial potentials occurring prior to ventricular activity. Conversely, in the AF episode, fibrillatory waves or the absence of a P wave and irregular RR intervals, can be seen on the ECG. The EGM recording during AF reveals double potentials or fractionated potentials, sometimes coinciding

with ventricular potentials within each cardiac cycle, leading to a chaotic pattern (i.e., irregular variation in the morphology and rhythm) in the ECG.

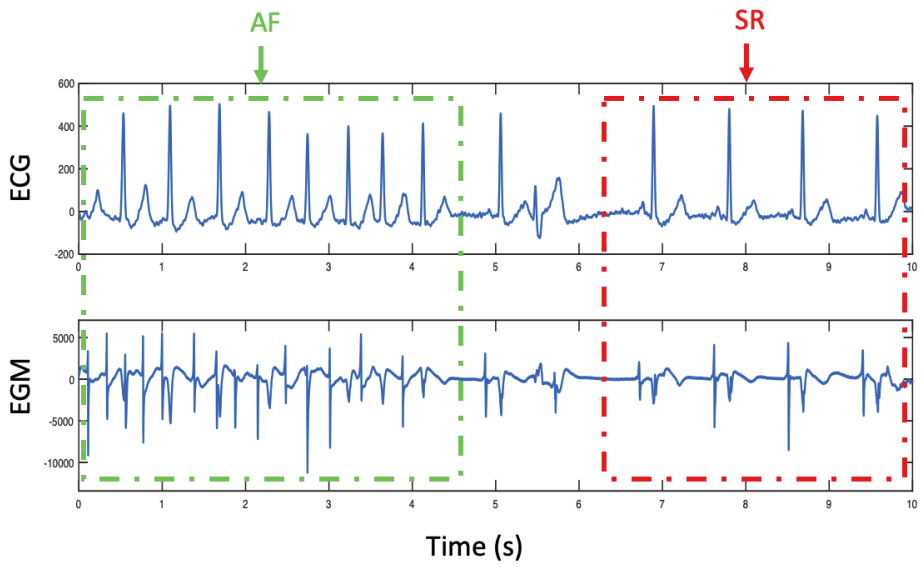

Figure 2.6: AF and SR episodes are shown on ECG and EGM recordings. The green color denotes the AF episode, and the red denotes the SR episode.

2.2.2. TYPES OF ATRIAL FIBRILLATION

An AF episode is a period during which the AF characteristics are present for longer than 30 seconds [27]. According to cardiology guidelines, atrial fibrillation can be classified into four distinct categories based on the duration of the AF episode: paroxysmal, persistent, long-lasting persistent, and permanent AF which are shown in Fig. 1.1. Paroxysmal AF refers to episodes that spontaneously resolve within 7 days, while persistent AF extends beyond 7 days or necessitates intervention to restore the heart's normal sinus rhythm. A sub-category within the paroxysmal AF group called post-operative *de novo* AF happens in patients who have not previously experienced atrial fibrillation and develop AF following cardiac surgery. Long-standing persistent AF describes a continuous state of AF lasting for over 12 months. Finally, permanent AF characterizes a condition where attempts to restore sinus rhythm have failed, leading to persistent AF that is ongoing indefinitely [27, 28].

For research purposes, AF can be induced through a controlled pacing procedure. In this case, AF is triggered during the experiment, allowing researchers to set the trigger points and analyze the response obtained from this procedure. The heart rhythm restores to normal sinus rhythm after a few seconds.

2.2.3. UNDERLYING MECHANISMS OF AF

The mechanism of AF has been the subject of extensive investigation in numerous studies. These studies have identified several key mechanisms that play a role in both the initiation and perpetuation of AF [29–32]. One such mechanism involves the presence of ectopic foci (or local ectopic firing [29]), which are abnormal sites within the atrial tissue that generate spontaneous electrical activity, disrupting the normal heart rhythm. Additionally, the formation of rotors has been implicated in AF, where electrical waves circulate in a self-sustaining loop, leading to the irregular and rapid electrical impulses characteristic of AF [30]. Furthermore, multiple wavelets are another mechanism for AF proposed by Moe et al. [31]. This mechanism suggests that multiple wavelets, either through collision or generation of new wavelets, contribute to the development of AF [31, 33, 34]. Another contributing mechanism in AF is breakthrough which happens due to the asynchrony between the endocardium and epicardium (the inner and outer layers of the heart)[35]. More than one mechanism could be involved in AF initiation and maintenance, making these mechanisms not necessarily contradictory.

2.2.4. ATRIAL FIBRILLATION TREATMENT

Treatment of AF varies according to age, overall health, severity of AF, and symptoms. One of the most important treatments of AF is ablation therapy. Ablation therapy uses catheters to identify and destroy the abnormal electrical regions that are the cause of the arrhythmia. In this method, catheters are inserted into the blood vessels reaching the heart. Radio frequency energy or cryo-energy is then used to destroy the targeted area which makes small scars. The abnormal electrical pathways are blocked by these scars, resulting in restoring the normal sinus rhythm. Ablation therapy for atrial fibrillation employs various techniques, including pulmonary vein isolation (PVI), which aims to isolate and ablate the pulmonary veins, and more extensive ablation approaches that target additional areas of the atria. The efficacy of ablation therapy in managing AF is influenced by factors such as the specific type and duration of AF. For example, for individuals diagnosed with paroxysmal AF, the success rate of ablation therapy ranges from 70% to 80%. However, for patients experiencing persistent AF, the success rate diminishes to approximately 45% to 60% [36]. Therefore, timely detection is crucial.

2.3. ATRIAL FIBRILLATION CLASSIFICATION BASED ON ELECTROCARDIOGRAM

As mentioned in Chapter 1, in this thesis, we start from the body's surface by analyzing multi-lead ECGs. To do so, we explain in this section the state-of-the-art classification methods for AF detection using ECG signals. This will facilitate the understanding of our approach for severity detection of AF in Chapter 4. Then, we go deeper from low-resolution analysis (i.e., multi-lead ECGs) to high-resolution analysis (i.e., electrograms) to improve severity detection of AF. Therefore, in Section 2.4, we explain the propagation of the atrial activity on the heart tissue by delving

into the signal model at the electrogram level. We will use this information to develop our method in Chapter 5 and Chapter 7.

In the context of assessing the severity of atrial fibrillation (AF), a fundamental approach involves distinguishing ECGs into two categories: SR episodes and AF episodes. However, this classification can be challenging due to several reasons. First, the ECG recording is affected by different kinds of noises. These noises and artifacts can affect the signal quality, leading to misinterpretation of the recorded signals. For example, a P wave is a low-amplitude signal prone to be disturbed by the artifacts, resulting in a misdetection of the P wave. Since the absence of a P wave or the presence of the fibrillatory wave is one of the AF characteristics, the artifacts pose more challenges in AF detection. Second, AF is intermittent, meaning the patient can be transient between SR and AF episodes. This poses complexity to the analysis. In addition, short data length, patient-specific factors, overlap with other arrhythmias, and overlap with normal heart rate variability are other reasons that make the classification between SR and AF more challenging.

To tackle this challenge, researchers have developed computer-aided diagnosis (CAD) systems. As shown in Fig. 2.7, these systems can be broadly classified into two main categories: handcrafted feature-based methods and deep learning-based methods.

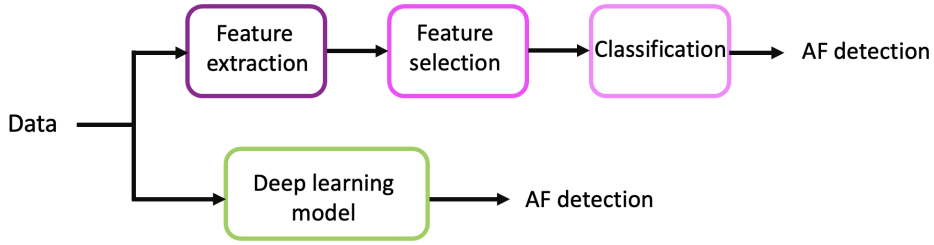

Figure 2.7: The general framework for the AF classification including handcrafted feature-based methods and deep learning-based methods

2.3.1. HANDCRAFTED FEATURE-BASED CLASSIFICATION

Handcrafted feature-based methods use prior knowledge (not necessarily models) about the arrhythmia to extract specific features, which are then inputted into classifiers. Given the nature of AF, handcrafted features can be categorized into four groups: time-based, frequency-based, time-frequency-based, and nonlinear methods.

Time-based features primarily concentrate on capturing irregularities in the RR intervals [37] or variations in atrial activity [38], aiming to detect temporal abnormalities associated with AF. Furthermore, an additional valuable approach is the frequency analysis of fibrillatory waves. One commonly used method within

this category is the computation of the fibrillatory wave ratio using power spectral density analysis [39].

In order to address the limitation of low frequency/time resolution in previous methods, time-frequency techniques are employed, which allow for simultaneous localization in both time and frequency domains. One well-known approach in this domain is the utilization of the wavelet transform to detect atrial activity. This technique enables a more comprehensive analysis by capturing both temporal and spectral information of the signals [40, 41]. Additionally, non-linear methods are used to extract the dynamic characteristics of AF. These approaches capture complex patterns within the AF signals, enabling a more comprehensive understanding of the dynamic behavior represented by the arrhythmia [42].

In many cases, there is a feature selection step following the feature extraction step. Feature selection aims to choose a subset of the extracted features that are more relevant and could improve the performance of the classification task. These methods can be categorized into three major groups: filter, wrapper, and embedded methods. The filter methods, such as ReliefF, primarily filter out features without considering the classification accuracy, only focusing on the characteristics of the features [43]. In contrast, wrapper methods, such as forward selection, choose the features based on their effects on the classification performance [44]. However, since wrapper methods select the subset of features via a repeated algorithm, these methods are not efficient computationally. Instead, embedded methods have advantages of both filter and wrapper methods, where they use learning algorithms with constraints to select the most relevant features [44, 45].

In AF classification, the last phase is a classification step based on the selected features. These methods can be generally categorized into three groups: supervised learning, unsupervised learning, and reinforcement learning. In supervised learning, such as support vector machine (SVM) [46] and random forest (RF) [47], the patients are classified based on the labeled data. Unsupervised learning, such as k-means clustering [48], denotes categorizing the data points without available labels. Finally, reinforcement learning, such as Q-learning [49], classifies the data points based on a trial-and-error approach and rewards. In the context of the handcrafted feature-based classification of AF, the majority of methods are based on the supervised approach, which can provide more interpretable results.

2.3.2. DEEP LEARNING-BASED CLASSIFICATION

The second category for AF classification is deep learning-based methods. They consist of deep neural networks to extract the hidden patterns from the data. Generally, these methods use a large number of annotated data fed to the deep neural networks to unravel the structure of the data. In contrast to the handcrafted features, the majority of deep learning-based methods are designed to be independent [50] of or less reliant [51] on pre-defined discriminative features. However, while these methods offer enhanced performance and flexibility, they may provide less interpretability and insight into the underlying electropathology of AF.

2.4. ACTION POTENTIAL AND ELECTROGRAM MODELS

In the previous section, we have seen the common methods for AF classification using ECGs. In this section, we explore action potential and electrogram signal models. Such computational models are used in Chapter 5 and Chapter 7.

2.4.1. CELL MODEL

The complexity of human atrial action potential properties arises from the intricate interplay of various ion channels, which govern the depolarization and repolarization of the atrial cell membrane, essential for generating the electrical activity responsible for atrial contraction and relaxation. The action potentials are generated by the coordinated influx and outflux of ions, e.g., sodium, potassium, and calcium, resulting in the depolarization and repolarization of the cell membrane.

Different complex computational models have been presented to explore the effects of membrane ionic channels in the sinoatrial node [52], atria [53], and ventricles [54]. These models are computationally intensive, providing detailed insights into the dynamics of ion channel activity and their impact on the electrical properties of different cardiac cell types. One of the fundamental and well-known computational models for human atrial action potential was proposed by Courtemanche et al. [53]. The Courtemanche model characterizes the human atrial action potentials through a series of differential equations that show the behavior of different ion channels, including fast sodium channels, transient outward potassium channels, delayed rectifier potassium channels, and calcium channels. The model has been widely used to investigate the effects of various drugs and conditions on atrial electrophysiology.

2.4.2. ACTION POTENTIAL PROPAGATION MODEL

Using a partial differential equation, the dynamics of the action potential propagation in a mono domain tissue can be modeled by [55]

$$C\frac{\partial V(\boldsymbol{y},t)}{\partial t} = S_v^{-1}\nabla\cdot\boldsymbol{\sigma}\nabla V(\boldsymbol{y},t) + I_{stim}(\boldsymbol{y},t) - I_{ion}(\boldsymbol{y},t) \tag{2.1}$$

In the given equation, the transmembrane potential $V(\boldsymbol{y},t)$ at location $\boldsymbol{y}$ and time t is influenced by several factors, including the membrane capacitance constant (C), cellular surface-to-volume ratio (S_v), and the conductivity tensor ($\boldsymbol{\sigma}$). The stimulation current (I_{stim}) is an external input, and the ionic current (I_{ion}) is derived from the cell model, and depends on V in a complicated way.

2.4.3. ELECTROGRAM MODEL

By elevating our analysis to the epicardial surface of the heart, we can mathematically represent the electrogram measurement through a weighted summation (or continuous integral) of the transmembrane currents as [55]

$$\phi(\boldsymbol{x},t) = \frac{1}{4\pi\sigma_e}\int\frac{I_m(\boldsymbol{y})}{|\boldsymbol{x}-\boldsymbol{y}|}d\boldsymbol{y} \tag{2.2}$$

In the given equation, we assume a uniform extracellular conductivity denoted by σ_e. The vector $\boldsymbol{y}$ represents the cell locations, while $\boldsymbol{x}$ represents the electrode location. Actually, $\phi(\boldsymbol{x}, t)$ is the recorded potential at the epicardial level known as electrogram. In Eq. (2.2), I_m is the transmembrane current defined as

$$I_m = I_{ion} - I_{stim} + C\frac{\partial V}{\partial t} = S_v^{-1}\nabla.\boldsymbol{\sigma}\nabla V \tag{2.3}$$

Using these action potential propagation and electrogram measurement models, we designed a simulator for the heart tissue, which has been used in Chapter 5.

2.5. MEASUREMENT DATA

In this section, we mention two data acquisition schemes. In Section 2.5.1, we explain the telemetry data, which is recorded from the body's surface. In Section 2.5.2, we delve into the cardiac mapping approach for electrogram measurement.

2.5.1. TELEMETRY DATA

Telemetry data refers to monitoring the health condition of the patient in real-time. In this project, we use telemetry multi-lead ECG data, which are recorded at the Erasmus Medical Center (EMC). This data is measured from patients who underwent cardiac surgery, aiming to monitor post-surgical health conditions and patient recovery. The recording duration depends on the monitoring tasks, which varies between 72h and 120h after the surgery. The telemetry data is used in Chapter 3 and Chapter 4.

2.5.2. CARDIAC MAPPING

Cardiac mapping, or more specifically high-resolution epicardial mapping, is a procedure to record the epicardial potentials directly from the surface of the heart through an open heart or minimally invasive surgery. At the Erasmus Medical Center, epicardial measurements have been recorded using an electrode array consisting of 192 unipolar electrodes arranged in a 8×24 rectangular array. The high-resolution electrode, shown in Fig. 2.8 A) with the inter-electrode distance of 2 mm, is placed directly on the surface of the heart (Fig. 2.8 B)). There are 9 common locations for the atrial mapping, which are shown in Fig. 2.8 C) and Fig. 2.9, and the mapping procedure is conducted consecutively at these mapping sites [56]. The signal is recorded in two episodes: SR and AF episodes. The SR recording time varies between 5s and 30s, while the AF recording time varies between 10s and 30s. The AF episode stands for actual and induced atrial fibrillation. In the actual AF recording, the patient had already developed AF, while in the induced AF, the arrhythmia is developed through pacing.

VARIOUS ESTIMATES BASED ON CARDIAC MAPPING

Epicardial mapping is informative about propagation of the electrical activity and conduction disorders. There are some characteristics and maps extracted from the epicardial measurements, some of them are introduced in this section.

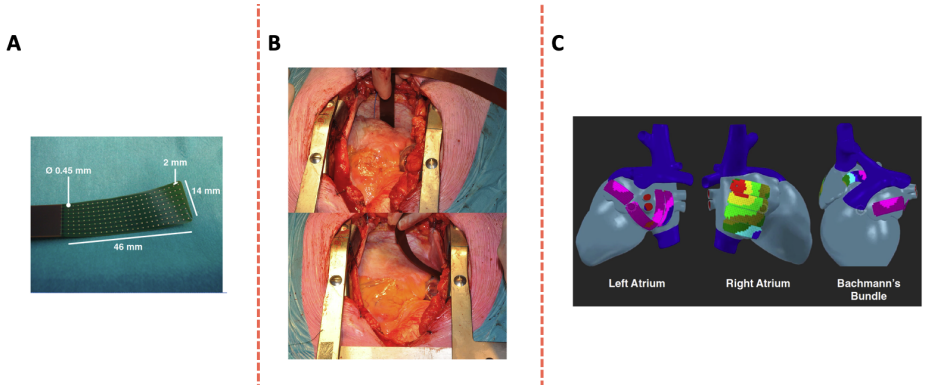

Figure 2.8: Mapping procedure, A) mapping electrode array, B) the placement of the electrode on the surface of the heart during the open heart surgery, C) different mapping locations [56].

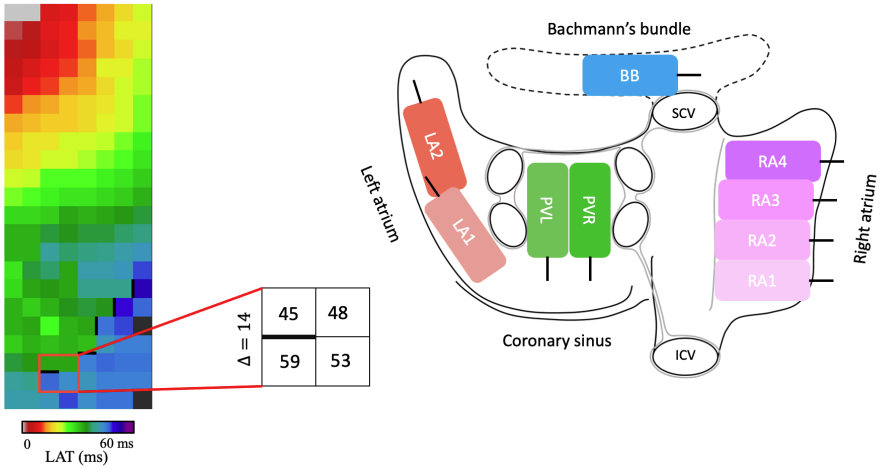

Figure 2.9: Atrial mapping scheme and activation map, left side: Activation map and the LAT on an area with a conduction block, right side: 9 atrial locations in the atrial mapping procedure, Right atrium (RA), left atrium (LA), right pulmonary vein (PVR), left pulmonary vein (PVL), Bachmann's bundle (BB), superior caval vein (SCV), inferior caval vein (ICV)

Local activation time (LAT): As introduced in Section. 2.1.5, the LAT refers to the precise moment when the cell located beneath the electrode becomes activated during cardiac electrical activity. In the context of epicardial recordings with single potential electrograms, the LAT is specifically identified as the time when the steepest descent in the electrogram occurs [57, 58].

Activation map (AM): By employing the epicardial electrode array, a valuable tool is available for constructing an activation map. This map is essentially a matrix that contains the LAT of the atrial potential at each recorded electrode site. To create the activation map, all LAT values are compared to the LAT of the earliest electrode, which establishes a reference point, typically set to 0. In Fig. 2.9 on the left panel, an activation map is shown. Each specific color in the color-coded map shows the LAT measured at the electrode in the rectangular electrode array. The numbers reported on the map are in milliseconds. The activation map uses colors, with varying colors indicating the different activation times. The colors begin with white, signifying the earliest activation, and progress through shades until reaching dark purple, indicating the latest activation. This visual representation enables researchers and clinicians to observe and analyze the spatiotemporal patterns of electrical activation across the heart's epicardial surface.

Conduction block (CB): Conduction block (CB) refers to an impairment in the normal propagation of electrical activity within the heart. When a conduction block occurs, the electrical signals cannot propagate through the affected region as expected. To assess the presence of a conduction block, researchers and clinicians measure the difference between the LAT of two adjacent electrodes. If this difference, denoted as Δ (Fig. 2.9), is greater than or equal to 12ms, it indicates the presence of a conduction block, and is marked with a heavy line.

Fig. 2.10 shows the activation maps during sinus rhythm and atrial fibrillation. The wavefront propagation is shown with black arrows, and conduction blocks are shown with thick black lines. It can be seen that during SR, there is a single wavefront direction, while during AF, multiple wavefront directions are observed. Furthermore, there are a higher number of conduction blocks in AF than in SR.

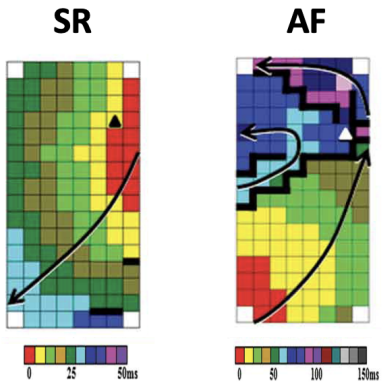

Figure 2.10: Activation maps during, left: SR, right: AF. The thick black lines in the activation maps denote CB [59].

2.6. CONCLUSION

This chapter introduced the fundamental knowledge needed for reading this thesis. Furthermore, we briefly explained the data measurement system used in this project, including multi-lead ECG and high-resolution epicardial mapping.This investigation aims to help us with the severity detection of AF. By analyzing the heart's surface and progressing to the cellular level, we gain valuable insights into the contributing factors and complexities that govern AF. In the next chapter, we start addressing the first research question regarding the severity detection of atrial fibrillation using multi-lead ECG.

3

SEVERITY DETECTION OF ATRIAL FIBRILLATION: PAROXYSMAL VS PERSISTENT

In the previous chapter, we explained different types of atrial fibrillation. Severity detection could be started by distinguishing between SR and AF, which has been done in several studies [38, 51]. However, the challenges of AF severity detection are more pronounced when patients develop different degrees of abnormality, known as types of AF. Two main types of AF are defined as paroxysmal and persistent AF. They are distinguished by the duration of an AF episode. In this chapter, we present a method to discriminate between the signal characteristics of paroxysmal and persistent patients, based on a multi-lead ECG signal recording. The primary objective is to develop a method to extract a template pattern based on the morphology of each type of AF (here, i.e., paroxysmal and persistent AF). For this purpose, we construct a tensor of the atrial activity of different heartbeats and channels. A canonical polyadic decomposition with rank 2 is computed from this tensor and the resulting loading vectors describe the characteristics of paroxysmal and persistent AF in three dimensions: time, heartbeat and channel. The time loading vector reveals the pattern of a single P wave or abnormal AF patterns. The heartbeat loading vector shows whether the pattern is present or absent in a specific beat. The results can be used to distinguish between the patterns in paroxysmal AF and persistent AF.

3.1. INTRODUCTION

In a normal person, the electrical activity of the heart starts from the sinoatrial (SA) node and propagates to the atrioventricular (AV) node which creates regular beats. However, during AF, impulses from other sites in the atrium generate irregular beats

This chapter is based on a paper published as "H. Moghaddasi, A. J. van der Veen, N. M. S. de Groot, and B. Hunyadi, *Tensor-based Detection of Paroxysmal and Persistent Atrial Fibrillation from Multi-channel ECG*, 28th European Signal Processing Conference (EUSIPCO), pp. 1155-1159, 2020, IEEE."

which change the signal morphology as well as the heart rate. The clearest feature of AF in an electrocardiogram is the irregular R-R interval during the AF episode. Two main types of AF are denoted as paroxysmal and persistent AF. In paroxysmal AF, irregular beats start suddenly and the heart rhythm goes back to the normal rhythm by itself. Episodes of AF occur occasionally and last between 30 seconds and 7 days. Atrial premature beats (APB) can also lead to paroxysmal AF. APB happens when a site in the atrium depolarizes before the SA node and subsequently triggers a heartbeat. Wallmann et al. [60] derived that frequent APB can lead to AF. They observed that if the number of APB is higher than 70 in 24 hours, the probability of AF increases by 28% in stroke patients. In persistent AF, the irregular beats last more than 7 days and do not terminate by themselves. However, this classification is not always very practical or insightful as one would have to measure for 7 days, and it does not describe the severity. This motivates to search for a more practical classification approach.

Currently, AF diagnosis is based on the surface ECG and Holter monitoring [61]. Holter monitoring is a continuous measurement of the heart's electrical activity, typically from the body's surface. In the severity detection, some works, such as [10, 62], only selected the AF episodes of an ECG signal for the classification. However, between 25% and 60% of AF cases are paroxysmal AF, which have both SR and AF episodes in the recorded ECG signal. Moreover, most automatic detection methods work on a single channel ECG [63]. A multi-channel ECG has spatiotemporal information, which is helpful in the AF analysis.

In this chapter, we present a novel method to distinguish between paroxysmal and persistent AF based on characteristic patterns observed in a multi-lead ECG. A multi-channel ECG consists of temporal information from different heartbeats and different channels. After segmentation, we stack this information in a tensor (high dimensional matrix). A tensor decomposition factors the tensor into lower-dimensional components (loading vectors), which approximate the original tensor. Tensors have been widely used in various cardiac applications. Detection and localization of myocardial infarction (MI) [64], ECG data compression [65], irregular heartbeat classification [66], and detection of T-wave alternans [67] are examples of these researches in cardiology. Previously, Giernaert et al. [68] proposed to use a multilinear singular value decomposition (MLSVD) for the classification of short periods of ECG signals into AF or SR. However, both episodes are present when we analyze longer periods, as is necessary for detecting paroxysmal AF. If an algorithm or physician only looks at the SR segment of the signal, the AF would not be detected.

Therefore, we concentrate on long-duration AF patient data and propose a tensor-based method to extract characteristics of paroxysmal AF and persistent AF. The advantage of our work is that the proposed method is able to compress a very long ECG signal into three loading vectors, which can also reveal the short episodes of AF. Moreover, the tensor analysis shows that each type of AF (paroxysmal, persistent) can be further decomposed into two sub-groups (type A, type B), which represent discriminant features of paroxysmal AF and persistent AF. The loading vector also allows us to estimate (and generalize) the AF burden, which is a widely

used parameter to assess the severity of AF. AF burden is defined as the time ratio of the AF episode duration divided by the total recording duration [69]. Indeed, the second loading vector could be used for AF burden estimation by decomposing the original tensor.

3.2. METHODOLOGY

3.2.1. DATA ACQUISITION

We use ECG telemetry data collected at Erasmus Medical Center (EMC) from 13 patients, 6 with paroxysmal AF and 7 with persistent AF. The data are standard 12-lead ECG signals that last 72 hours and are labeled paroxysmal AF or persistent AF by clinicians. All ECG signals are recorded with a sampling frequency of 200 Hz. This chapter will use the chest leads denoted as $V1-V6$. The ECG recordings contain noise from power-line, electrode connections, breathing artifacts, and electromyography interference. Hence, a band-pass filter with a cutoff frequency of 0.33 Hz to 30 Hz is applied on all six channels. Next, the signals are also normalized in amplitude to have values between -1 and $+1$. The resulting normalized signal is denoted by $s_n(t)$, where subscript n indicates that the signal is normalized.

3.2.2. SEGMENTATION

The ECG of a normal heartbeat consists of three main segments: the P wave, the QRS complex, and the T wave. The P wave represents atrial depolarization during a cardiac cycle, and analyzing this part will help us to study atrial activity. However, during AF, rapid fibrillatory waves of atrial activity or the absence of a P wave are recorded instead of the P wave. Hence, we segmented the ECG signal from the end of the T wave (T_{end}) to the start of the QRS complex (QRS_{start}) [70] to concentrate on the most important part of the ECG signal from the AF point of view.

We applied a Hilbert transform (HT) to segment the ECG signal in this work. The use of HT in ECG analysis was first presented by Bolton and Westphal [71]. Benitez et al. [72] used a Hilbert transform of the first differential of the ECG to locate the R peak in the QRS complex. Varghees and Ramachandran [73] showed that an HT is useful for detecting the boundaries of the local waves in the signal. They proposed an HT for heart sound activity detection, and we implemented the same pre-processing steps to detect the boundaries of the local waves in the ECG signal.

Since we aim to find the boundaries of the local waves with high amplitude (T wave and QRS complex), we set an adaptive threshold based on the standard deviation σ_{s_n} of the normalized signal $s_n(t)$ (suppressing the P wave and fibrillatory waves in the segmentation). Hence, the thresholded signal is computed as

$$s_{th}(t) = \begin{cases} 0, & s_n(t) < \sigma_{th} \\ s_n(t), & \text{otherwise} \end{cases} \tag{3.1}$$

After analyzing an arbitrary short segment of each patient, we set $\sigma_{th} = 0.2\sigma_{s_n}$.

Let $\hat{s}_{th}(t)$ be the HT of $s_{th}(t)$, then the analytical signal representation of the thresholded signal is computed as

$$s_a(t) = s_{th}(t) + j\hat{s}_{th}(t) = A(t)e^{j\varphi(t)} \tag{3.2}$$

where $s_a(t)$ denotes the analytical signal of the thresholded signal, $A(t)$ and $\varphi(t)$ are the amplitude and the instantaneous phase which are computed as

$$A(t) = \sqrt{s_{th}^2(t) + \hat{s}_{th}^2(t)} \tag{3.3}$$

$$\varphi(t) = \tan^{-1}\left(\frac{\hat{s}_{th}(t)}{s_{th}(t)}\right). \tag{3.4}$$

As can be seen in Fig. 3.1, the phase is between $-\frac{\pi}{2}$ and $+\frac{\pi}{2}$ [74]. It was noted in [73] that a negative to positive phase angle change corresponds to a local peak point of the thresholded signal. So, in the instantaneous phase waveform, the zero-crossing point is determined by checking the sign of the samples at time t and $t+1$. The detected zero-crossing points in the phase angle then correspond to the location of the R peak or the T peak.

In the next step, the peak locations are divided into two groups as R peaks and T peaks. By analyzing all data, a threshold c is defined as

$$c = 0.75\max(s_{th}(t)) \tag{3.5}$$

Let t_{peak} be the location of a peak point as detected from the previous step. If $s_{th}(t)$ at $t = t_{peak}$ is higher than c, then t_{peak} is classified as $t_{R_{peak}}$, otherwise, it would be $t_{T_{peak}}$. The constant 0.75 was determined empirically based on a subset of the ECG data, and it is considered to be able to detect the varying-amplitude R peaks in the ECG sequence.

According to the instantaneous phase of the analytical signal, the boundaries of the local waves in the ECG signal are determined by the positive-slope line. In Fig. 3.1, the filtered signal, thresholded signal and the instantaneous phase of the thresholded signal are shown. As can be seen in Fig. 3.1 B), the boundaries of a T wave and a QRS complex are depicted by $T_{start} - T_{end}$ and $QRS_{start} - QRS_{end}$, respectively. It can be seen in Fig. 3.1 C) that the QRS complex and T wave start from $-\frac{\pi}{2}$ radian and end at $+\frac{\pi}{2}$ radian. Thus, the starting point of the positive slope is determined by checking the amplitude of the phase in samples from $t_{R_{peak}}$ backward. The first location for which the amplitude of the phase is $-\frac{\pi}{2}$ is declared as the starting point of the QRS complex. Similarly, the end point of the positive slope is determined by checking the amplitude of the phase in samples from $t_{R_{peak}}$ onwards. The first location for which the amplitude of the phase is $+\frac{\pi}{2}$ is declared as the end point of the QRS complex. This algorithm repeats for each T wave and it starts from $t_{T_{peak}}$.

Based on the results, we observed that the detected boundaries of local waves slightly differ from the true boundaries. This error is due to the use of the threshold for low-amplitude signals. The duration of the boundary location error is approximately 20 ms. So, we considered a 10 ms time interval after the T_{end} and 10 ms before QRS_{start} to correct the time-location error. The same $T_{end} - QRS_{start}$ intervals are selected from all channels and stored for further analysis.

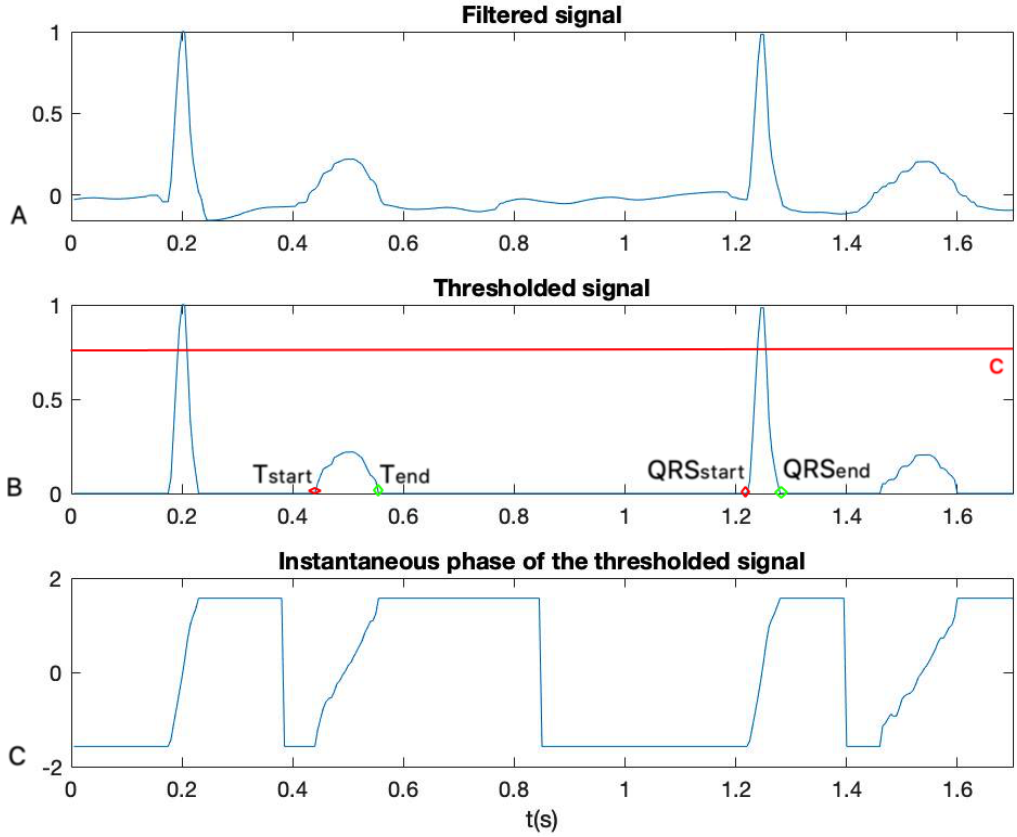

Figure 3.1: Segmentation of the ECG signal, A) Filtered signal B) Thresholded signal C) Instantaneous phase of the signal

3.2.3. DYNAMIC TIME WARPING

A normal heart rate is not entirely constant as cardiac cycles have slightly different lengths. This situation intensifies in cardiac arrhythmia which has uneven cardiac cycles. Hence, the segmented ECG signals in all heartbeats of a single channel do not necessarily have the same length. Therefore, for building a tensor and after that computing a tensor decomposition (details will be explained in Section 3.2.4 and Section 3.2.5), we need to align the segments. Here, alignment means finding a mapping function that can minimize the distance between the two time series. We used dynamic time warping (DTW) to align two segmented ECG signals which correspond to two heartbeats onto the same number of samples. The DTW algorithm is applied based on the dynamic programming techniques explained in [75]. The goal of DTW is to minimize the total distance between two sequences of data. Hence, it searches for an alignment path that minimizes the total cost of

alignment[1].

In channel one, the distance is calculated between all segments. Then, we construct a matrix consisting of the distances from all segments of channel one. This matrix shows two groups of segments in the recorded signals based on the measured distance. Thus, to minimize the distance, we define the mean value of the matrix as a threshold and divide segments into two groups accordingly. In the next step, each group's alignment method is repeated separately. As a result, we obtain aligned ECG segments from channel one with the same length. Then, we align a segment of channel two with the aligned segments of channel one and repeat the algorithm for other beats of channel two. The algorithm is repeated for other channels similarly. As a result, we have aligned segments with the same length in all beats and all channels.

3.2.4. TENSOR CONSTRUCTION

A tensor is a generalization of a matrix to higher dimensions. While a single channel ECG can be stored in a vector (one dimension), the segments of an ECG can be stored in a matrix (two dimensions). More specifically, if the length of $T_{end}-QRS_{start}$ segment is L samples and the number of heartbeats in a single-channel is M, we can create a matrix of size $L \times M$ in which each column shows a heartbeat and each row shows the time. The same is done for other channels and the resulting matrices are stacked behind each other to construct a third-order tensor with three dimensions, namely time, heartbeat and channel. The construction of the third-order tensor $\mathscr{X} \in \mathbb{R}^{L \times M \times V}$, where V denotes the number of channels, is illustrated in Fig. 3.2.

3.2.5. TENSOR DECOMPOSITION

In the ECG signal, there are normal heartbeats and AF episodes. Here, we assume that a certain temporal pattern, present with different amplitudes on different heartbeats and channels, characterizes normal heartbeats. Further, during AF episodes, it is assumed that a different pattern is present, which is scaled in different heartbeats and channels. So, the tensor $\mathscr{X}$ can be approximated by a canonical polyadic decomposition (CPD) where each rank-1 component describes one pattern [76]. The first loading vector describes the time course of the pattern, while the

[1] To elaborate on the DTW algorithm, let us consider two time series as $\boldsymbol{x} = [x_1, x_2, \cdots, x_n]$ with n samples and $\boldsymbol{y} = [y_1, y_2, \cdots, y_m]$ with m samples. Then, the distance between two samples of these time series can be computed as

$$d(x_i, y_j) = |(x_i - y_j| \tag{3.6}$$

The accumulated distance is calculated as

$$\boldsymbol{D}(i,j) = \min\left[\boldsymbol{D}(i-1,j-1), \boldsymbol{D}(i-1,j), \boldsymbol{D}(i,j-1)\right] + d(x_i, y_j) \tag{3.7}$$

Therefore, DTW aims to minimize the total cost of alignment by choosing an optimal path based on the $\boldsymbol{D}$ matrix [75].

This matrix contains the optimal path, which creates the same length for both time series. After constructing the $\boldsymbol{D}$ matrix according to Eq. 3.7, to find this optimal path, the DTW algorithm starts from the element $\boldsymbol{D}(n,m)$ and searches for the minimum element in its neighboring area (i.e., $\boldsymbol{D}(i-1,j)$, $\boldsymbol{D}(i,j-1)$, and $\boldsymbol{D}(i-1,j-1)$) and selects the minimum one. The algorithm is repeated until it reaches the $\boldsymbol{D}(1,1)$ element. As a result, the path between $\boldsymbol{D}(m,n)$ and $\boldsymbol{D}(1,1)$ will be the optimal path.

second and third loading vector shows how this pattern is scaled over the beats and channels. The CPD is defined as

$$\mathcal{X} = \sum_{r=1}^{R} \boldsymbol{a}_r \circ \boldsymbol{b}_r \circ \boldsymbol{c}_r + \mathcal{E} \tag{3.8}$$

where $(\boldsymbol{a}_r, \boldsymbol{b}_r, \boldsymbol{c}_r)$ are the loading vectors of component r and "$\circ$" denotes the outer

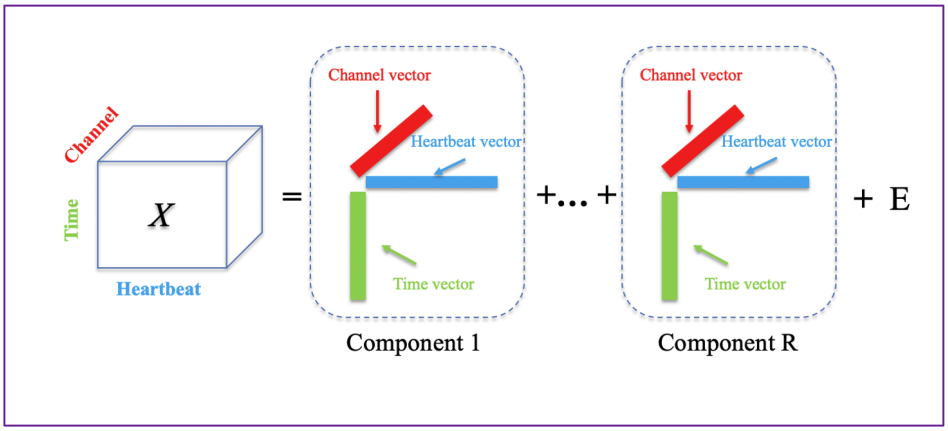

Figure 3.2: Tensor construction and CPD decomposition

product [77]. The CPD approximates a tensor into a sum of R rank-1 components. The rank of the tensor is determined by the smallest R for which $\mathcal{E} \approx 0$ (Fig. 3.2). An important issue for the CPD is its uniqueness. It is clear from the definition of the CPD that the factor matrices can only be unique up to permutation and scaling. More precisely, define first, second and third factor matrices of a third-order tensor $\mathcal{X}$ as $\boldsymbol{A} = [\boldsymbol{a}_1, \cdots, \boldsymbol{a}_R]$, $\boldsymbol{B} = [\boldsymbol{b}_1, \cdots, \boldsymbol{b}_R]$, and $\boldsymbol{C} = [\boldsymbol{c}_1, \cdots, \boldsymbol{c}_R]$. The CPD is also written as $\mathcal{X} = [\boldsymbol{A}, \boldsymbol{B}, \boldsymbol{C}]_R$. Then, the CPD is unique if $\mathcal{X} = [\boldsymbol{A}, \boldsymbol{B}, \boldsymbol{C}]_R = [\overline{\boldsymbol{A}}, \overline{\boldsymbol{B}}, \overline{\boldsymbol{C}}]_R$ implies that an $R \times R$ permutation matrix $\boldsymbol{\Pi}$ and nonsingular diagonal matrices $\boldsymbol{\Lambda}_A$, $\boldsymbol{\Lambda}_B$,and $\boldsymbol{\Lambda}_C$ exist such that

$$\overline{\boldsymbol{A}} = \boldsymbol{A}\boldsymbol{\Pi}\boldsymbol{\Lambda}_A, \quad \overline{\boldsymbol{B}} = \boldsymbol{B}\boldsymbol{\Pi}\boldsymbol{\Lambda}_B, \quad \overline{\boldsymbol{C}} = \boldsymbol{C}\boldsymbol{\Pi}\boldsymbol{\Lambda}_C, \quad \boldsymbol{\Lambda}_A\boldsymbol{\Lambda}_B\boldsymbol{\Lambda}_C = \boldsymbol{I}_R \tag{3.9}$$

Conditions for uniqueness of the CPD were derived by Kruskal [78] for third-order tensors and Sidiropoulos and Bro [79] for higher-order tensors. A sufficient condition for uniqueness is that $\boldsymbol{A}$ and $\boldsymbol{B}$ are full rank and $\boldsymbol{C}$ does not contain collinear columns.

3.2.6. RANK ANALYSIS

In the CPD model, firstly the number of components R should be determined. In the presence of noise, there is no direct algorithm to find R. In order to establish a suitable R, we decompose the tensor into the different number of components and calculate the residual error by comparing the reconstructed tensor to the original

tensor $\mathscr{X}$. Then, the relative error is computed by dividing the Frobenius norm of residual error to the Frobenius norm of the original tensor. For our data, we reconstruct the tensor at each step considering r components, where r varies between 1 and 10. The relative errors for a patient with paroxysmal AF and a patient with persistent AF are shown in Fig. 3.3. For both patients, the maximum error reduction happened when the rank was increased from 1 to 2 which means rank 1 is able to extract the dominant component of the signal. However, due to our prior knowledge, the P wave is replaced with fibrillatory waves or the absence of a P wave during AF. Therefore, rank 1 is too small, and more than one component is needed to extract these morphological characteristics of AF. Here, we choose rank 2 empirically based on the visual analysis of the components. Next, we study paroxysmal and persistent AF datasets and present two examples for each type of AF.

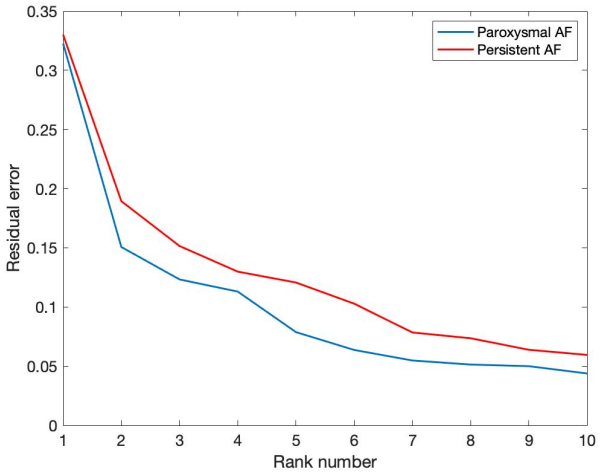

Figure 3.3: Relative error of tensor decomposition by reconstructing the tensor by varying r between 1 and 10

3.3. RESULTS

We apply the proposed methods to the clinical data obtained from paroxysmal and persistent AF patients, demonstrating the characteristics of AF for different severity levels of patients. For each severity level, i.e., paroxysmal and persistent AF, we will show two examples of loading vectors. The examples will show that we can use these to differentiate between paroxysmal and persistent AF.

3.3.1. PAROXYSMAL ATRIAL FIBRILLATION

Fig. 3.4 shows the CPD components for two patients with paroxysmal AF. Column one shows the first loading vector which represents a template for $T_{end} - QRS_{start}$

segment. Column two shows the variation of the loading vector one in the different heartbeats. Note that the algorithm was applied to the whole telemetry data but in Fig. 3.4 and Fig. 3.5, we show only 100 beats. The third loading vector corresponds to the relative strength (and polarity) of the extracted pattern (first loading vector) across channels. For paroxysmal AF, we observe two distinct patterns which we call type A and type B.

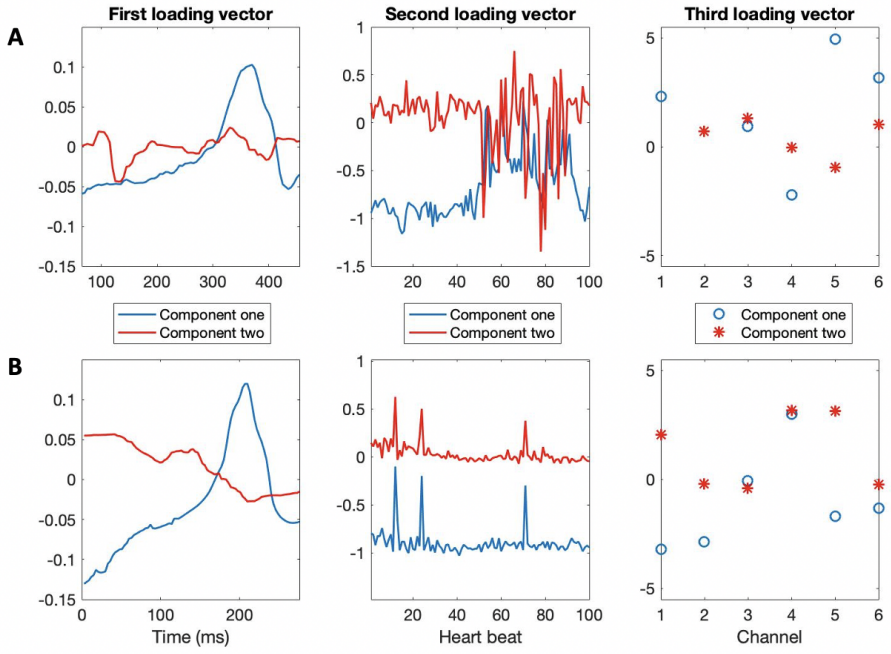

Figure 3.4: CPD loading vectors for two paroxysmal cases, A) type A; B) type B

Fig. 3.4 A) shows an example of type A. Looking at the first loading vector, component one (in blue) is recognized to have a morphology similar to a single P wave contributed by the SR part, while component two (in red) is recognized as a template for fibrillatory waves. The second loading vectors show the magnitude of the extracted patterns across beats. From beat number 48, the magnitude of component two is increasing which shows the starting point of fibrillatory waves. Fibrillatory waves continue until beat number 92, after which normal sinus rhythm is restored. This can also be seen from the magnitude of component one in the second loading vector. The second loading vector is also useful to find the AF burden. From this vector, the duration of AF episodes, the number of AF episodes, and the percentage of time the patient is in AF can be monitored. To do so, one could divide the number of heartbeats where the patient develops component two (i.e., AF component) by the total number of heartbeats.

Fig. 3.4 B) shows the components for an example of type B. Component one

(in blue) of the first loading vector shows a single P wave while component two (in red) illustrates a pattern for the absence of a P wave which could be related to atrial premature beats. By analyzing the second loading vector, it is clear that the magnitude of component one is mostly higher than component two which is close to zero except for three heartbeats. In beat number 10, 25 and 72, the magnitude of component two is higher than component one, which is close to zero. This means that in these 3 beats the normal P-wave (first loading vector of the second component) is absent. By counting the number of atrial premature beats as explained in Section 3.1, a total of 138 atrial premature beats could be detected in a total length of 24 hours. So, this could be the characteristics of type B patterns in paroxysmal AF patients related to the APB. Comparing types A and B, we judge that it is more clear to estimate the AF burden for type B, while type A poses a more significant challenge, requiring an appropriate thresholding approach. In the dataset, two patients have patterns of type A and four patients have patterns of type B.

3.3.2. PERSISTENT ATRIAL FIBRILLATION

Fig. 3.5 shows the CPD components of two patients with persistent AF. As described in Section 3.1, AF is characterised by fibrillatory waves or the absence of a P wave. Looking at Fig. 3.5, we observe two distinct patterns of persistent AF, which we also call type A and type B (they are not related to the previous A and B), that depict a similar characteristic pattern to AF. In Fig. 3.5 A), patterns of type A are observed. The first loading vector shows two components. Component one (in blue) is a template of fibrillatory waves and component two (in red) is a template for the absence of P wave. The second loading vector gives information about the distribution of fibrillatory waves as well as the absence of P wave. By analyzing two components of the second loading vector, it is determined that most beats represent the pattern of the fibrillatory wave while some beats have an absence of a P wave.

In case two, fibrillatory waves and the absence of a P wave are shown as components of the first loading vector, similarly. The difference between type A and type B is in the distribution of components. In type B, the number of beats with a fibrillatory pattern are almost the same as the beats with the absence of a P wave pattern. These features are considered as patterns of type B in persistent AF. In other words, the most discriminant feature of type A and type B is the percentage of fibrillatory waves compared to the absence of P waves. For type B, the percentage of fibrillatory waves is higher than for type A. In the dataset, three patients have patterns of type A and four patients have patterns of type B.

3.4. DISCUSSION

We presented a novel method to find specific patterns in long multichannel ECGs to reveal differences between paroxysmal AF and persistent AF. The most important difference between these conditions is that in paroxysmal AF, SR (that include P-waves) and AF episodes (without P-waves) both are present, while in the persistent AF, SR (i.e. P-waves) are almost absent. This difference can only be established using long ECG recordings. Reading long-term multichannel ECG is time-consuming and

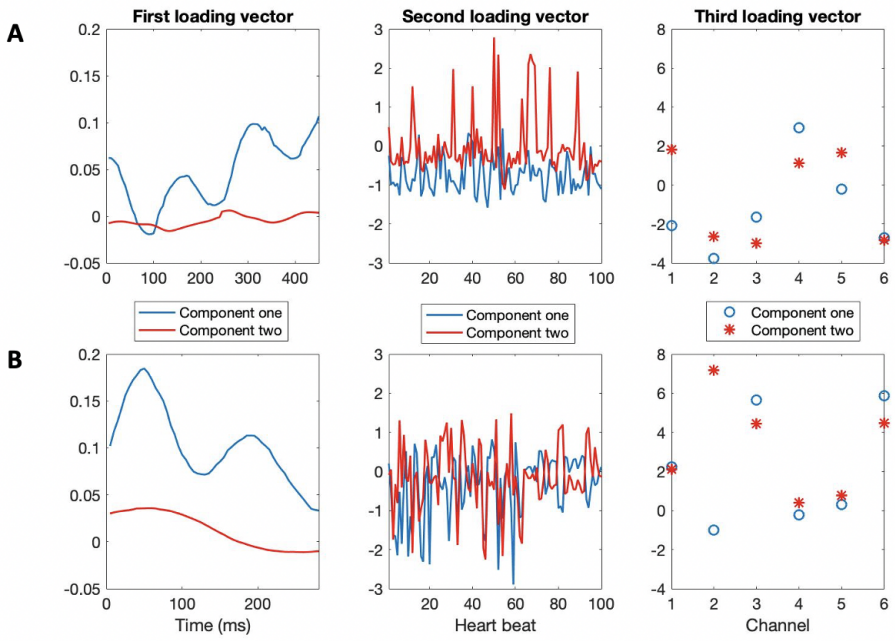

Figure 3.5: CPD loading vectors of in two persistent cases, A) type A; B) type B

cumbersome. Our approach provides a compact and easy-to-interpret summary of all the patterns present in the ECG in just 3 figures that visualize the loading vectors: the most prevalent patterns, their presence in the consecutive waves, and their relative strength in the different channels. Paroxysmal and persistent AF can be differentiated directly from the first loading vector, based on the presence or absence of a loading vector resembling a P-wave pattern.

It is important to note that while the proposed method is able to distinguish between persistent AF and paroxysmal AF, in borderline cases, an improvement in the method is needed. For example, if the AF episodes in a paroxysmal patient last slightly less than 7 days, the SR episode would be too short to be extracted by the CPD decomposition. In this case, we may observe components similar to the first loading vectors of persistent AF patients without a P wave morphology. Moreover, the second loading vector of the CPD can also be useful in the severity detection of AF. This vector shows the distribution of a single P wave, absence of P wave, or fibrillatory waves. Hence, by analyzing the second loading vector of a large group of labeled data, we can find the relationship between the extracted patterns and the severity of AF.

3.5. CONCLUSION

This chapter presents a tensor-based method to extract characteristics of paroxysmal and persistent AF in long multi-channel ECG signals. Results of patients in both groups reveal that the CPD is able to find components that allow to discriminate between paroxysmal and persistent patients. In the next chapter, we address a more challenging and demanding aspect of AF severity detection, excluding SR episodes and purely focusing on the AF episodes.

4

SEVERITY DETECTION OF ATRIAL FIBRILLATION: *de novo* VS PERSISTENT

In the previous chapter, we developed a method to distinguish between two stages of atrial fibrillation without excluding SR episodes. In this chapter, we go one step further and focus on a more intricate severity detection of AF, specifically focusing on ECG data excluding SR episodes. Due to the progressive nature of AF, timely detection is important and improves life expectancy. Currently, physicians use a surface ECG for AF diagnosis. However, when the patient develops AF, its various development stages due to electrical changes in the atrium are not distinguishable for cardiologists based on visual inspection of the surface ECG signals. Therefore, a first step towards severity detection of AF is to see if from ECG recordings of AF episodes, we can differentiate between short-lasting AF and long-lasting AF.

AF is the most common complication developed after cardiac surgery. Patients that did not have AF before but develop it for the first time are classified as *de novo* post-operative AF (POAF). We consider that these cases are a good model for short-lasting AF, while long-lasting AF can be represented by cases with persistent AF. In this chapter we consider a binary severity detection of AF for these two specific types of AF. We will propose a method that combines three sets of discriminative features based on fundamentally different aspects of the multi-channel ECG data, namely based on the analysis of RR intervals, a greyscale image representation of the vectorcardiogram, and a frequency domain representation of the ECG. Due to the nature of AF, these features are expected to capture both morphological and rhythmic changes in the ECGs.

This chapter is based on a paper published as "H. Moghaddasi, R. C. Hendriks, A. J. van der Veen, N. M. S. de Groot, and B. Hunyadi, *Classification of De novo post-operative and persistent atrial fibrillation using multi-channel ECG recordings*, Computers in Biology and Medicine, 143, 105270, 2022."

4.1. INTRODUCTION

AF is described by uncoordinated atrial activity that is represented on the ECG by irregular RR intervals [2]. Cardiology guidelines classify AF based on the duration of AF episodes [80]. According to this definition, in paroxysmal AF, an AF episode lasts between 30 s and 7 days and returns to sinus rhythm (SR) by itself, while in persistent AF, an AF episode lasts more than 7 days and it is not self-terminating [27, 28, 80]. Interestingly, atrial fibrillation is the most common complication after cardiac surgery in patients who never experienced AF [81]. These patients are commonly referred to as *de novo* post-operative AF (POAF) patients. The specific mechanism of *de novo* POAF is not yet fully understood. Hypotheses state that the patients develop AF after cardiac surgery due to reasons such as pericardial inflammation, atrial stretch and disharmony in the autonomic nervous system, to name a few [82]. All these factors shorten the refractory period of the atrial cells, making the wavelets propagate to the atrioventricular (AV) node at a higher rate, resulting in fast and irregular ventricular contraction [81].

Currently, the gold standard to diagnose AF is considered to be the interpretation of the 12-lead ECG by a trained physician [7]. However, based on visual inspection of ECG signals with AF episodes only, it is impossible for cardiologists to distinguish between *de novo* POAF and persistent AF. Furthermore, the stage of AF (severity of the arrhythmogenic substrate) when the patient develops AF cannot be determined by visual inspection of the ECG by physicians. In other words, AF episodes do not show a visible difference between *de novo* POAF and persistent AF.

The simplest level in the severity detection of AF is to classify ECGs into SR episodes and AF episodes. Scientists addressed this issue by computer-aided diagnosis (CAD) systems. Generally, such machine learning methods can be classified into two main groups as handcrafted- and deep learning-based methods, and in this chapter we will focus on handcrafted features, also called feature engineering. These features are extracted based on prior knowledge which is used in the classifiers. Due to the nature of AF, the handcrafted features can be classified into 4 groups; time-, frequency-, time-frequency and nonlinear-based methods. The time-based features mostly focus on the irregularity in the RR intervals [37] or the discrepancy in atrial activity [38]. The irregularity in the RR intervals is demonstrated by the features which rely on the heart rate variability (HRV) using Poincaré plots [83, 84], density histogram of delta RR intervals [85], entropy measures [86, 87], probability density estimation of the RR interval distribution [88] and calculation of statistics [89–92]. On the other hand, the discrepancy in the atrial activity is evaluated by the P-R interval variability, the P wave morphology similarity measure, the R-R Markov score [93] and absence of a P wave or presence of fibrillatory waves using piecewise linear functions [94].

Beyond this, frequency analysis of the fibrillatory waves is also quite informative. The fibrillatory wave ratio using a power spectral density [39] and fibrillatory wave spectrum [95] are common extracted features in this category. Although time/frequency-based features have the capability of extracting irregularity of RR intervals and fibrillatory waves, techniques based on wavelet transform solve the low frequency/time resolution problem of the previous methods by jointly localizing

in time and frequency. Atrial activity was correctly detected by features extracted from the correlation matrix of the wavelet coefficients [40] and discrete wavelet transform [96]. Furthermore, dynamic characteristics of AF is extracted by features as higher-order spectra (HOS) [97], Hurst exponent, largest Lyapunov exponent (LLE), and fractal dimension [42], quadratic sample entropy and LLE [98].

In contrast to the handcrafted features, most of the deep learning-based methods are independent from the discriminative features [50] or less-dependent on the handcrafted features [51]. At the same time, they provide less insight into the underlying electropathology of AF.

Although there exists extensive research on the classification of SR episodes and AF episodes, this is not directly useful for diagnosing the severity of AF. This is due to the fact that both *de novo* POAF and persistent AF patients can have both SR and AF episodes. In this chapter, we tackle the challenging problem of diagnosing the severity of AF based on AF episodes. There is no clear, visually perceivable difference between an AF episode in a *de novo* POAF patient and an AF episode in a persistent AF patient. Our motivation to address this problem is summarized as follows. First, since *de novo* POAF is the first time that a patient develops AF, comparing its evolution to persistent AF might lead to insights into the exact mechanism of AF and its underlying electropathology. Moreover, being able to differentiate between short-lasting and long-lasting AF could help physicians to learn how to determine the stage of its development. In fact, knowing this is critical for AF treatment. Considering that AF is a progressive disease that can lead to stroke or heart failure, detection and treatment of AF in the early stages will decrease the mortality rate and healthcare costs. In addition, the development stage of AF is crucial for predicting the outcome of the treatment. An example of this is catheter ablation, the standard therapy for AF patients. In the case of paroxysmal patients, the success rate of ablation therapy is between 70% and 80% while for patients with persistent AF, this rate drops to 45-60% [99]. This shows why early detection of AF is of vital importance in the treatment process.

In this chapter, we analyze the AF episodes of long-term multi-channel surface ECG recordings. Our hypothesis is that there is a clear difference between *de novo* POAF and persistent AF. We test this hypothesis by proposing features that can differentiate between these two groups. Analyzing these differences may give us insight into the physiological changes that underlie the occurrence of AF and, subsequently, reveal the underlying differences.

The core of our method therefore consists of careful feature engineering preceding machine learning-based classification. To capture morphological and rhythmic differences, multi-channel ECGs can be analyzed in various ways, e.g., the time domain, the spatial domain, and the frequency domain. We propose three corresponding groups of features. In the time domain, we propose rhythm-based features where we look at the irregularity of the RR intervals, an indirect indicator of the atrial activity. The second set of features is based on the vectorcardiogram. Here we extract joint spatial/temporal aspects of the heart's dynamics in the cardiac cycles. This is implemented based on image descriptors on the 3D structure of the electrical activity of the heart. Finally, in the third group of features, frequency-domain aspects

of the atrial activity during AF episodes are analyzed.

The main novelty of the proposed method is hidden in the feature extraction. Firstly, we have introduced two novel features based on the different usage of autoregressive modeling and dominant frequency. Secondly, to the best of our knowledge, this is the first paper that detects the severity of AF by analyzing vectorcardiogram images using image processing techniques which unveils the new aspects of this disease. Furthermore, from the clinical point of view, we have introduced the first method of classification between *de novo* POAF and persistent AF which had not been done before.

The rest of this chapter is organized as follows. In Section 4.2, we introduce our method including feature extraction, feature reduction and classification. The performance of our proposed method is demonstrated in Section 4.3. In Section 4.4, we analyse the feature values extracted from *de novo* POAF and persistent AF patients, to gain insight into the most essential differences between their underlying physiology. Finally, we draw conclusions in Section 4.5.

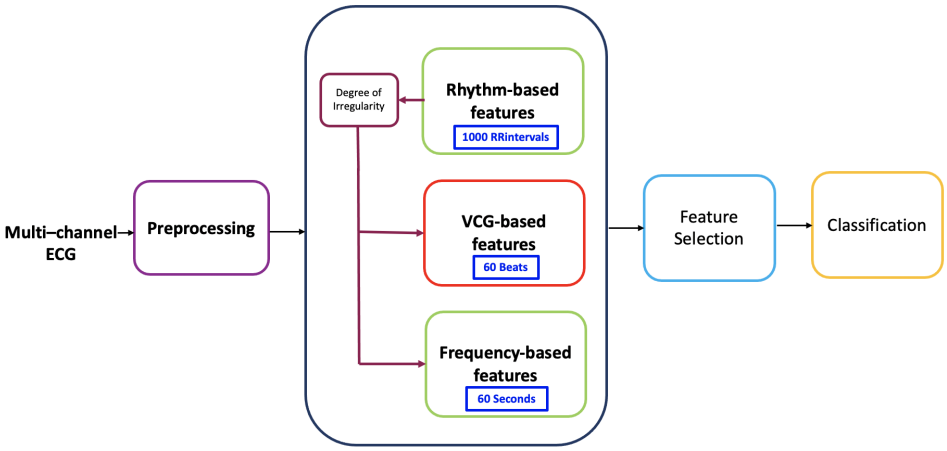

Figure 4.1: Block diagram of the proposed method.

4.2. METHODOLOGY

We hypothesize that differentiating *de novo* POAF and persistent AF can be done by finding features that capture the morphological and rhythmic changes in the ECG signal. With multi-channel ECG data, beat-to-beat variations in morphology are visible in patterns in the vector cardiogram. Rhythmic changes follow from surveying variations in the RR intervals (in time domain), and from analyzing the dominant frequencies corresponding to atrial activity.

In Fig. 4.1 we show a high-level block diagram of our approach outlining the different steps required for classification. The core of this work is the development of features discriminating between *de novo* POAF and persistent AF, as these features

might provide more insight in how the development of AF can be monitored and how the development stage of AF can be determined in more detail. However, as our data originates from continuous recordings, noise and artifacts will be present. Prior to discussing the actual features, we will therefore discuss the data acquisition and the required pre-processing in Sections 4.2.1 and 4.2.2, respectively. As we hypothesize that differentiation between de novo AF and persistent AF lies in morphological and rhythmic beat-to-beat changes, we will develop in Sections 4.2.3–4.2.5 three groups of features capturing these aspects. Subsequently, we discuss the feature selection stage and classification in Sections 4.2.6 and 4.2.7, respectively.

4.2.1. DATA ACQUISITION

We enrolled in total 151 patients of which 99 were categorised as *de novo* and 52 were categorised as persistent AF patients. The telemetry data was collected at the Erasmus Medical Center (EMC). The data consists of 12-lead ECG signals with recording durations between 72 hours and 120 hours, at a sample rate of 200 Hz. All patients were labeled as *de novo* POAF or persistent AF by physicians at the EMC.

4.2.2. PRE-PROCESSING

The process of recording the ECG signals in the telemetry data takes several days per patient. During this period, the ECG leads are connected to the patient's body and it is likely that the leads sometimes get disconnected during the recording. Moreover, breathing artifacts, electromyography interference and power-line interference are other inevitable noise sources. To remove the effect of these perturbations, we filter the data with a Butterworth band-pass filter in the frequency range between 0.33 Hz and 30 Hz [100–102]. In addition, due to the high-amplitude noise, the quality in some segments of the long-term recordings is poor. These segments are therefore excluded from the signal. To do so, we divide the ECG signals in each lead in the pre-processing step into 60s segments and apply the band-pass filter to all segments. For each segment and channel, we estimate the signal-to-noise ratio (SNR) by calculating the power of the denoised signal divided by the power of the residual noise as

$$\mathrm{SNR} = 10\log_{10}\frac{\sum_{n=0}^{N-1} s_d^2(n)}{\sum_{n=0}^{N-1}\left(s(n)-s_d(n)\right)^2} \tag{4.1}$$

where N is the number of samples in a segment, and $s(n)$ and $s_d(n)$ are the original and the denoised signals, respectively. After that, we remove the segments where the ECG has an SNR < 10 dB. Notice that the SNR is determined based on the noise outside the frequency range of 0.33–30 Hz. The retained segments are normalized with respect to the maximum absolute value of the signal, to have an amplitude between -1 and $+1$. For the features which need R peaks detection, we have done another step in the pre-processing. By calculating SNR as in Eq. (4.1) for all ECG channels, we select the ECG channel with the highest SNR for performing R peak detection. Finally, a wavelet-based ECG delineator algorithm [103] is applied to the filtered ECG signal to detect the R peak in each cardiac cycle.

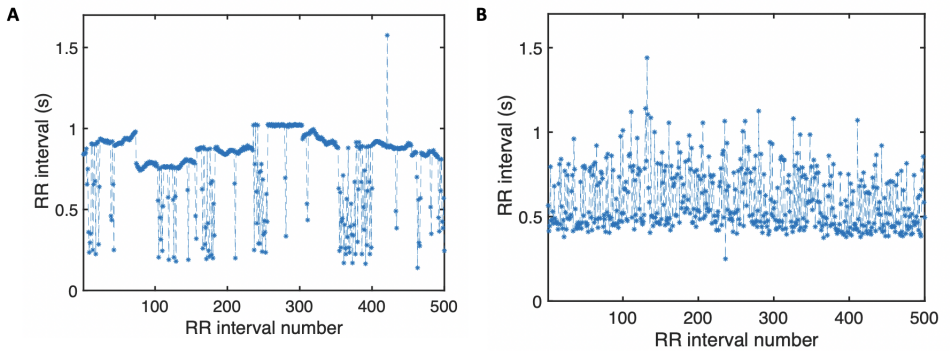

Figure 4.2: RR intervals for A) *de novo* POAF, B) persistent AF.

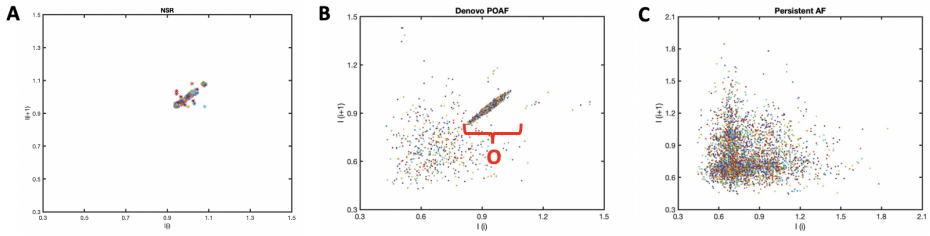

Figure 4.3: Poincaré plots: A) SR intervals in *de novo* POAF, B) irregular intervals in *de novo* POAF, C) persistent AF.

4.2.3. RHYTHM-BASED FEATURES

One way in which AF affects the ECG is by increasing the irregularity of the RR intervals. Generally these intervals become shorter and less predictable. Fig. 4.2.A shows an example of the RR intervals of a *de novo* POAF, and Fig. 4.2.B shows an example of the RR intervals of a persistent AF. For this figure, for the *de novo* POAF patient a data segment was selected where AF is present. It is clearly seen that regular (and slower) beats are interlaced with irregular and faster beats. For persistent AF, the regular beats are absent.

Another way to visualize this is through Poincaré plots [83]. This is a recurrent scatter plot that allows to judge the correlation structure present in a time series, in this case a sequence of N RR intervals with the individual lengths given by $I_1, I_2, \cdots, I_N$. The plot shows the points $[I_k, I_{k+1}]$, for $k = 1, \cdots, N-1$. As example, Fig. 4.3.A shows a Poincaré plot of a SR episode of a *de novo* POAF patient, Fig. 4.3.B shows a Poincaré plot of an AF episode a *de novo* POAF patient, and Fig. 4.3.C shows a Poincaré plot of a patient in persistent AF. Clearly, in the latter case the Poincaré plot does not represent any specific pattern and the points have an irregular distribution, while during *de novo* POAF, two different patterns are observed. In the area indicated by the symbol O, points are concentrated on an ellipsoid oriented

around a diagonal line (for which $I_k = I_{k+1}$), while for the remaining points in the Poincaré plot no regular pattern is observed. The latter cloud of points is absent for the SR episodes.

In the related literature, several parameters have been proposed to describe the structure in such plots [104], often referred to as SDNN (standard deviation of NN intervals i.e., the standard deviation of I_k, with outliers removed), SD1 and SD2 (the axis lengths of a fitted ellisoid), SDSD (the standard deviation of successive differences $I_{k+1} - I_k$), and RMSSD (the root mean square of successive differences), etc. As discussed in [105], these are all related, and we offer the following perspective from statistical system theory to explain this further.

Consider the measured RR intervals $I_1, \cdots, I_N$ as a realization of a wide sense stationary random process. Let $\bar{I}$ denote the sample mean, that is ,

$$\bar{I} = \frac{1}{N} \sum_{k=1}^{N} I_k \,. \tag{4.2}$$

We will work from now on with the zero mean sequence $x_k := I_k - \bar{I}$.

The Poincaré plot is related to the modeling of x_k by a first-order autoregressive (AR) model, AR(1), as

$$x_{k+1} = a\, x_k + e_k \,, \tag{4.3}$$

where e_k is a zero mean Gaussian random process with variance σ^2, and a is the AR coefficient ($|a| \le 1$). If $a = 1, \sigma = 0$, then $x_{k+1} = x_k$ and the RR intervals are constant and perfectly predictable. If $a = 0$, then the RR intervals are completely uncorrelated.

For some upper bound L, not too large, we form the sample autocovariance sequence

$$\hat{r}_\ell = \frac{1}{N-L} \sum_{k=1}^{N-L} x_{k+\ell}\, x_k, \qquad \ell = 0, 1, \cdots, L. \tag{4.4}$$

These are estimates of $r_\ell = E[x_{k+\ell}\, x_k]$. Then the AR(1) model satisfies [106]

$$\left\{ \begin{array}{rcl} r_0 &=& \dfrac{\sigma^2}{1-a^2} \\ r_1 &=& a\, r_0 \end{array} \right. \quad \Leftrightarrow \quad \left\{ \begin{array}{rcl} a &=& \dfrac{r_1}{r_0} \\ \sigma^2 &=& \dfrac{r_0^2 - r_1^2}{r_0^2} \end{array} \right.$$

We can also construct the 2×2 correlation matrix

$$\boldsymbol{R} = \begin{bmatrix} r_0 & r_1 \\ r_1 & r_0 \end{bmatrix} = \frac{\sigma^2}{1-a^2} \begin{bmatrix} 1 & a \\ a & 1 \end{bmatrix}.$$

The eigenvalue decomposition of $\boldsymbol{R}$ can be computed in closed form as

$$\boldsymbol{R} = \frac{1}{2} \begin{bmatrix} 1 & 1 \\ 1 & -1 \end{bmatrix} \begin{bmatrix} \sigma_a^2 & 0 \\ 0 & \sigma_d^2 \end{bmatrix} \begin{bmatrix} 1 & 1 \\ 1 & -1 \end{bmatrix}$$

with

$$\begin{aligned} \sigma_a^2 &= r_0 + r_1 = \frac{\sigma^2}{1-a} \\ \sigma_d^2 &= r_0 - r_1 = \frac{\sigma^2}{1+a} \,. \end{aligned}$$

This latter parametrization is directly visible in the Poincaré plot: for an AR(1) model, the points are scattered on an ellipsoid with center $[\bar{I}, \bar{I}]$, with the long axis in the direction $[1,1]$ with length σ_a, and with the short axis in the orthogonal direction $[1,-1]$ with length σ_d. Further, σ_a is equal to SD1, while σ_d corresponds to SD2, SDSD, and RMSSD.

Thus, we have 3 equivalent parametrizations of the AR(1) model: $(\bar{I}, r_0, r_1)$, $(\bar{I}, a, \sigma^2)$, and $(\bar{I}, \sigma_a, \sigma_d)$.

To measure the irregularity, an index δ is defined as

$$\delta = \frac{\sigma_d^2}{\bar{I}} \tag{4.5}$$

which is the difference of the correlation values with zero and one time lags normalized by the mean of the RR intervals. For regular RR intervals (e.g., SR episodes), it is expected that all the points are located close to a central point which means that δ is almost zero. As the irregularity increases, δ increases. We use this index to filter out the SR episodes in the classification.

At this point, a relevant question is also whether AR(1) is a good model choice at all. We could study the fit to higher-order models, AR(ℓ), for $\ell = 1, \cdots, L$, and related performance metrics such as final prediction error (FPE) [107]. Instead, we will consider more general auto-regressive moving average (ARMA) models. For some p, larger than the model order we wish to select, construct the $p \times p$ Hankel matrix

$$\boldsymbol{H} = \begin{bmatrix} r_1 & r_2 & \cdots & r_p \\ r_2 & r_3 & \cdots & r_{p+1} \\ \vdots & \vdots & \ddots & \vdots \\ r_p & r_{p+1} & \cdots & r_{2p-1} \end{bmatrix}.$$

Then system theory tells us that for an ARMA(ℓ) model, the rank of $\boldsymbol{H}$ is ℓ. For example, for an AR(1) model,

$$\boldsymbol{H} = r_0 \begin{bmatrix} a & a^2 & a^3 & \cdots \\ a^2 & a^3 & a^4 & \cdots \\ a^3 & a^4 & a^5 & \cdots \\ \vdots & \vdots & \vdots & \ddots \end{bmatrix}$$

which is clearly of rank 1. To detect the rank, consider the singular values of $\boldsymbol{H}$ sorted in non-increasing order, $\lambda_1 \geq \lambda_2 \geq \cdots \geq \lambda_p$. If the rank of $\boldsymbol{H}$ is ℓ, then $\lambda_\ell > 0$ while $\lambda_{\ell+1} = 0$.

As feature to detect rank 1 in our data sets, we propose to use $p = 5$, and define the feature

$$\varrho = \frac{\lambda_1}{\lambda_2}. \tag{4.6}$$

If a first order model is a good fit, then $\varrho \gg 1$. Fig. 4.4 shows as example plots of the eigenvalues of $\boldsymbol{H}$ for *de novo* POAF and persistent AF, respectively. It is seen that for *de novo* POAF $\lambda_1 \gg \lambda_2$, while for persistent AF λ_1 is not much larger than λ_2. Thus,

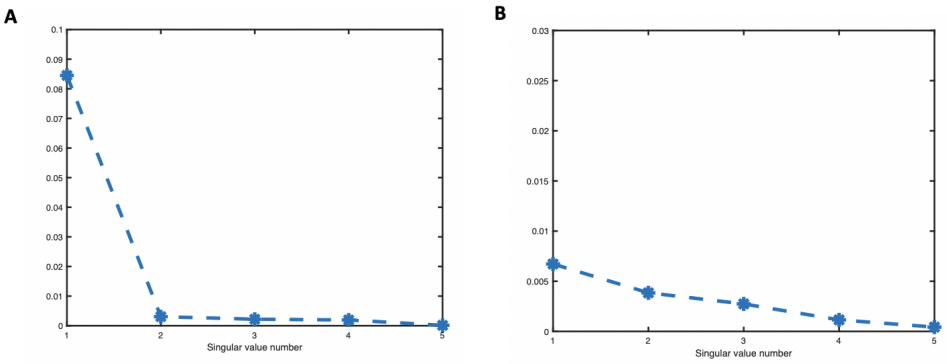

Figure 4.4: Singular values of matrix $\boldsymbol{H}$: A) *de novo* POAF, B) persistent AF.

for *de novo* POAF, ϱ is much larger than for persistent AF, and a rank 1 model seems appropriate. Comparing to Fig. 4.3.B, we expect that points in the narrow ellipsoidal area indicated by the symbol O dominate the model structure.

Altogether, to compute the rhythm-based features, we first exclude the SR episodes by excluding segments for which δ is almost zero (corresponding to a highly regular/ predictable RR interval sequence). By analyzing our dataset, a threshold $\delta > 0.01$ is defined to exclude SR episodes. For the classification, considering the shortest AF episode in our dataset, we used a window that contains 1000 RR intervals (from the most irregular part of the signal as measured by the δ parameter) and extracted four features from the best quality lead: $\bar{I}$, σ_a, σ_d, and ϱ.

4.2.4. VECTOR CARDIOGRAM-BASED FEATURES

In the previous section, we extracted features from the time domain. In this section, we investigate spatial information of the ECG signals.

Different degrees of AF are expected to represent themselves by specific characteristics extracted from the ECG. This becomes even more prominent if we take multiple leads into account, as morphology may vary across different leads. In order to summarize multi-channel ECG information in a compact way, we make use of the vector cardiogram (VCG). The VCG is an alternative representation of the multi-channel ECG information that allows to track the electrical activity of the heart along the three orthogonal body planes: left-right (x), head-to-feet (y) and front-back (z). Using Frank's transformation [108, 109], the 3-lead VCG ($\boldsymbol{v} = [V_x, V_y, V_z]^T$) is obtained using 8 leads out of the 12-lead ECG by

$$\boldsymbol{v} = \boldsymbol{F}\,\boldsymbol{e} \tag{4.7}$$

where $\boldsymbol{e} = [V_1, V_2, V_3, V_4, V_5, V_6, I, II]^T$ and $\boldsymbol{F}$ is a 3×8 transformation matrix derived from Frank's equation [108].

As an example, Fig. 4.5A and Fig. 4.5B show the orthogonal leads as a function of time for an SR episode and an AF episode in a persistent AF patient, respectively.

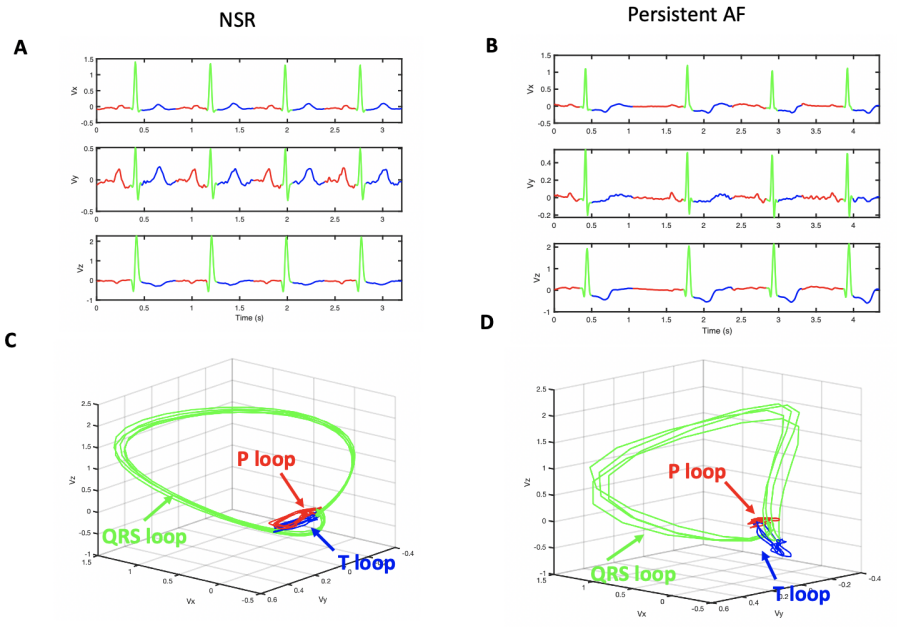

Figure 4.5: A) Orthogonal leads for an SR episode, and B) for a persistent AF patient; C) corresponding 3D VCG for the an SR episode, and D) for the persistent AF patient.

The corresponding 3D VCGs are shown in Fig. 4.5C and Fig. 4.5D. For SR, each cardiac cycle creates a complete P loop (red), QRS loop (green) and T loop (blue). However, for persistent AF, the P loops are not clearly visible, but replaced by a chaotic trajectory before the start of the QRS loops. Moreover, for persistent AF, beat-to-beat variations of the QRS loop are greater than for SR. The most important differences between the 3D VCG of SR and persistent AF are the sub-patterns within the image representing the electrical activity of the heart along the three orthogonal body planes. A suitable discriminator is therefore a feature describing the local patterns in this 3D VCG image.

To capture these differences, we propose to use local binary pattern (LBP) analysis [110] on a segmented version of the 3D VCG image. LBP is an image descriptor that has been successfully used to describe texture in various applications ranging from face detection and detection of facial expressions [111, 112], to diagnosing heart diseases [113, 114].

The main idea behind LBP analysis is to first capture and categorize the local texture of the image around a given pixel using the so-called LBP operator, and subsequently summarize the information from all pixels using a histogram. The LBP operator computes an 8-bit binary code word for each pixel by comparing its grayscale value to its 8 neighbors in a 3×3 neighborhood (see Fig. 4.6). If the intensity of the given pixel is smaller than that of its ith neighbor, the corresponding bit is set to '1', and otherwise it is '0'. In the original LBP algorithm [110], this leads

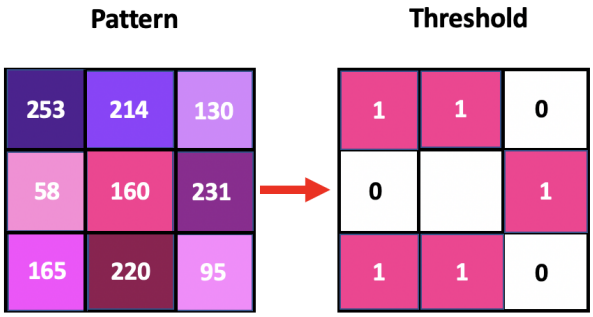

Figure 4.6: LBP operator

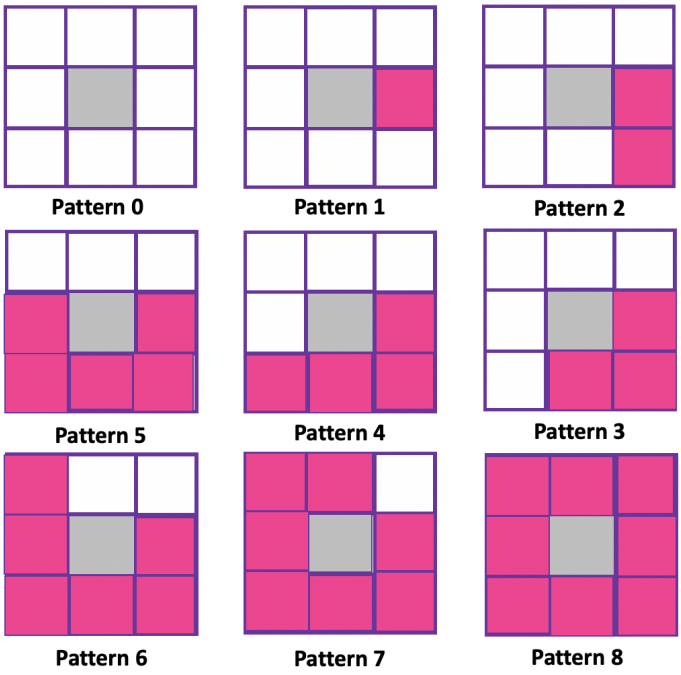

Figure 4.7: URILBP: There are in total 9 possible uniform rotationally invariant local binary patterns.

to a total of 2^8 possible binary patterns. Then, the number of occurrences of each pattern is counted to build a histogram. This histogram describes the distribution of all possible local patterns in the image. However, not all 256 possible patterns are equally interesting. Firstly, many of these patterns can be obtained from each other

by a circular shift (rotation). There are only 36 unique rotationally invariant patterns (see [115] for the visualization of all these patterns). Secondly, it has been shown empirically that a vast majority of all patterns found in real images share a certain property, namely, that they are 'uniform'. Here, uniformity means that a circular pattern has at most 2 transitions from black to white and vica versa. For example, the pattern 00000001 (2 transitions, considering a cyclic extension where the last bit is also compared to the first) is uniform while the pattern 11001001 (4 transitions) is non-uniform. Interestingly, the most frequent uniform patterns turn out to represent important microfeatures in the image such as dots or edges. Out of the 36 rotationally invariant patterns only 9 are uniform. These patterns are shown in Fig. 4.7. The first and last pattern capture bright spots and black spots or homogeneous surfaces, respectively. The other seven patterns capture edges between a bright and a dark surface. Finally, in our adaptation of the uniform rotation invariant LBP (URILBP) we construct a histogram by counting the number of occurrences in these categories. As such, our VCG-based URILBP feature has a length of 9.

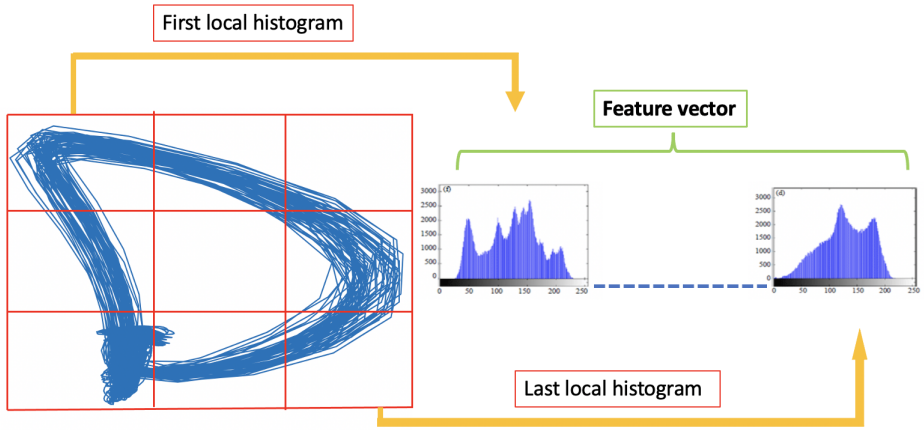

Figure 4.8: The URILBP feature vector of an image consists of a concatenation of the histogram of URILBP scores of each sub-image

The original 3D VCG image is a large binary volume. Before applying URILBP, we first discretize and segment this volume in such a way that the resulting set of grayscale images individually capture meaningful parts of the VCG. We first discretize the 3D image into 2D planes along the x, y, and z-direction with a resolution of 100 pixels per unit of normalized ECG voltage. As a result, binary images (2D planes) are created along all three directions. Next, the binary images are divided into 5 batches in each direction. The images in the batches are summed together, resulting in 5 2D grayscale images in each direction, i.e. 15 planes in total. We emphasize that the major motivation behind this preprocessing is to segment the 3D VCG into P loops, QRS loops and T loops. In Fig. 4.10, 5 planes in x-direction are shown. Plane 3 and plane 4 mainly contain the P loops and T loops, respectively, while QRS loops can be

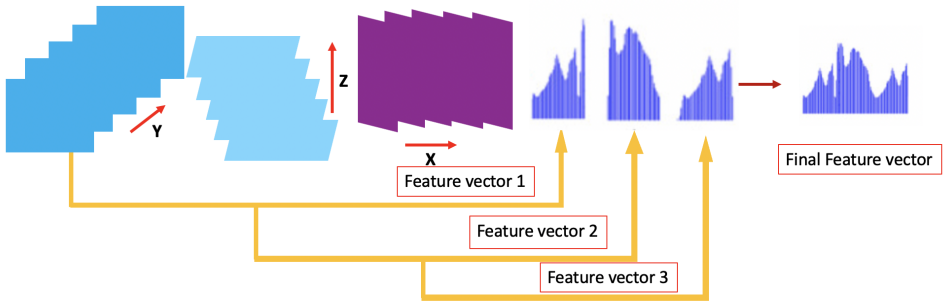

Figure 4.9: 3DLBP feature vector .

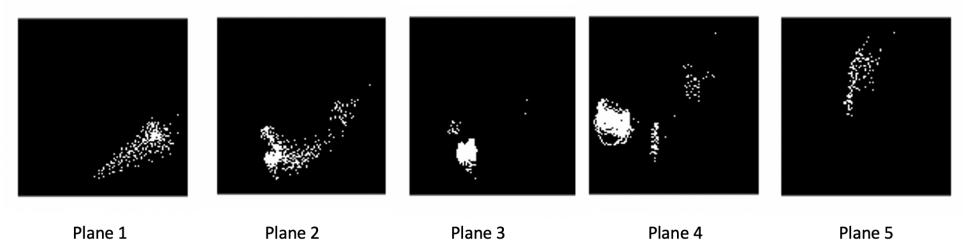

Figure 4.10: Projected planes at x-direction .

detected in plane 1, plane 2 and planes 5. As the P and T loops occupy just part of the plane, the planes are further divided into 9 non-overlapping sub-images and the URILBP histogram is calculated for each sub-image. When the loops follow the same or similar trajectory across subsequent heartbeats, the subimages (in the direction perpendicular to the local trajectory) will contain a majority of black pixels with bright areas (see for example bottom left of plane 3). The edges of such areas may be captured by bins 4-8 in the URILBP histogram. Conversely, chaotic trajectories will result in numerous discrete bright dots (see for example bottom right of plane 1), that can be captured by bins 2-3 of the URILBP histogram.

The nine histograms extracted from the sub-images are concatenated to create a feature vector for that plane (see Fig. 4.8). Finally, the feature vectors of the 15 planes are concatenated into one final feature vector (see Fig. 4.9). We refer to the resulting procedure as 3DLBP.

To compare the 3DLBP between *de novo* AF and persistent AF, we divide the filtered ECG signals into frames of 60 beats. We select the frame with the highest degree of irregularity, as measured by the δ parameter (see Eq. (4.5)). This frame is selected for the following reasons. First, the highest δ frame is representative of the most irregular parts of the signal, so by using 3DLBP on this frame, we can extract the texture information of the VCG trajectory in the most irregular segment

of the signal. Therefore, this enables us to compare the VCG trajectory in the AF episodes in *de novo* AF and persistent AF. Moreover, this will suppress the repetitive information of SR episodes in *de novo* patients and AF episodes with the same trajectory in the VCG. In other words, this enables us to compare a small portion of the signals that is the most characteristic of the ECG in AF patients.

4.2.5. FREQUENCY-BASED FEATURES

The time domain and the spatial domain information are extracted in Section 4.2.3 and Section 4.2.4. As a third feature class, we propose to use specific frequency components of *de novo* POAF and persistent AF. During AF episodes, multiple wavefronts propagate simultaneously through the atrium. As a result, a surface ECG will show a broader frequency spectrum. Indeed, in SR episodes the frequency range of atrial activity is typically between 0.6 Hz and 1.5 Hz, while during an AF episode the atrial activity is typically in the frequency range between 4 and 9 Hz [116, 117]. We hypothesize that features which are related to the frequency components of atrial activity might also provide a distinction between *de novo* POAF and persistent AF.

To analyze the frequency content in the range $4-9$ Hz, we follow the approach presented in [118]. Namely, we use a stationary wavelet transfrom with a Daubechies-5 mother wavelet to obtain the power spectrum $S_l^D(f)$ of the detail coefficients d_l at the lth level. In order to cover the desired frequency range, we first upsample the signal to 500Hz and then use $l=6$ levels of decomposition. The stationary wavelet transform has been used as a bandpass filter to extract the frequency range 4-9 Hz and then a Fourier transform is applied on the detail coefficients d_l at $l=6$ to obtain the $S_l^D(f)$.

Then, we propose to find the dominant frequency (DF), which carries the fundamental frequency of the signal and can be calculated by finding the maximum peak in the power spectrum. In addition, the area under the power spectrum curve can be captured by the average power in the bandwidth of interest [118]. Therefore, we define the DF-to-average-power ratio, for the lth level, as

$$\rho = \frac{\arg\max_{f\in F} S_l^D(f)}{\int_{f\in F} S_l^D(f)\,df}. \tag{4.8}$$

To compare the DF-to-average-power ratio between *de novo* POAF and persistent AF, we divide the filtered ECG signals into 60 s segments and calculate the δ parameter according to Eq. (4.5). Then, we select the frame with highest δ (this indicates the most irregular and thus the most AF containing segment), because we want to compare the AF episodes in *de novo* POAF and persistent AF, while avoiding SR episodes. This will increase the robustness of the classifier since frequency information in the AF episodes are only compared among each other. Since leads V_1, aVF and III have the largest atrial contribution in the ECG signal [119], we determine this feature from these three leads. To compare the DF and DF-to-average-power ratio in *de novo* POAF and persistent AF, we divide the filtered ECG signals into 60 s segments and select the segments with the highest δ index. Then, we sub-divide each segment into 5 s non-overlapping frames. The

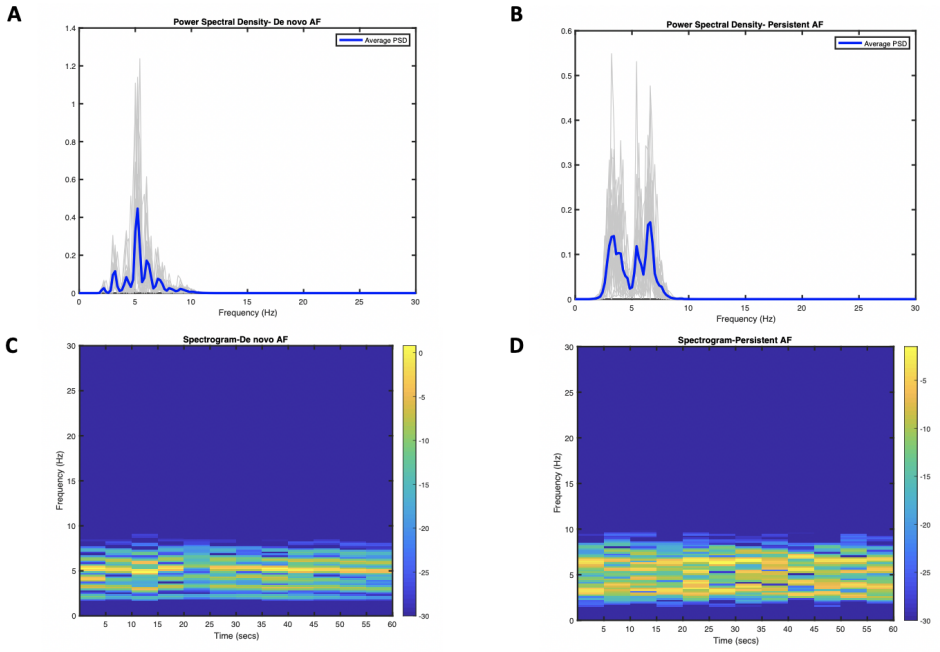

Figure 4.11: Power spectral density and spectrogram, A) PSD of 60 s in a *de novo* POAF (gray) and the average PSD (blue), B) PSD of 60 s in a persistent AF (gray) and the average PSD (blue), C) spectrogram in a *de novo* POAF, D) spectrogram in a persistent AF.

estimated power spectral densities (PSDs) for all consecutive time frame of the detail coefficient in $l = 6$ are plotted on top of each other in gray for a *de novo* POAF patient and a persistent patient in Fig. 4.11.A and Fig. 4.11.B, respectively. The average PSD over time is shown in blue. Persistent AF has a larger DF with wider power distribution, while *de novo* POAF achieves a lower DF with narrower power distribution. Frequency components of atrial activity (AA) in persistent AF vary more than in *de novo* POAF. In the power spectrum for persistent AF, the peak is therefore lower and the width larger. In persistent AF, more frequency components with a lower signal amplitude are thus involved. Moreover, the frame-to-frame variation of the maximum peak of the PSD in *de novo* POAF is smaller than for persistent AF. This can be explained by the hypothesis that during persistent AF, more inconsistent wavelets travel across the atrium which is represented on the surface ECG by the multiple frequency components with most likely slightly different frequencies. Looking at the spectrograms (Fig. 4.11. C and Fig. 4.11. D), DF in *de novo* POAF is more consistent across time frames than persistent AF. It shows that by considering the whole sequence of spectra across 60 s, there are more variations in the activated frequency components in persistent AF.

4.2.6. FEATURE SELECTION

When the number of features in a classification task is too large or/and features are correlated, feature selection is a critical pre-processing step for selecting the features with the highest relevance. This not only might reduce the computational burden of training the classifier but in many instances boosts its performance. In this work, we use ReliefF as our feature selection method [43]. ReliefF is a filter-based feature selection method which finds weights for the features. In the ReliefF algorithm, a feature from a random training sample is selected as R_i and then the algorithm searches for its two nearest neighbors as nearest hit H_j (from the same class) and nearest miss M_j (from the different class)[1] [43]. The importance of a feature is represented by a weight. The weight increases if the feature and miss have different values while it decreases if the feature and hit have different values. This algorithm is repeated m times where m is a user-selected parameter. The highest weighted features are selected to train the classifier.

4.2.7. CLASSIFICATION

The performance of the extracted features is evaluated by implementing two supervised methods. In the next sections, we explain these methods used to classify patients into *de novo* POAF or persistent AF.

Support vector machine With Support Vector Machines (SVMs), a decision boundary with a maximum margin is found for separating data points of different classes. Although an SVM is originally a linear classifier, the use of kernel functions enables SVM to perform nonlinear classification. Given a training set of P points as $p_i : i = 1, 2, ..., P$ with defined labels q_i, either -1 or $+1$, SVM classifies a test data p as [116]

$$f(p) = sgn\left(\sum_{i=1}^{P} \beta_i q_i K\left(p_i, p\right) + o\right) \tag{4.9}$$

where sgn is the sign function, β_i are Lagrange multipliers, K is the kernel function and o is the bias of the hyperplanes. In this work, we use the radial basis function (RBF) kernel function where we fixed the kernel parameter $\sigma = 1$. We empirically found that for our dataset this value represented a good trade-off between flexibility, i.e, higher testing accuracy, and the risk of overfitting.

Random forest Random Forest (RF) is an ensemble learning method which is used for classification or regression problems. RF combines multiple decision trees for the final result in which each decision tree consists of three types of nodes, namely, the root node, inner nodes, and leaf nodes. Each decision predicts a result and the final result is produced by the majority voting among all trees. The advantage of using RF in our problem is that it solves the overfitting problem and the problem of unbalanced datasets, and normalization of features is not necessary [120]. We

[1] The ReliefF algorithm searches for the k nearest hits and misses selected randomly from the dataset and averages between them to compute the importance.

trained a bagged ensemble of 150 classification trees with the maximum number of splits set to 13, using the highest weighted features.

4.3. RESULTS

4.3.1. FEATURE ANALYSIS

The performance of the extracted features is demonstrated in this section. As in most *de novo* POAF patients AF develops after 48h (day three), we extracted features starting from the third day (48h-72h) to observe AF episodes in patients. Considering the three groups of features (i.e., rhythm-, VCG- and frequency-based features) and after selecting the most irregular segments, we have used 121979 seconds, in total. More specifically, we used 84883 seconds from *de novo* POAF patients and 37096 seconds from persistent AF patients. In the rhythm-based features, 1000 RR intervals have been used per patient which vary between 372s and 938s. For the VCG-based features, we used 60 beats per patient which vary between 24s and 57s. In the frequency-based features, we used 60s per patient. Four features, namely, $\bar{I}$, σ_a, σ_d, ϱ are extracted from the rhythm-based feature, in total. From the frequency-based features, ρ is calculated for the leads V_1, aVF, and III (three features). For the VCG-based features, using URILBP for the most irregular (highest δ) frame of the 3D VCG, results in a feature vector with length 1215. Therefore, the initial length of the feature vector, for each patient, is 1222. Negative weights estimated by ReliefF are not suitable predictors for the classifier [43], so by using ReliefF, we then selected the 32 highest weighted features (positive ones) for training the classifier, which turned out to be all rhythm-based features ($\bar{I}$, σ_a, σ_d, and ϱ), ρ from lead V_1, and some bins of the URILBP histogram.

Fig. 7.2 shows the box plots of some of the selected features. In Fig. 7.2.A and Fig. 7.2.B three rhythm-based features (σ_a, σ_d and $\bar{I}$) and two ratios (ϱ and ρ) are shown, respectively. Four selected bins of the VCG-based features are shown in Fig. 7.2.C. Looking at Fig. 7.2.A, in the *denovo* POAF patients, the σ_a, σ_d and $\bar{I}$ are larger than for persistent AF. Comparing ϱ and ρ (Fig. 7.2.B) in *de novo* POAF and persistent AF, ϱ in *de novo* POAF is larger than for persistent AF which shows that the rank 1 model is appropriate for *de novo* POAF. Also, ρ is larger in *de novo* POAF than in persistent AF, as there are more frequency components in persistent AF than in *de novo* POAF. For the VCG-based features, 27 bins are selected by the ReliefF algorithm. Here, we have interpreted a few of these bins (four patterns which are shown in Fig. 7.2.C) for the following reasons. At first, some of the VCG bins are discriminative independently and the rest are jointly insightful. In this section, we focus on the independent bins. Second, VCG-based features are extracted from three directions (X-Y planes, X-Z planes and Y-Z planes). So, examples from all three directions are shown. Third, these bins have the highest weights in the ReliefF algorithm. Therefore, we have interpreted the most discriminative bins. The selected features are mainly concentrated on the sub-images that correspond to the P loops area. In Fig. 7.2.C, patterns 5 and 6 belong to the P loops area on the X-Y plane. The patterns represent the edges in the image. The edges are indicators for a particular pattern in an image. These patterns can show the difference between a loop and a

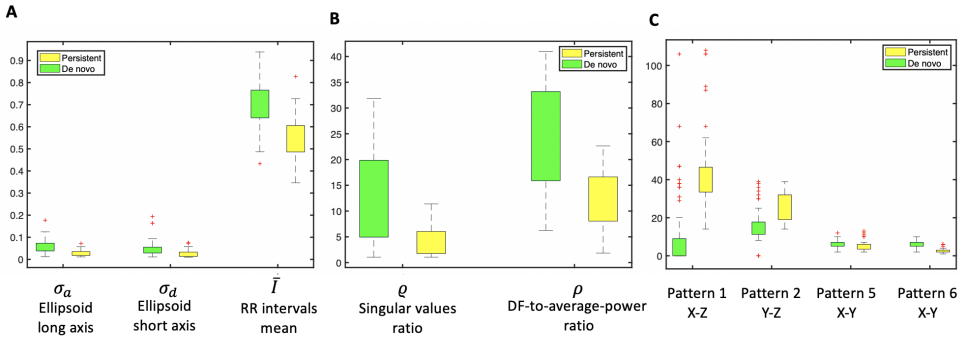

Figure 4.12: Box plots of the selected features, A) Rhythm-based features (σ_a: ellipsoid long axis, σ_d: ellipsoid short axis and $\bar{I}$: RR intervals mean), B) Ratios (ϱ: singular values ratio Eq. (4.6), ρ: DF-to-average-power ratio Eq. (4.8)), C) VCG-based features .

chaotic pattern. In the *de novo* patients, the number of pixels that represent patterns 5 and 6 is larger than in persistent AF patients. It shows that there are more edges for *de novo* patients than for persistent AF. Conversely, patterns 1 and 2 represent single dot and double dots in the 3×3 neighborhood, respectively. In Fig. 7.2.C, pattern 1 is a bin on the P loops area on the X-Z plane and pattern 2 is on the Y-Z plane. In persistent AF, the number of pixels that represent patterns 1 and 2 is larger than in *de novo* POAF patients. The more chaotic the pattern, the more dots there are on the LBP image. In other words, these box plots represent that in the bins that correspond to edges (i.e. regular loops), the number of pixels in the *de novo* POAF is higher than in persistent AF, while in bins that correspond to dots (i.e. chaotic patterns), the number of pixels in persistent AF is higher than in *de novo* POAF.

For the validation of the classifier, we report the mean (M) and standard deviation (SD) of 5-fold cross validation on 151 patients (99 *de novo* POAF patients and 52 persistent AF patients). To keep the same proportion for each group in the training set as in whole dataset, we applied 5-fold splitting on each class separately. In 5-fold cross validation testing, we have under-sampled the majority class (i.e., *de novo* POAF) to have the same number of patients to evaluate in both classes [121].

4.3.2. PERFORMANCE EVALUATION PARAMETERS

To check the performance of the classifier, we evaluate our results using common performance metrics such as accuracy (ACC), sensitivity (SEN), specificity (SPE), precision (PRE), and F_1 score. These metrics are defined as

$$ACC = \frac{TP + TN}{TP + TN + FP + FN} \times 100 \tag{4.10}$$

$$SEN = \frac{TP}{TP + FN} \times 100 \tag{4.11}$$

$$SPE = \frac{TN}{TN + FP} \times 100 \tag{4.12}$$

$$PRE = \frac{TP}{TP+FP} \times 100 \tag{4.13}$$

$$F_1 = 2\frac{PRE \times SEN}{PRE+SEN} = \frac{2TP}{2TP+FP+FN} \times 100, \tag{4.14}$$

where TP and TN are the numbers of correctly detected and rejected cases in class one, respectively, and FP and FN are the numbers of wrongly detected and rejected cases in class one, respectively. We report the classification results for the random forest and SVM classifiers with kernel function RBF with scaling factor 1. Considering TP as the number of correctly detected cases of persistent AF, in Table 4.1 and Table 4.3, the performance of the SVM and RF classifier are shown, respectively. Considering TP as the number of correctly detected *de novo* POAF cases, in Table 4.2 and Table 4.4, the performance of the SVM and RF classifier are shown, respectively. To investigate the importance of each group of features, we trained the classifiers with each group of features separately (group 1: rhythm-based features, group 2: VCG-based features, group 3: frequency-based features). Then, we merged the groups with a combination of two out of three groups and finally, all three groups were used for training the classifiers. Looking at Table 4.1 and Table 4.2, it is clear that all three groups and both classifiers are able to differentiate *de novo* POAF patients from persistent AF patients. The rhythm-based features and the combination of rhythm- and frequency-based features have the highest accuracy in the classification using one group and two groups, respectively. Moreover, the random forest has the highest accuracy and F_1 score. The classifier achieving the highest accuracy is the random forest classifier using all three groups of features, reaching an accuracy of over 89%.

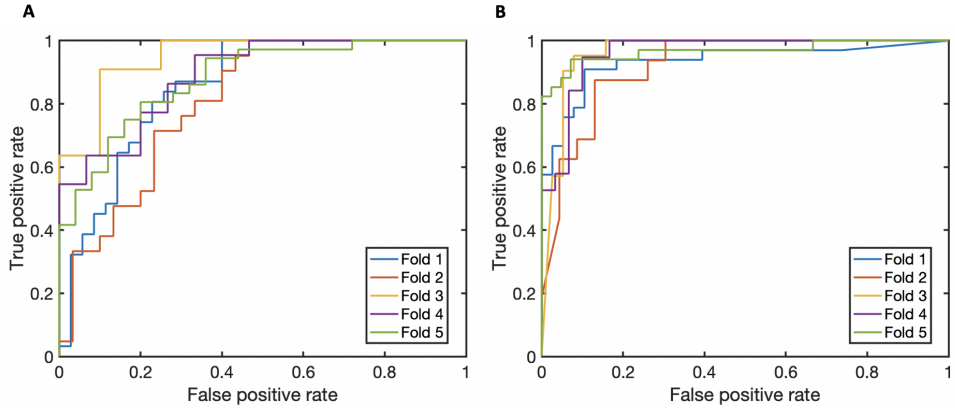

Figure 4.13: Receiver operating characteristic (ROC) curve on the testing dataset, A) SVM, B) RF.

Looking at Tables 4.1 - 4.4, and Fig. 4.13, RF performs better than SVM. The performance of the SVMs depends on the kernel function. Although the RBF kernel is known to be a universal approximator [122], finding the optimal kernel parameters given our relatively limited dataset is a challenging problem. Note that in the

current chapter, our main goal was to demonstrate that classification is possible. Optimizing classification performance is out of the scope, however, we believe that SVM classification could be further improved by resolving the issues mentioned above.

Table 4.1: The performance of the SVM classifier on the selected features, Group 1: Rhythm-based features, Group 2: VCG-based features, Group 3: Frequency-based features
TP: Persistent AF.

Features	Metric	Acc	Sen	Spe	Pre	F_1
Group 1	**M**	71.84	75.89	67.48	71.77	73.33
	SD	3.28	8.13	10.01	6.55	3.73
Group 2	**M**	67.63	68.93	64.59	65.91	66.09
	SD	6.16	9.31	6.57	5.64	7.32
Group 3	**M**	68.91	71.25	66.12	67.82	68.89
	SD	4.38	4.12	9.32	8.01	7.56
Groups 1 & 2	**M**	72.91	74.77	71.40	70.50	72.14
	SD	4.61	8.14	7.08	6.17	3.22
Groups 1 & 3	**M**	74.14	64.04	82.90	76.33	66.28
	SD	5.45	6.23	6.92	5.46	5.62
Groups 2 & 3	**M**	72.99	73.98	71.51	70.76	71.94
	SD	5.68	7.20	7.26	7.16	5.79
All groups	**M**	79.00	81.38	75.96	78.30	79.69
	SD	5.65	4.82	8.95	7.44	7.12

4.4. DISCUSSION

This section discusses and interprets our results and compares them with related works. For this purpose, in Section 4.4.1, we compare the developed features with similar studies in the literature. Then, in Section 4.4.2, we elaborate on one group of the developed features (frequency-based features) and compare them with the high-resolution electrogram mapping, motivating multimodal analysis. Finally, in Section 4.4.3, we pinpoint some of the limitations and potential improvements to consider for the future.

4.4.1. RELATION TO LITERATURE

In general, detecting AF and doing the follow-up gives insights into the gradual progress of the pathological damage in the tissue. In the past, many studies have been done to find discriminators between AF and SR. However, the stages of AF are often not included in these studies and the discrimination is based on the presence of an AF episode or an SR episode. Self-terminating and sustained AF have been studied in recent works. Most of these studies focused on the dominant frequency of the AA, heart rate variability, sample entropy phase variations and fractal dimension

Table 4.2: The performance of the SVM classifier on the selected features, Group 1: Rhythm-based features, Group 2: VCG-based features, Group 3: Frequency-based features
TP: *De novo* POAF.

Features	Metric	Acc	Sen	Spe	Pre	F_1
Group 1	**M**	71.84	67.48	75.89	72.05	69.14
	SD	3.28	10.01	8.13	9.18	6.86
Group 2	**M**	67.63	64.59	68.93	69.77	65.95
	SD	6.16	6.57	9.31	6.17	7.81
Group 3	**M**	68.91	66.12	71.25	69.81	66.96
	SD	4.38	9.32	4.12	5.49	6.42
Groups 1 & 2	**M**	72.91	71.40	74.77	74.89	72.62
	SD	4.61	7.08	8.14	5.67	7.69
Groups 1 & 3	**M**	74.14	82.90	64.04	75.33	77.41
	SD	5.45	6.92	6.23	6.21	6.75
Groups 2 & 3	**M**	72.99	71.51	73.98	74.22	72.34
	SD	5.68	7.26	7.20	6.62	7.25
All groups	**M**	79.00	75.96	81.38	79.18	77.40
	SD	5.65	8.95	4.82	4.68	6.30

Table 4.3: The performance of the RF classifier on the selected features, Group 1: Rhythm-based features, Group 2: VCG-based features, Group 3: Frequency-based features
TP: Persistent AF.

Features	Metric	Acc	Sen	Spe	Pre	F_1
Group 1	**M**	80.93	78.73	83.12	83.46	80.37
	SD	6.71	5.09	10.78	6.22	6.70
Group 2	**M**	77.01	70.21	82.58	80.95	72.66
	SD	5.05	6.18	4.98	5.22	5.79
Group 3	**M**	79.17	82.46	75.78	76.62	79.08
	SD	4.22	4.97	4.78	4.29	6.46
Groups 1 & 2	**M**	83.42	84.89	82.73	78.93	81.61
	SD	4.00	4.66	5.21	5.3	4.95
Groups 1 & 3	**M**	86.38	89.40	83.78	82.20	85.27
	SD	3.82	3.7	6.58	3.95	3.16
Groups 2 & 3	**M**	82.27	85.88	79.08	79.84	82.50
	SD	4.59	5.17	6.81	6.46	2.94
All groups	**M**	89.07	92.57	86.23	83.95	87.93
	SD	2.77	3.63	6.24	6.00	2.81

[8, 9, 123–125]. However, they do not address the classification of *de novo* POAF and persistent AF. For instance, [8, 9] compared self-terminating AF versus sustained AF, and e.g., [10] aimed to differentiate paroxysmal versus persistent AF. Notice that despite the fact that our problem overlaps with these classification tasks, it is not

Table 4.4: The performance of the RF classifier on the selected features, Group 1: Rhythm-based features, Group 2: VCG-based features, Group 3: Frequency-based features
TP: *De novo* POAF.

Features	Metric	Acc	Sen	Spe	Pre	F_1
Group 1	**M**	80.93	83.12	78.73	78.11	80.10
	SD	6.71	10.78	5.09	6.91	5.88
Group 2	**M**	77.01	82.58	70.21	75.91	77.55
	SD	5.05	4.98	6.18	6.12	5.91
Group 3	**M**	79.17	75.78	82.46	81.17	78.10
	SD	4.22	4.78	4.97	5.35	6.47
Groups 1 & 2	**M**	83.42	82.73	84.89	88.63	87.02
	SD	4.00	5.21	4.66	4.23	4.02
Groups 1 & 3	**M**	86.38	83.78	89.40	90.64	86.72
	SD	3.82	6.58	3.7	4.71	5.26
Groups 2 & 3	**M**	82.27	79.08	85.88	83.31	80.93
	SD	4.59	6.81	5.17	4.9	5
All groups	**M**	89.07	86.23	92.57	90.96	89.76
	SD	2.77	6.24	3.63	3.12	2.76

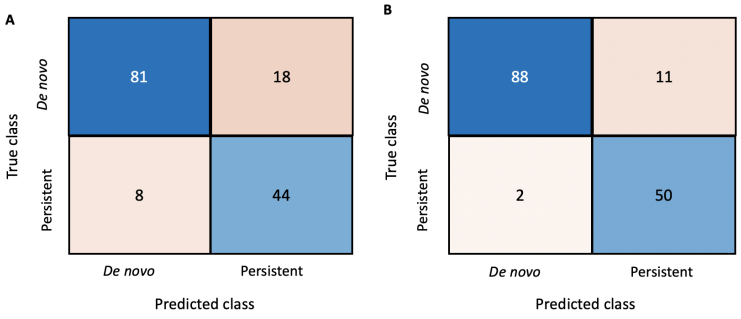

Figure 4.14: Confusion matrix of the training dataset (the whole dataset), A) SVM, B) RF.

completely included in any of them. In addition, some of these works only compared AF episodes in short-length signals, e.g., [99], so the global features introduced in the current work cannot be directly compared with these.
In this work we considered both morphological (VCG-based and frequency-based features) and rhythmic (rhythm-based features) changes by extracting features from AF episodes. However, the performance of the rhythm-based and VCG-based features depends on the detection of the R peaks. We deal with this problem by extracting frequency-based features which are independent from the detection of R peaks. Therefore, it makes the algorithm more robust in case of missed-R peak detection. Related to the frequency-based features, Petrutiu et al. [123] calculated the dominant frequency of ECG signals by using template matching QRS-T cancellation and showed differences for paroxysmal and persistent AF. The dominant frequency

in paroxysmal AF obtained was 5.2 ± 0.4 Hz while for persistent AF was 6.6 ± 0.6 Hz. Similarly, Chiarugi et al. [9] used the dominant frequency and average heart rate to discriminate between non-terminating and terminating AF episodes on 1-minute ECG signals. These studies demonstrate the ability of the dominant frequency for differentiating paroxysmal/persistent AF or terminating / non-terminating AF. In the current study, we considered normalizing with the average power to take all involved frequency components into account.

4.4.2. COMPARISON WITH INVASIVE WAVE MAPPING

Regardless of their discriminating capabilities, the dominant frequency and average power reveal pathological characteristics of both *de novo* POAF and persistent AF. That is, from a physiological point of view, the level of atrial fibrosis in paroxysmal AF patients is lower than that in persistent AF patients. So, paroxysmal AF patients tend to present a lower dominant frequency in comparison with persistent AF [99]. This observation is confirmed by our results.

Using electrogram data, Allessie et al. [126] studied the wave maps and dissociation maps for the acute AF and longstanding AF obtained from the intra-operative mapping on the right atrium. It is noted that the number of waves entering the area of the mapping in acute AF is less than that in longstanding AF. The number of waves is also related to the boundaries of the conduction blocks and collisions. To compare our frequency-based features with the observation of wave mapping, we investigate the distribution of frequency-based features over time. To do this, we divide the pre-processed signals into 60 s segments and calculate the index δ according to Eq. (4.5). Then, for AF episodes, we sort segments according to the δ from the highest to the lowest and select 20 segments with the highest δ. These are thus the most irregular segments. Then, we sub-divide each segment into 5 s non-overlapping frames and calculate the DF and ρ in each frame. Fig. 4.15 shows

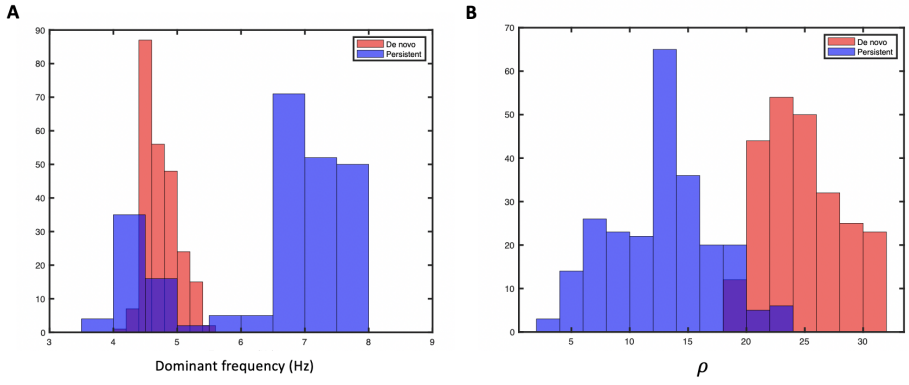

Figure 4.15: Histogram of the frequency-based features for 20 segments with the highest δ, A) DF B) ρ.

the histogram of the frequency-based features for 20 segments with the highest δ in a *de novo* POAF patient and a persistent AF patient.

Comparing DF in a *de novo* POAF patient (Fig. 4.15.A, red plot) and a persistent AF patient (Fig. 4.15.A, purple plot), frame-to-frame variation of DF in *de novo* POAF is smaller than for persistent AF. It shows that by considering the whole spectrum, there are more frequency components in persistent AF that are activated. Looking at ρ in Fig. 4.15.B, in the *de novo* POAF patient, the ρ is more concentrated than in persistent AF, which means that there is no direct relationship between DF and ρ in the persistent AF. Moreover, looking at ρ, there is less overlap between the *de novo* POAF and persistent AF compared to the DF, which shows that ρ could be a valuable discriminator for this classification. Therefore, combining these observations with wave mapping results, we hypothesize that there exists a relationship between the number of waves in the intra-operative mapping with the dominant frequency and power spectrum of the wavelet detail coefficients of the ECG signal. To test this hypothesis, future work could consider instances where the electrogram and ECG signals are recorded simultaneously. The ρ could be calculated from leads aVF and III of the ECG (since V_1 is not available during an open-heart surgery) and the frequency-based features could be compared with the wave maps obtained from the electrograms.

4.4.3. LIMITATIONS AND FUTURE WORK

Although the proposed method reached an accuracy of over 89% for differentiating between *de novo* POAF and persistent AF, it has some limitations. First, we cannot really compare our work to other features/classification schemes as this is the first study on *de novo* POAF and persistent AF as far as we know. Moreover, the lack of telemetry data in the persistent AF cases limited our evaluation to a small group of patients. Results shown in the tables in Section 4.3 are based on a 5-fold cross-validation within our dataset of 151 patients. In order to investigate the robustness of our approach, future work will aim to validate the algorithm on an independent (preferably prospective and multi-center) dataset. Furthermore, body mass index (BMI) is an important factor in the amplitude of the recorded ECG signals, as well as for VCG signals. To be able to compare the surface of the QRS loops in *de novo* POAF and persistent AF effectively, BMI should also be considered. Finally, we focused on a specific frequency range in the frequency-based features to measure the dominant frequency of AA, however, in such a frequency range, the effects of ventricular activity (VA) are not completely removed. To improve the frequency-based features, QRS-T cancellation or AA extraction by source separation methods might lead to further improvement.

Furthermore, as predicting AF is necessary for increasing the success of treatments, it would also be useful to concentrate on identifying features from the SR episodes of the signal to predict AF. As *de novo* POAF is the most common complication after surgery, telemetry data from a large population of *de novo* POAF can be collected. Therefore, deep learning techniques could then be viable to identify features from the SR episodes in a data-driven manner when combined with expert knowledge of the underlying physiological principles.

4.5. CONCLUSION

In this chapter, we proposed a feature engineering machine learning-based classification approach for the detection of short- and long-term AF based on the extracted features from the multi-channel ECG signals. We introduced three groups of features (rhythm-, VCG- and frequency-based features) to cover both morphological and rhythmic changes from AF episodes. The performance of our method is evaluated by implementing RF and SVM classifiers in which RF could achieve 89.07% accuracy. Furthermore, the introduced features unveil the irregularity differences of the RR intervals and the morphological differences of the fibrillatory waves between *de novo* POAF and persistent AF patients. As the severity of AF increases, these features could be considered indicators for the correct stage of the patient. For example, the increase in the severity level of an AF patient leads to an increase in the irregularity of RR intervals, resulting in a higher value of ϱ. Furthermore, an increase in the chaotic pattern in the VCG results in a higher number of pattern 1 in Fig. 4.7. Finally, an increase in the number of frequency components results in a higher value for the DF-to-average-power ratio.

In this chapter, we have seen that the progression of atrial fibrillation can be monitored by capturing morphological and rhythmic differences. In the next chapter, we focus on integrating ECG findings with high-resolution electrogram mapping, aiming to improve AF diagnosis.

5

A SINGULAR-VALUE-BASED MARKER FOR THE DETECTION OF ATRIAL FIBRILLATION

In the previous chapter, we developed a method to detect the progression of AF using multi-lead ECG. In this chapter, we focus on more detailed measurement data acquired directly at the surface of the heart, called a high-resolution intra-operative epicardial electrogram. This will increase the accuracy of AF detection and enable to locate electropathological regions.

The severity of atrial fibrillation (AF) can be assessed from intra-operative epicardial measurements (high-resolution electrograms) using metrics such as conduction block (CB) and continuous conduction delay and block (cCDCB). These features capture differences in conduction velocity and wavefront propagation, but ignore complementary properties such as the morphology of the action potentials. In this chapter, we focus on the morphology of the action potentials, and derive features to detect variations in the atrial potential waveforms. We show that the spatial variation of atrial potential morphology during a single beat may be described by changes in the singular values of the epicardial measurement matrix. The method is non-parametric and requires little preprocessing. A corresponding singular value map points at areas subject to fractionation and block. Further, we developed an experiment where we simultaneously measure electrograms (EGMs) and a multi-lead ECG. The captured data showed that the normalized singular values of the heartbeats during AF are higher than during SR, and that this difference is more pronounced for the (non-invasive) ECG data than for the EGM data, if the electrodes are positioned at favorable locations. Overall, the singular value-based features are a useful indicator to detect and evaluate AF. The proposed method might be beneficial for identifying electropathological regions in the tissue without estimating the local activation time.

This chapter is based on a paper submitted as "H. Moghaddasi, R. C. Hendriks, B. Hunyadi, M. van Schie, P. Knop, N. M. S. de Groot, and A. J. van der Veen, *A Singular-value-based Marker for the Detection of Atrial Fibrillation Using High-resolution Electrograms and Multi-lead ECG*"

5.1. INTRODUCTION

In Chapters 3 and 4, we have analyzed the multi-lead ECG for severity detection of atrial fibrillation. In this chapter, we also consider measurements at the surface of the heart and propose a diagnostic tool to detect atrial fibrillation using ECGs and high-resolution electrograms.

High-resolution electrograms (EGMs) are used to understand the electropathological process of AF in more detail. From such measurements, the electrical propagation in the heart and the conduction velocity are assessed by the local activation time (LAT) and derived features, such as conduction block (CB) and continuous conduction delay and block (cCDCB). This analysis is influenced by the accuracy of the LAT estimation. Furthermore, these features assessed during sinus rhythm do not sufficiently differentiate between the various stages of AF development [12, 13].

In some cases, the electropathology of atrial tissue can also be linked to the morphology of the observed signals. The R/S ratio of single potentials (SPs) has been shown to be useful for assessing the severity of conduction inhomogeneity [14, 15]. This is complementary to the LAT analysis: a wavefront[1] could propagate normally, even while the underlying APs are abnormal. In our previous work (reported in Chapter 7, we have demonstrated that the development stages of AF might manifest themselves as variations in atrial potential waveforms [127].

In this chapter, we go one step deeper and study a measurement data matrix formed from an array of unipolar EGMs. This matrix is preprocessed such that it becomes insensitive to differences in LAT but remains sensitive to spatial differences in AP morphology. We then look at the singular values of this matrix. A simple cardiac signal model demonstrates that if all cells beneath the electrodes generate the same action potential (AP), and the propagation follows a flat wavefront, then the data matrix has rank 1: only a single singular value is nonzero. Furthermore, with a slightly more elaborate signal model, we will demonstrate that, in case of more complex underlying physiology - such as differences in AP morphology or abnormal wavefront propagation - the data matrix has a higher rank, which can be detected by an increase in the second singular value.

Thus, our hypothesis is that the normalized second singular value is a useful feature to detect and classify degrees of AF. This is tested on two types of clinical data. First, we study this feature on measured intraoperative unipolar EGMs obtained from patients with induced AF. Comparing SR and AF data, we found that the normalized singular values are significantly higher during AF than during SR, and this allows to discriminate between SR and AF.

Next, we also study singular values for data collected using a (non-invasive) multi-lead ECG. In particular, we have designed a sub-vest to monitor the body surface potentials (BSPs) at 15 leads simultaneously combined with EGM mapping at specific epicardial locations during minimally invasive surgery. This vest was designed as a standard 12-lead ECG cannot be simultaneously acquired during open-heart surgery. The acquired data allows to study the singular values of the low-resolution BSP data for exactly the same heartbeats as the high-resolution EGMs. The results show that, for specific placements of the electrodes, the BSP shows even

[1] To compare the various wavefronts visually, see Fig. 5.2

more significant changes in singular values than the EGM, presumably because the latter only measures a small area of the atrial surface.

For EGM data acquired on a sufficiently large rectangular grid, the normalized second singular value can also be computed from overlapping submatrices of 3×3. Looking at the submatrices helps us to locate the abnormal electropathological regions in the tissue. This allows to construct a novel map that has complementary information to the traditional activation map. The results show that this map highlights areas of double potentials, simultaneous presence of multiple AP morphologies, and block. These are often associated with AF. We propose this map as a useful tool, complementary to the use of activation maps.

A related eigenvalue analysis (and corresponding map) was proposed by Riccio e.a. [128]. As a preprocessing step, their method requires to time-align the time-domain electrogram traces. The estimation of the local activation times is an additional step, which also based on an underlying model where for each trace a single activation time can be estimated. This is problematic at electrodes that see a double potential. In contrast, our proposed method requires only little preprocessing.

The rest of this chapter is structured as follows. In Section 5.2, we introduce our method, including notation, action potential, and electrogram model, and analyze the singular values in relation to various scenarios, such as one or more signal morphologies, and one or more wavefronts. In Section 5.3 we demonstrate the proposed approach on simulated data. Then, in Chapter 6, we will test the approach on clinical data.

5.2. METHODOLOGY

5.2.1. NOTATION

In this chapter, scalars are denoted by normal lowercase letters, vectors by bold lowercase letters, and matrices by bold uppercase letters. For matrices, $(|\cdot|)$ is the element-wise absolute value, and $(.^H)$ denotes the Hermitian operator.

5.2.2. ACTION POTENTIAL AND ELECTROGRAM MODEL

An action potential is generated by a sequence of voltage changes across the membrane of a cell. Various mathematical models have been proposed to describe the AP in atrial myocytes and pacemaker cells. In particular, the total ionic current in human atrial myocytes can be computed from the Courtemanche model (which is explained in Section 2.4.1) [53], while for pacemaker cells, which have funny currents, the ionic current is governed by the Fabbri et al. model [52].[2] Next, a reaction-diffusion equation models the AP propagation in a 2D tissue, described by the interaction of three currents: the transmembrane current, the stimulus current, and the ionic current. In models with uniform parameters, the resulting APs are the

[2] The Courtemanche model was used to produce the simulated data for our analysis. By varying parameters, this model can generate a variety of AP morphologies. More elaborate computer models of electrograms have been developed in [55, 129, 130], and these could be used to improve our analysis.

same for all cells, and a simple data model to describe this is

$$p_c(t) = a_c\, s(t-\tau_c), \quad c = 1, \cdots, C, \tag{5.1}$$

where $p_c(t)$ is the AP (voltage) for the cth cell, a_c is a positive real amplitude, $s(t)$ is the reference AP, and τ_c is the time delay between a reference cell and the cth cell. C denotes the total number of cells in the 2D tissue model. Here, "cell" does not refer to a physical cell, but rather a space-discretized grid point representing a collection of physical cells. The delays τ_c are the LATs. These are related to each other via wavefronts, which follow from the selected diffusion-reaction model, the underlying conductivity tensors, and an initial stimulus scenario [55].

Moving one level up, the electrogram as measured on the epicardium is modeled by a collection of M electrodes assumed to be placed at a constant height above the tissue. We have seen the electrogram model for a 1D tissue in the continuous form in Eq. 2.2. This model can be generalized to a 2D tissue. Basically, each electrode measures a weighted sum of the action potentials $p_c(t)$ from all cells on the 2D tissue. The mth electrode signal (voltage) $d_m(t)$ at location (x_m, y_m) with a constant height z_0 above the 2D tissue can then be modeled as [130] as

$$\begin{aligned} d_m(t) &= \sum_{c=1}^{C} h_{m,c}\, p_c(t), \qquad m = 1, \cdots, M \\ h_{m,c} &= \frac{k_0}{\sqrt{(x_c - x_m)^2 + (y_c - y_m)^2 + z_0^2}}. \end{aligned} \tag{5.2}$$

Here, the weight $h_{m,c}$ describes the instantaneous gain from cell c to electrode m, using an inverse relation to distance, and k_0 is a constant scale parameter (electrode gain). The electrode size in this model formulation is very small and is considered as a point electrode.

5.2.3. DATA STACKING AND PROCESSING

Returning to the cell model (5.1), we first apply a Fourier transform: let

$$\tilde{p}_c(\omega) = \int_{-\infty}^{+\infty} p_c(t) e^{-j\omega t}\, dt \tag{5.3}$$

where $\tilde{(\cdot)}$ denotes the frequency domain. We take N samples in frequency domain:[3] $\omega \in \{\omega_1, \omega_2, \cdots, \omega_N\}$. The $C \times N$ complex samples are stacked into a matrix $\boldsymbol{P}$:

$$\boldsymbol{P} = [\tilde{p}_c(\omega_n)]_{c,n} \in \mathbb{C}^{C \times N}.$$

For electrode signals $d_m(t)$, we can do a similar processing, resulting in a matrix that we denote by $\boldsymbol{D}$, but that now will have size $M \times N$.

As motivated later, we drop the phase by taking the element-wise absolute value of $\boldsymbol{P}$ (action potentials) or $\boldsymbol{D}$ (electrograms) as $\boldsymbol{B} = |\boldsymbol{P}|$ or $\boldsymbol{B} = |\boldsymbol{D}|$, respectively.

[3] In practice, we would sample in time domain and use the FFT.

Finally, we compute the singular value decomposition (SVD) of $\boldsymbol{B}$ as

$$\boldsymbol{B} = \boldsymbol{U}\boldsymbol{\Sigma}\boldsymbol{V}^H, \tag{5.4}$$

where $\boldsymbol{U}$ and $\boldsymbol{V}$ are unitary matrices containing the left and right singular vectors, and $\boldsymbol{\Sigma}$ is a diagonal matrix containing the singular values $\{\sigma_1, \cdots, \sigma_N\}$, sorted in descending order.

The singular values are indicative of the numerical rank of the matrix, and they give important information on the complexity of the matrix. Next, we analyze these singular values for several cases of interest.

5.2.4. SINGULAR VALUE ANALYSIS

Cell level, single AP morphology We start at the cell level and assume, as in (5.1), that under healthy conditions all cells generate APs with the same morphology. In the frequency domain, (5.1) gives

$$\tilde{p}_c(\omega) = a_c\, e^{-j\omega\tau_c}\, \tilde{s}(\omega). \tag{5.5}$$

After discarding the phase by taking the absolute value, and stacking the magnitude spectra into the matrix $\boldsymbol{B}$, we observe that

$$\boldsymbol{B} = \boldsymbol{a}\boldsymbol{s}^T, \tag{5.6}$$

where $\boldsymbol{a} = [a_1, \cdots, a_C]^T$ and $\boldsymbol{s}^T = [|\tilde{s}(\omega_1)|, \cdots, |\tilde{s}(\omega_N)|]$. This model shows that $\boldsymbol{B}$ has rank 1: only one singular value is non-zero. This important property is achieved by discarding the phase (which contains the effect of the LATs), and the assumption that all cells have the same AP morphology. Unfortunately, some information on the morphology is lost, since we also drop the phase of $\tilde{s}(\omega)$.

Since the LATs do not play a role after taking the absolute value, it does not matter whether the AP model describes an SR scenario (τ_c organized in a single wavefront) or an AF scenario (τ_c organized in multiple wavefronts, or highly unstructured).

Cell level, two different AP morphologies As a second case, we consider a scenario where cells take one out of two morphologies, $s_1(t)$ or $s_2(t)$.

The data model for $\boldsymbol{B}$ results in

$$\boldsymbol{B} = \boldsymbol{A}\boldsymbol{S} = \boldsymbol{a}_1\boldsymbol{s}_1^T + \boldsymbol{a}_2\boldsymbol{s}_2^T \tag{5.7}$$

where $\boldsymbol{A} = [\boldsymbol{a}_1\ \boldsymbol{a}_2]$ and $\boldsymbol{S} = [\boldsymbol{s}_1\ \boldsymbol{s}_2]^T$. Entries of $\boldsymbol{a}_1$ are zero if the corresponding cell is of the second type, and likewise, entries of $\boldsymbol{a}_2$ are zero if a cell is of the first type. Thus, the columns of $\boldsymbol{A}$ are complementary and trivially orthogonal. Since by assumption $\boldsymbol{s}_1 \neq \boldsymbol{s}_2$, the matrix $\boldsymbol{B}$ has rank 2, and only two singular values are nonzero.

These two singular values are determined by two parameters:

1. The difference between $\boldsymbol{s}_1$ and $\boldsymbol{s}_2$, as expressed by their cross-correlation. If the difference is small, then the second singular value will be small.

2. The number of cells in group 1 versus the number of cells in group 2: this determines the ratio $\|\boldsymbol{a}_1\|/\|\boldsymbol{a}_2\|$. If the cells are predominantly in one group, then the second singular value will be small.

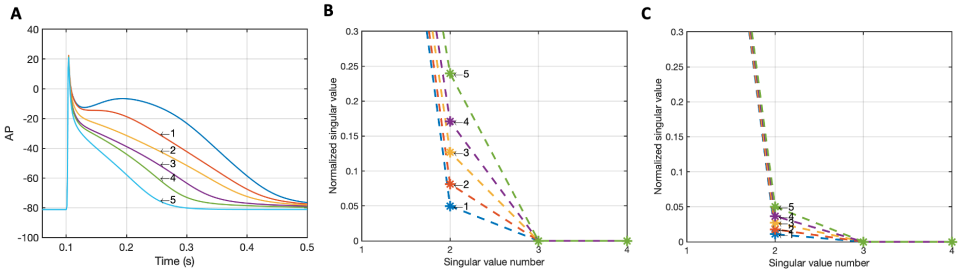

Figure 5.1: Effect of varying signal morphologies at cell level: A) AP morphologies (activation signals), B) resulting normalized singular values with the same number of cells in group 1 and group 2 C) resulting normalized singular values with different number of cells in group 1 and group 2 .

The effect could be calculated in closed form, but is easier appreciated from a simulation. Referring to Fig. 5.1 A), two signal morphologies for the action potential are used: the unmarked blue one, and one of the numbered signals. The signals are derived from the Courtemanche model for a human atrial myocyte, and distinct morphologies are obtained by modifying the calcium current's parameters. A collection of cells are simulated with equal a_c, random τ_c, and a specified fraction assigned to each of the two morphologies. In both cases, signals are scaled to have equal l_2 norm. The resulting singular values are shown in Panel B and C (where σ_1 is normalized to 1, and we zoomed in on the range between 0 and 0.4) . In Fig. 5.1 B), the fraction of cells in either group is equal, while in Fig. 5.1 C), the fraction of cells in either group has a 1:80 ratio. In Panel B, it is seen that the second singular value increases if the second signal is more different. In Panel C, it is seen that the differences are more subtle if there is a significant imbalance in the number of cells between the two groups.

This result extends to more than two different AP morphologies, but although the number of terms in (5.7) increases, the columns $\{\boldsymbol{s}_i\}$ tend to be parallel and at some point the singular values will not increase by much.

Electrogram with single AP morphology, flat wavefront Let us now consider the electrode signals. For a single AP morphology $s(t)$, we obtain from (5.2)

$$\tilde{d}_m(\omega) = \sum_{c=1}^{C} h_{m,c}\, e^{-j\omega\tau_c}\, \tilde{s}(\omega)\,. \tag{5.8}$$

Due to the summation over the cells in (5.8), taking the absolute value $|\tilde{d}_m(\omega)|$ will not have the desired effect of removing the phase factors $e^{-j\omega\tau_c}$. As a consequence, the resulting matrix $\boldsymbol{B}$ constructed from $\tilde{d}_m(\omega)$ will generally have full rank.

Let us make the simplifying assumption that the atrial wave travels in a single flat wavefront (i.e., a plane wave), and that the coefficients $h_{m,c}$ are spatially invariant except perhaps for an electrode gain, as in (5.2). In that case, the phase factors average to

$$\sum_{c=1}^{C} h_{m,c}\, e^{-j\omega\tau_c} \quad =: \quad h_m e^{-j\omega\tau_m} \tag{5.9}$$

where τ_m is the delay for the cell under electrode m. Under this condition, we can again write

$$\boldsymbol{B} = \boldsymbol{h}\boldsymbol{s}^T$$

and only one singular value will be nonzero. A proof of this claim is in the Appendix; the proof shows that it does not matter if the electrodes are in a grid or more randomly placed. The condition of a single flat wavefront describes the situation of a heart in sinus rhythm (SR), with the activating source sufficiently far away from the electrode.

Electrogram with single AP morphology, curved or multiple wavefronts If the wavefront under an electrode is sufficiently curved, then (5.9) does not hold. As a consequence, more singular values will be nonzero. It is hard to analyze this more quantitatively, but if the delay differences are small, then this effect is not expected to be very strong. A curved wavefront occurs if the activating source is close to the electrode, or in case of a nearby focal activation. The effect is shown in Fig. 5.2 A), where we compare two regions (i.e., $\boldsymbol{B}$-matrices) each with 9 electrodes. The tissue is activated in the top-left corner. For Location 1, where the activation wavefront is strongly curved, the second singular value is higher than for Location 2, where the activation wavefront is almost flat. It is also seen that more than two singular values are raised. A stronger effect is expected in case an electrode sees multiple wavefronts. This will significantly destroy the symmetry which was a condition to arrive at a rank-1 model. This case relates to the occurrence of fractionation or double potentials, and therefore is associated with AF. Fig. 5.2 B) shows the effect. The electrodes in Location 2 see a single wavefront, while the electrodes in Location 1 are above a block and see two wavefronts with clearly different LATs. In the latter case, the singular values are substantially raised.

Electrogram with multiple AP morphologies If we have cells with two types of morphologies, then (as before) the rank of $\boldsymbol{B}$ is increased. If the wavefront is still flat, the presence of two cell types will result in rank 2, but for larger numbers the rank will probably be harder to judge. If the wavefronts are curved or we have multiple wavefronts, then the number of nonzero singular value will increase as well.

The effect is shown in Fig. 5.2 C), where two signal morphologies are used. Cells activated from the top-left corner use one type of morphology, and cells activated from the top-right corner use a second type. Location 2 has a curved wavefront but only a single signal morphology, which is similar to Fig. 5.2 A). Location 1 is a region where the two wavefronts collide and two morphologies are present; this further raises the second singular value.

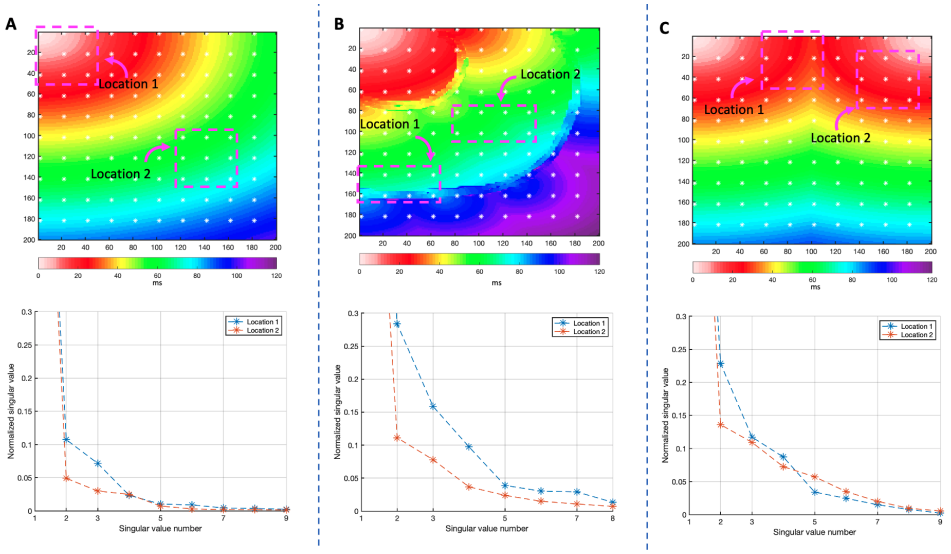

Figure 5.2: Effect of wavefront curvature: A) single wavefront, B) tissue with conduction blocks C) multiple wavefronts with different AP morphologies.
Top row: activation map, bottom row: resulting normalized singular values.

In summary, for the matrix $\boldsymbol{B}$ derived from the EGM, we expect a low rank (only one large singular value) in case there is only one AP morphology and the wavefront is flat, a raised second singular value in case there are multiple AP morphologies and/or the wavefront is curved, and a strongly raised second singular value if some electrodes see multiple wavefronts with clearly different LATs. This suggests that the ratio of the second singular value to the first one (σ_2/σ_1) could be a useful feature for detecting and classifying AF. The advantage of this feature would further be that it is directly derived from the data, without relying on the prior estimation of LATs.

The examples further showed that the maximal σ_2/σ_1-ratio that we can expect is about 0.25.

5.2.5. DEFINITION OF A σ_2 MAP

In the presentation of the method, we defined a data matrix $\boldsymbol{B}$ obtained from the electrode array. In principle, the matrix could encompass the entire array. The examples presented in Fig. 5.2 used subsets of 8 or 9 electrodes, which showed that the normalized singular values vary depending on the location. In locations with a curved wavefront or with multiple wavefronts, the normalized σ_2 is higher than in locations with a flat wavefront and a single AP morphology. If we collect all electrodes in the data matrix, then the location data is averaged, and the differences between the singular values become smaller and harder to detect.

Therefore, to analyze EGM array data with electrodes arranged in a rectangular grid, we propose to use a "σ_2 map", a location-dependent map. We use 3×3 subsets

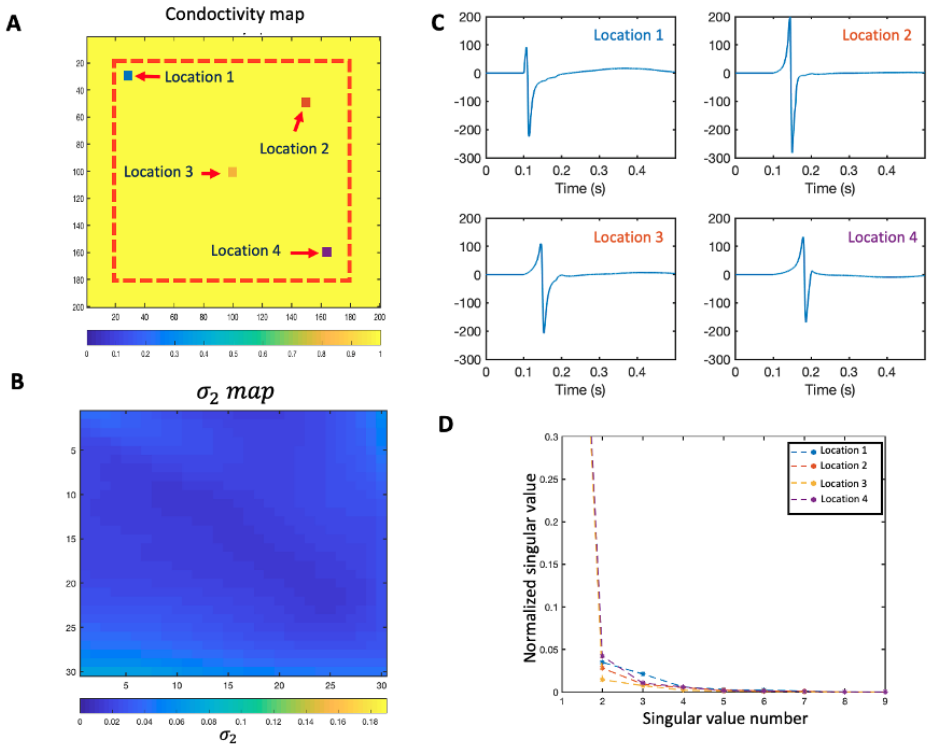

Figure 5.3: σ_2 map analysis of a homogeneous tissue
A) Conductivity map, B) σ_2 map, C) the electrograms at four electrodes, D) normalized singular values for 3×3 subsets of electrodes, centered at these locations.

of the electrode array, and for each subset construct the $\boldsymbol{B}$ matrix and compute the normalized σ_2 value. This gives one pixel in a σ_2 map, located at the center of the subset. The subset is shifted to cover the entire rectangular array, resulting in the σ_2 map.

As an example, Fig. 5.3 and Fig. 5.4 show a simulation[4] where we compare a σ_2 map for a tissue with a homogeneous conductivity (5.3) to a tissue with a conduction block (5.4). A rectangular electrode array with 32×32 electrodes is placed within the area denoted by the red dashed line. The tissue is activated from the top left and a single AP morphology is used. For the homogeneous tissue, all 3×3 subsets result in normalized σ_2 values of less than 0.05. For the tissue with a block, the normalized σ_2 is larger than 0.05 around the block, and is easily recognized in the map. The corresponding time domain signals (e.g., at location 3 and location 4) show double potentials, while in the homogeneous area (e.g., at location 1) we see a single potential. Thus, the σ_2 map can rapidly point out the inhomogeneities and

[4]The details of the simulation setup are discussed later in Section 5.2.6.

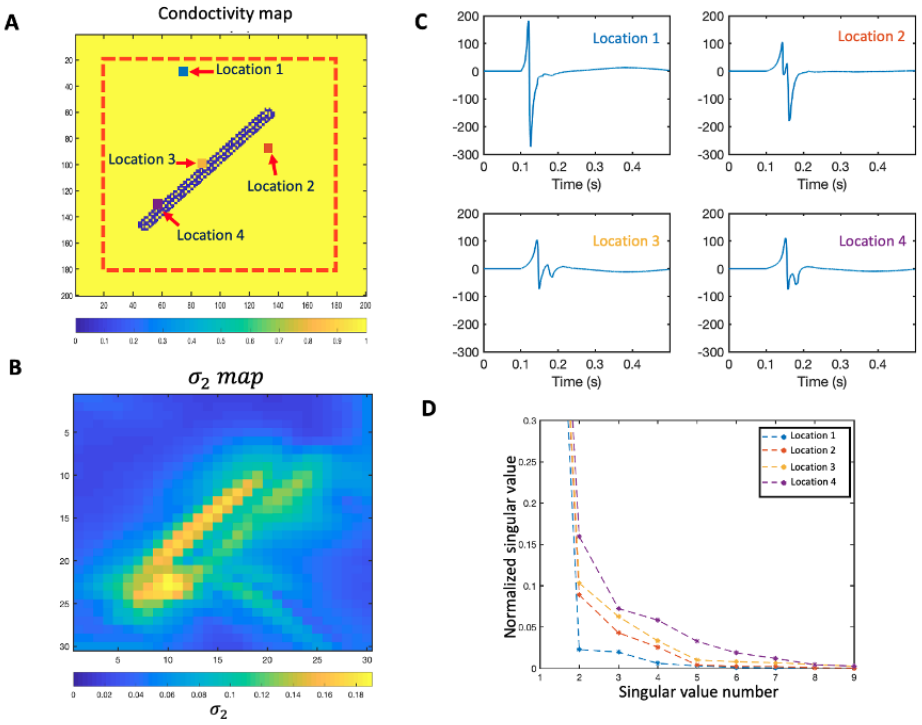

Figure 5.4: σ_2 map analysis of a tissue with a diagonal line of block.
A) Conductivity map, B) σ_2 map, C) the electrograms at four electrodes, D) normalized singular values for 3×3 subsets of electrodes, centered at these locations.

blocks in the tissue. The advantage of this method is that a LAT estimation and analysis is not required for detecting the blocks.

5.2.6. SIMULATED DATA GENERATION

To evaluate the method's performance and reliability, we will use simulated data in Section 5.3. This data was generated as follows.

We simulated a 2D tissue of 200×200 cells. The distance between the cells was 0.1 mm. We considered two conductivity maps. In the first simulated tissue, we have taken into account a homogeneous tissue where the conductivity is constant throughout the tissue. For the second simulated tissue, two different conductivities have been used: specific cells have a constant conductivity of $c_1 = 1$, whereas the others have a constant conductivity of $c_2 = 0.01$.

The AP signals of the cells are generated at a resolution of 1 kHz, using the Courtemanche model as implemented in [131, 132]. We generated APs with two different morphologies, which are shown in Fig. 5.5 as AP1 and AP2. For visualization

purposes, activation maps are generated by detecting the activation time as the instant when a cell crosses a threshold of −40 mV during the depolarization phase of the AP. To activate the tissue, two wavefront directions have been used. The first

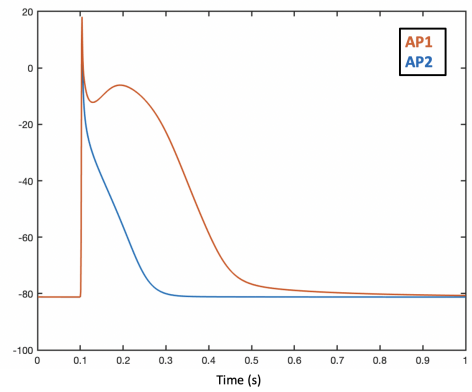

Figure 5.5: Two simulated morphologies for the action potentials.

wavefront originates from the top-left corner, and the second is from the top-right corner. The electrogram signals were observed by a rectangular electrode array of 10×10 electrodes with inter-electrode distance of 2 mm, at a constant height of $z_0 = 1$ mm from the tissue. To increase the resolution in the σ_2 map analysis, we increased the number of electrodes in the electrode array to 32×32 electrodes with an inter-electrode distance of 0.5 mm.

5.3. RESULTS

From Section 5.2, the hypothesis is that the normalized σ_2 value is a useful indicator to detect and classify cases of AF. This is tested on both simulated and two types of clinical data. In this chapter, we show the simulation results, and in Chapter 6, the clinical results are shown. We used the entire data matrix to demonstrate the general characteristics of AF by the normalized singular values. While using submatrices to locate the electropathological areas in the tissue allowed us to learn more about the spatial distribution of the AF substrate in the tissue.

5.3.1. SIMULATION SETUP

We compare three cases. In the first case, we generated a homogeneously conducting 2D tissue in which the AP is initiated from the top-left corner and propagates throughout the tissue. The activation map and electrograms at a few selected electrodes are shown in Fig. 5.6. As can be seen, the electrograms have similar morphologies, with a single deflection (a so-called single potential).

For the second case, we generated one wavefront with two different AP morphologies. The activation map and selected electrograms are shown in Fig. 5.7;

the areas with two different morphologies are indicated by rectangles. Fractionated potentials can be seen in the electrograms.

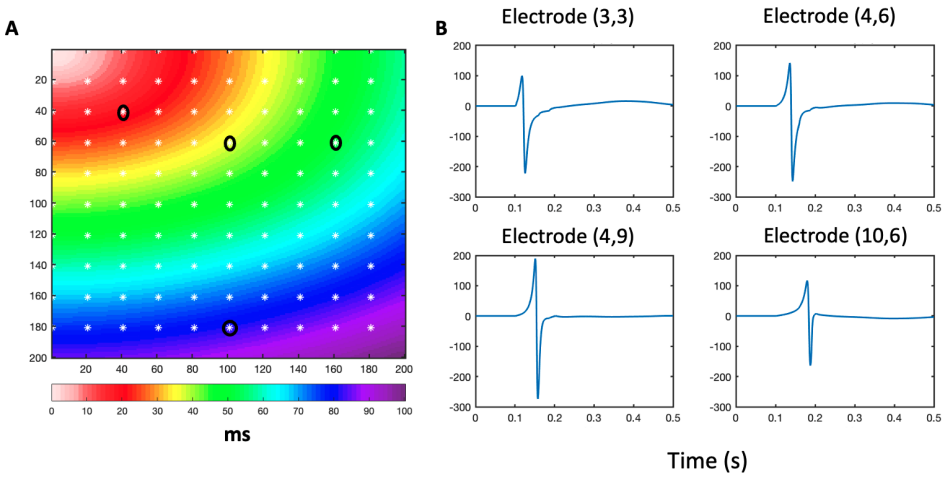

Figure 5.6: One wavefront, one AP morphology: activation map, and example electrograms.

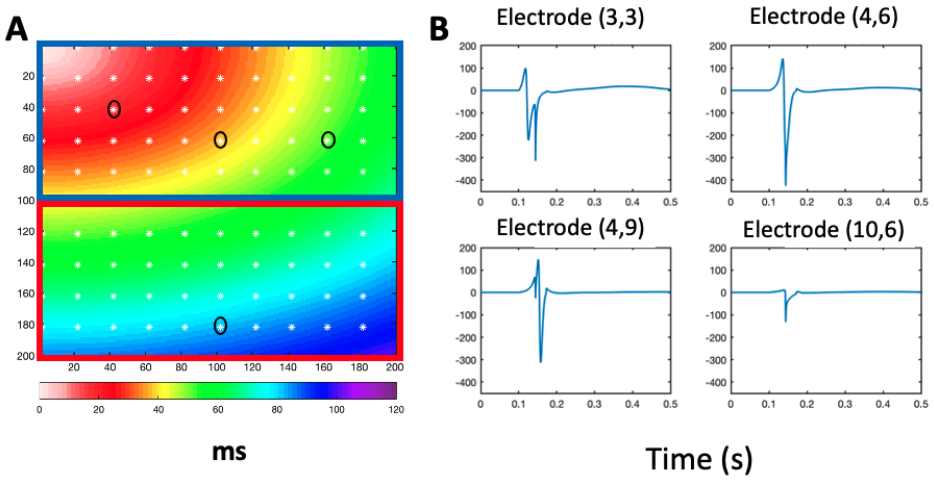

Figure 5.7: One wavefront with two conduction areas with different AP morphologies: activation map and electrograms.

For the third and fourth cases, we generated two wavefronts, activated from the top-left and top-right corners of the simulated tissue. The conductivity was

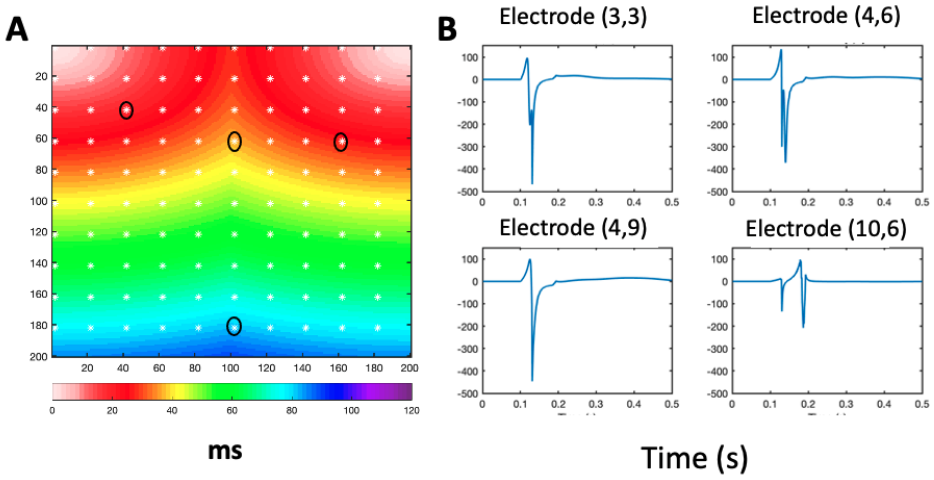

Figure 5.8: Two wavefronts with two different AP morphologies: activation map and electrograms.

homogeneous, and the two wavefronts collided on the center axis. In the third case, the cells at the left and the right generated the same AP morphology, while in the fourth case, the cells at the left and the right generated different AP morphologies AP1 and AP2 (Fig. 5.5). Due to the similarity between these two cases, we have shown the activation map and example electrograms only for the fourth case in Fig. 5.8. Some electrograms are fractionated, and this is more pronounced at the locations of wave collisions.

5.3.2. SIMULATION RESULTS

The three scenarios are first tested at the cell level. The results are in Fig. 5.9 A). The figure shows that the normalized singular values of the $\boldsymbol{B}$-matrix are increased only by the variety of AP morphologies, but not by the number of wavefronts. This is because at the cell level, the $\boldsymbol{B}$-matrix is not sensitive to activation time.

However, at the epicardial level (Fig. 5.9 B), it is seen that the normalized singular values of the $\boldsymbol{B}$-matrix are increased in all cases. For the case with 1 wavefront and 1 AP morphology, this is because the wavefront is curved. For the other cases, it is a combination of the curved wavefronts and the variation in the AP morphology. Also with a single AP morphology, the fact that there are 2 colliding wavefronts will increase the singular values. These effects are apparently not additive: the first scenario gives a normalized σ_2 value of 0.15, the other scenarios result in 0.24.

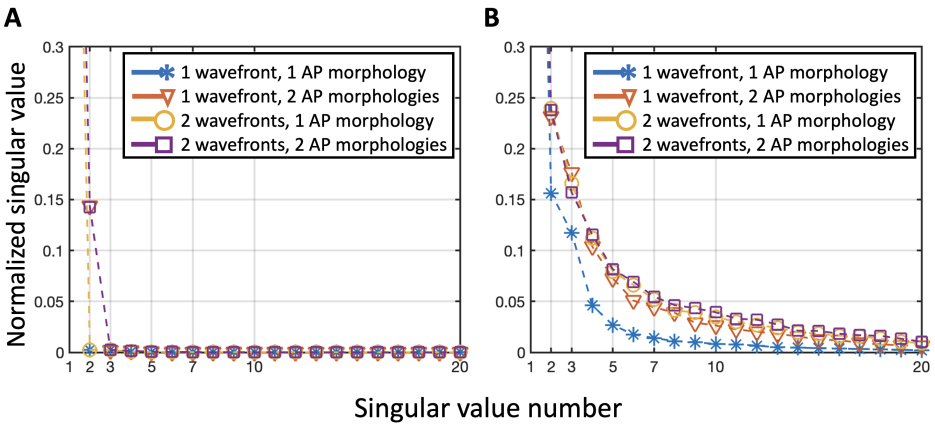

Figure 5.9: Simulated data: normalized singular values using the entire data matrix. A) cell level, B) epicardial level.

5.4. CONCLUSION

In this chapter, we developed a method to analyze the heart's electrical activity from different observation levels. We have shown that the singular values of the data matrix could be used to detect double potentials, abnormal wavefront propagation, simultaneous presence of multiple action potentials morphologies, and conduction blocks. In this chapter, the performance of the method has been evaluated using simulated data. In the next chapter, we assess the proposed method using different types of clinical data.

5.5. APPENDIX: PROOF OF THE CLAIM IN SECTION 5.2.4

We prove this for a continuous cell distribution in 1D space. For a traveling plane wave, the cell voltage as function of position x is

$$c(x,t) = s(t - \frac{x}{v})$$

where v is the propagation velocity. (Equivalently, the propagation delays τ are a linear function of position x.) For simplicity, we assume cells have an equal gain normalized to 1. In the frequency domain this then becomes

$$\tilde{c}(x,\omega) = S(\omega)e^{-j\omega x/v}.$$

The spatial response of an electrode centered at location 0 is some function $f(x)$; the example in (5.2) would in this context be $f(x) = a/|x|$. Assuming the response is linear space-invariant, the electrode voltage measured at a location y is the convolution integral

$$m(y,t) = \int c(x,t)f(y-x)dx = \int c(y-x,t)f(x)dx$$

In frequency domain, this becomes

$$\begin{aligned}\tilde{m}(y,\omega) &= \int S(\omega)e^{-j\omega(y-x)/v} f(x)dx \\ &= S(\omega)e^{-j\omega y/v}\int e^{j\omega x/v} f(x)dx \\ &=: S(\omega)e^{-j\omega y/v} I(\omega)\end{aligned}$$

Taking the absolute value gives

$$|\tilde{m}(y,\omega)| = |S(\omega)I(\omega)|$$

which is not a function of position y anymore. Sampling over y and ω, the corresponding measurement matrix $\boldsymbol{D}$ will be rank 1. Generally, $\boldsymbol{D}$ will be rank 1 if we are able to factorize $|\tilde{m}(y,\omega)|$ as $|\tilde{m}(y,\omega)| = A(y)B(\omega)$. This also shows that we can permit electrodes to have different gains (as long as they are frequency-independent): this results in a different factor $A(y)$ but will not increase the rank.

Generalizing the derivation, we observe that if cells have unequal gains $a(x)$, i.e., $c(x,t) = a(x)s(t-\frac{x}{v})$, we will have rank 1 only if we can factorize $a(y-x)$ into separate factors depending on y and x. It follows that $a(x)$ must be of the form $a(x) = e^{\alpha x}$. For small α, this can be linearized to $a(x) = 1+\alpha x$. Thus, we can permit a small gain gradient over the cells.

If the wavefront is curved, the delays are a nonlinear function of x, e.g. $\tau = \left(x+\frac{a}{x}\right)/v$. It is easily seen that in this case, $|\tilde{m}(y,\omega)|$ does not factorize, so that $\boldsymbol{D}$ will have rank higher than 1.

6

EVALUATION OF THE SINGULAR-VALUE-BASED MARKER ON CLINICAL DATA

In the previous chapter, we developed a method to detect regions with abnormal atrial activity. The method is based on the singular value decomposition, which can extract the spatial variation of the atrial potential morphologies. We also assessed the proposed method on the simulated data, considering different scenarios for wavefront propagation and action potential morphology. In this chapter, we evaluate the proposed method using two types of clinical data. Furthermore, we introduce a new measurement system to simultaneously record body surface potentials (BSP) and EGMs.

6.1. CLINICAL DATA

The clinical data is part of the Halt & Reverse study, approved by the medical ethical committee (MEC 2014 – 393), Erasmus University Medical Center, Rotterdam, the Netherlands. In this chapter, we have included two types of clinical data. The first one is EGM data measured from 9 recording locations, shown in Fig. 6.1-top during open heart surgery. The second clinical data is the simultaneous measurement of body surface potentials and EGMs during minimally invasive surgery.

6.1.1. ELECTROGRAM DATA COLLECTION

High-resolution epicardial unipolar EGM data was collected at the Erasmus Medical Center (EMC) during open-heart surgery on patients without a history of AF, as described in more detail in [56]. Fig. 6.1-top shows the standardized 9 recording locations; at each location, a recording consists of 5s of SR followed by 10s of

This chapter is based on a paper submitted as "H. Moghaddasi, R. C. Hendriks, B. Hunyadi, M. van Schie, P. Knop, N. M. S. de Groot, and A. J. van der Veen, *A Singular-value-based Marker for the Detection of Atrial Fibrillation Using High-resolution Electrograms and Multi-lead ECG*"

induced AF. The electrograms were recorded using a rectangular electrode array with 8×24 electrodes where the inter-electrode distance was 2 mm and the electrode diameter was 0.45 mm. The signals were amplified, filtered to a frequency range between 0.5 and 400 Hz, sampled at a rate of 1 kHz with resolution of 16 bits, and stored. One lead was used to record the ECG. During data analysis, we filtered the signals using a Butterworth band-pass filter in the frequency range between 0.33 Hz and 30 Hz [36, 102, 133]. The Pan-Tompkins R-peak detection method [134] was used on the ECG lead to segment the atrial activity of each EGM. To select the atrial activity, we used a fixed window with a length of 260 ms and select the interval between 320 ms and 60 ms before the R-peak [127]. This resulted in $N = 130$ frequency-domain samples per beat.

For the EGM data analysis, we included five patients without a history of AF. We pre-screened the available heartbeats using these exclusion criteria: 1) electrically silent heartbeats; 2) heartbeats where the fibrillatory waves are absent in the fixed window. As a result, the number of patients per location varies between 3 and 5, where between 2 and 23 heartbeats are included per patient. In total, 189 and 395 heartbeats are used for SR and AF episodes, respectively. More details about the number of heartbeats per location are reported in Table 6.1.

Table 6.1: Number of selected heartbeats per location

Mapping location	# SR heartbeats	# AF heartbeats
BB0	19	28
LA1	22	51
LA2	17	38
PVL1	20	19
PVR1	24	35
RA1	23	41
RA2	22	60
RA3	22	58
RA4	20	65

To compare the patients without a history of AF with those with a history of AF, we have further included 20 patients with a history of paroxysmal AF during SR and AF episodes. This data is only measured at the RA2 location (Fig. 6.1). To do so, we used 52 heartbeats of these patients during SR and 134 heartbeats of induced AF from patients with a history of AF at the RA2 location.

6.1.2. BODY SURFACE POTENTIAL DATA COLLECTION

To be able to simultaneously measure high-resolution epicardial EGMs and multi-lead body surface potentials (BSPs), we designed a novel sub-vest to record the BSPs during minimally invasive surgery. We placed the 15 electrodes of the vest at the locations indicated by the circles in Fig. 6.1, where black circles denote the electrodes on the front and red circles denote the electrodes on the back of the patient. This design was motivated as follows. First, the area highlighted in the

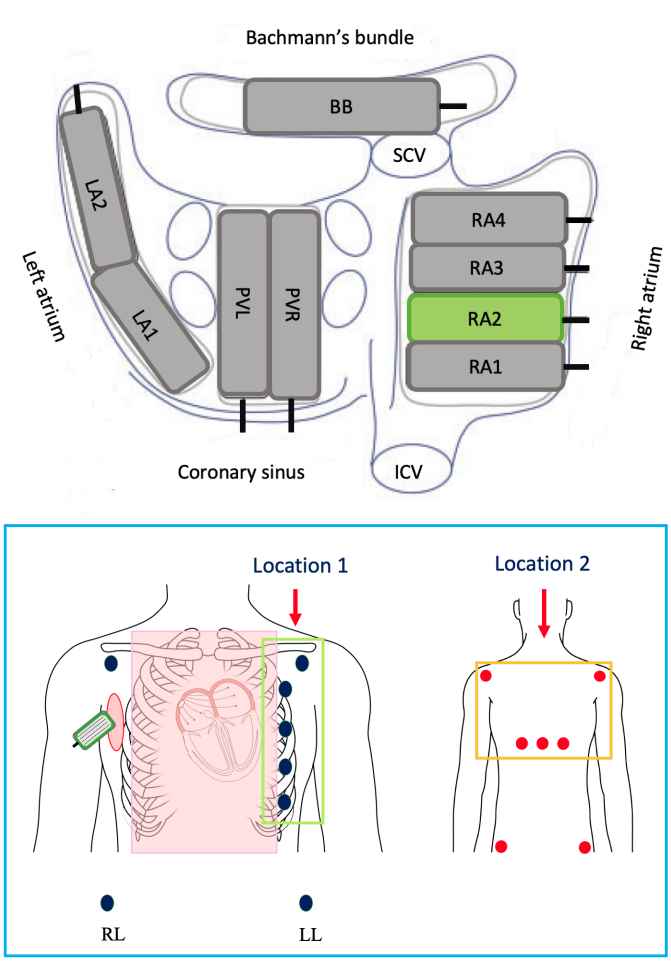

Figure 6.1: (Top) EGM measurement locations from the posterior view of the atria. (Bottom) Setup to simultaneously measure the EGM at location (RA1, RA2 or RA3) and body surface potentials with 15 electrodes, during minimally invasive surgery. Location 1 and 2 are designated subsets of 5 electrodes on the front and back of the patient, respectively.
We recorded data from all 9 standardized locations (shown on top) for the EGM data collection, and for the combined EGM and BSP measurements, we recorded at RA1-RA3.
Right atrium (RA), left atrium (LA), right pulmonary vein (PVR), left pulmonary vein (PVL), Bachmann's bundle (BB), superior caval vein (SCV), inferior caval vein (ICV).

faded color, called the sterile field, is inaccessible during minimally invasive surgery. Second, the atrial activity is a focus of this investigation. Since the atrial activity is generated during the depolarization phase, we covered an area that captures this, i.e.

optimized for a heart axis between -30 and +90 degrees. Additionally, to capture the atrial activity from the back of the patient, we positioned three electrodes close to the atrium on the back. For practical reasons, we had to limit the total number of leads. We used 15 prewired disposable electrodes from Nissha Medical Technologies (NMT), with the code CLARAVUE 4009839C, which are attached to the patient before starting the surgery. A 6-7 cm incision called an auxiliary port is made in the third or fourth intercostal space to perform the surgery. After positioning the electrode array to the right atrium at three locations marked RA1, RA2, and RA3 in Fig. 6.1, high-resolution electrograms and multi-lead BSPs were simultaneously measured.

We acquired measurements from 1 male patient without a history of AF. The patient underwent mitral valve prolapse (MVP) surgery. The left ventricular ejection fraction (LVEF) was normal, and the body mass index (BMI) was 26.5. We recorded for 30s during SR and 30s during an induced AF episode. A similar filtering and segmentation approach has been implemented for the BSP measurements.

6.2. RESULTS

We applied the proposed method, normalized singular values, to the clinical EGM data. Section 6.2.1 shows the differences between the singular values of SR and AF heartbeats at 9 recording locations. In Section 6.2.2, the combined EGM and BSP results are shown.

6.2.1. EGM RESULTS

Fig. 6.2 shows in blue and red faded lines the normalized singular values for each heartbeat during the SR and AF episode per location. The averages over the heartbeats are shown in bold blue and red. It is evident that the singular values are higher during AF heartbeats than during SR heartbeats. Arrows show the range of normalized σ_2 values, which is smaller for SR than for AF.

The distribution of the normalized σ_2 over the heartbeats is shown more clearly in Fig. 6.4. It can be seen that there is a significant difference between the normalized σ_2 during SR and the normalized σ_2 during AF (P-value < 0.001 for all mapping locations). These results show that the normalized σ_2 is a helpful feature to discriminate between SR and AF. The threshold to separate the distributions appears to be location specific.

To compare our results with patients who have a history of AF, we have included paroxysmal AF patients in our study. The results for paroxysmal patients are shown in Fig. 6.3. As can be seen, the normalized second singular value of paroxysmal AF patients during an AF episode is again distinctively higher than for those in SR. Comparing Fig. 6.2 (at the RA2 location) and Fig. 6.3, it is observed that the range of the normalized σ_2 in patients with a history of AF (paroxysmal AF (PAF) and paroxysmal SR (PSR)) is only slightly higher than for individuals without a history of AF, in particular for the SR episodes. This is more clearly seen in Fig. 6.4 (last column, marked RA2-PAF). Note that PSR heartbeats refer to heartbeats during SR in patients with a history of paroxysmal AF.

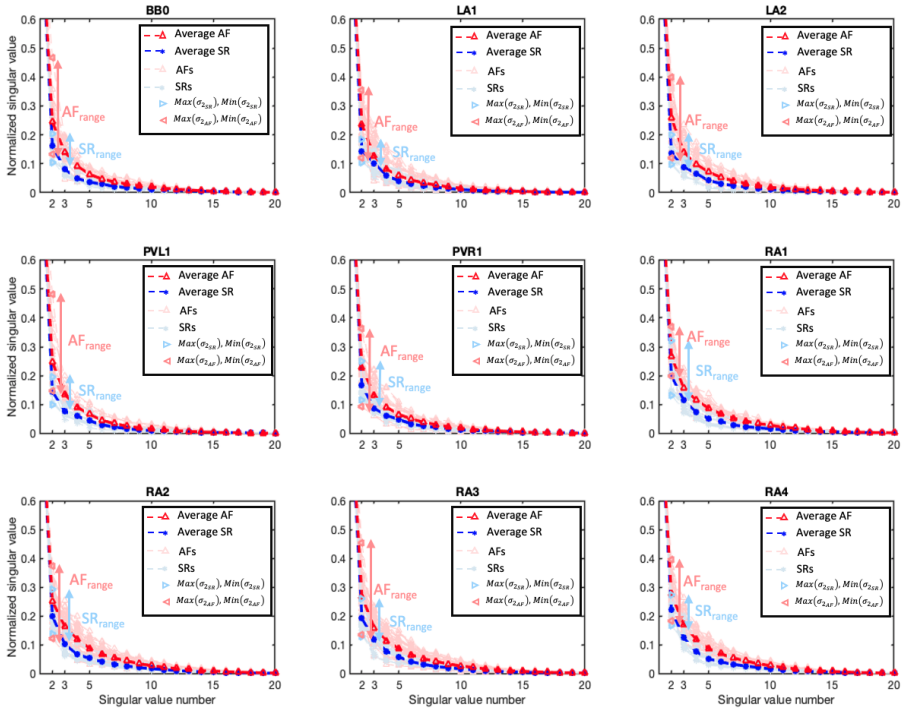

Figure 6.2: EGM clinical data: Normalized singular value analysis for each heartbeat per location. The bold lines show the average.

6.2.2. COMBINED ELECTROGRAM AND BODY SURFACE POTENTIAL DATA RESULTS

For the combined EGM and BSP data, we investigated the singular values of the $\boldsymbol{B}$ matrix during SR and induced AF on a single patient without history of AF. Fig. 6.5 shows a segment of one lead of the measured data where the patient was in AF for 5s and then the rhythm returned by itself to the normal sinus rhythm. The EGM and BSP data has been measured simultaneously. It can be seen in Fig. 6.5 that on the BSP measurement, during AF, the P wave is replaced by the fibrillary waves or the absence of a P wave. Besides, there is a significant variation in the RR intervals during AF compared to SR. However, the difference between the SR and AF is more pronounced in EGM data. In the atrial activity measured in the EGM, a single potential can be seen in each heartbeat during SR. While in the case of AF, a single potential is replaced by double potentials, multiple potentials, or fractionated potentials, sometimes coinciding with ventricular potentials visible during the AF episode. These distinctive characteristics contribute to the chaotic pattern observed in the BSP.

The normalized singular values for the SR and AF heartbeats for both EGMs and

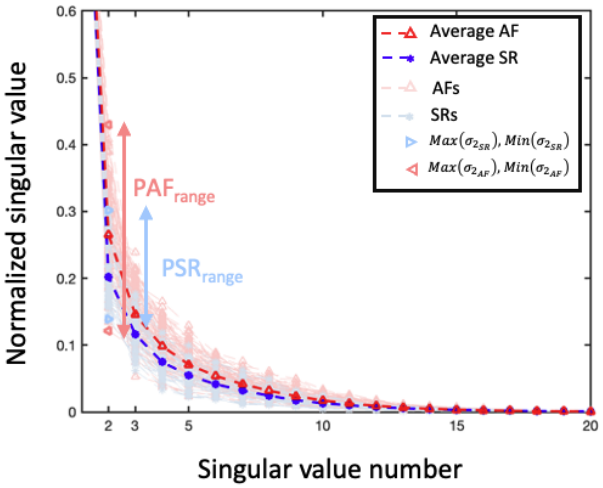

Figure 6.3: Normalized singular value analysis at the RA2 location in patients with a history of paroxysmal AF.

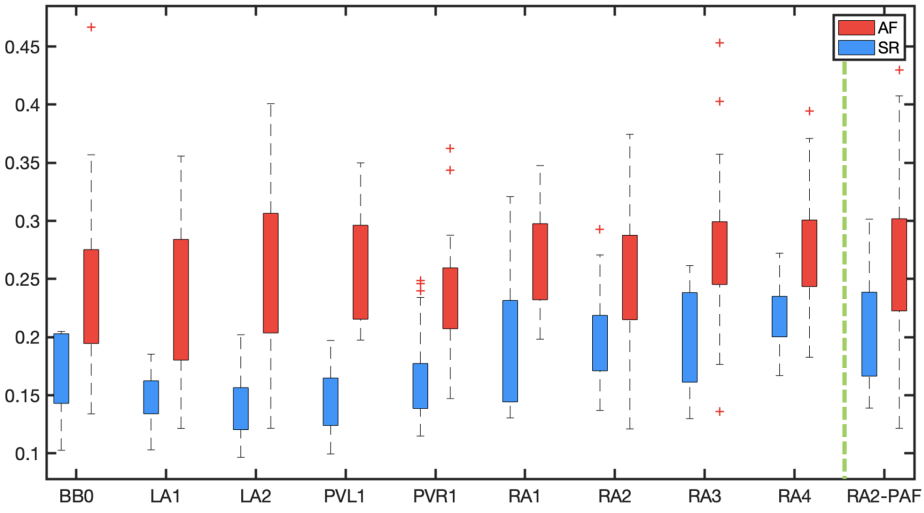

Figure 6.4: EGM clinical data: Box plot showing the distribution of the normalized σ_2 over the heartbeats for each of the mapping locations. Within the box, values between the 25th and 75th percentiles are shown. RA2-PAF denotes patients with a history of paroxysmal AF measured at the RA2 location.

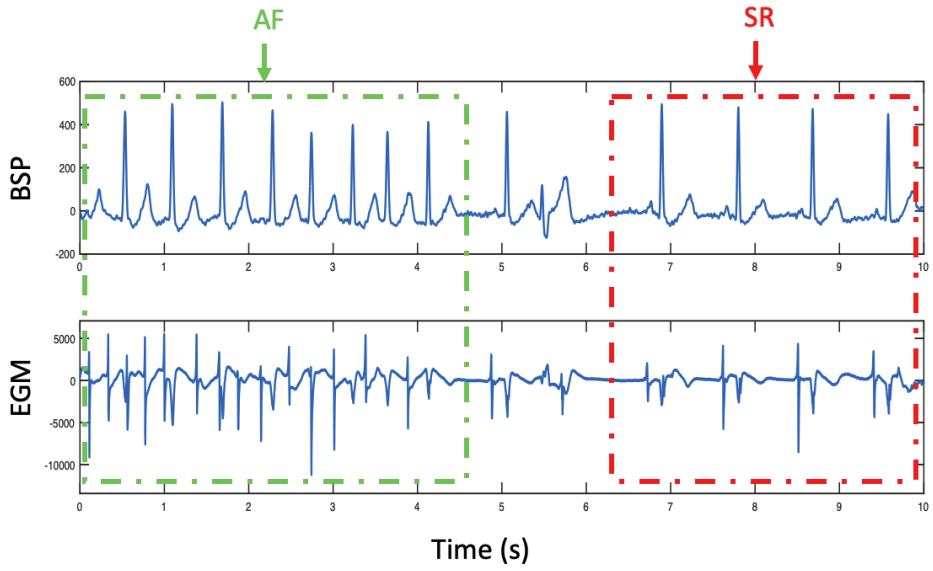

Figure 6.5: One lead from the BSPs and one lead from EGMs containing AF and SR heartbeats.

multi-lead BSPs are shown in Fig. 6.6, using the data at location RA1. The average singular values across the heartbeats are shown in bold blue and red for the SR and AF beats, respectively. It can be seen that the singular values of the heartbeats during AF are higher than during SR. This difference is somewhat more pronounced for the BSP data than for the EGM data: the average normalized σ_2 is 0.29 during AF and 0.19 during SR.

To study this in more detail, we sub-divided the BSP data to investigate the location dependency of the singular values. Referring to Fig. 6.1 and Fig. 6.7, we took 5 electrodes in the anterior plane, denoted by the green box (*location 1*), and 5 electrodes in the posterior plane, denoted by the orange box (*location 2*). At location 1, the average singular values of the AF beats are strongly higher than the average singular values of the SR beats (σ_2 at 0.35 vs. 0.22). In contrast, at location 2, the average singular values of the SR and the AF beats are similar (σ_2 at 0.15). This demonstrates that the presence of abnormal regions is not visible in all electrodes, and a selected subset might show a stronger response than the full data matrix.

The EGM data at the location RA1 can be studied in more detail using the activation map and the σ_2 map. A single heartbeat during SR is shown in Fig. 6.8 A. The wave propagation starts from the bottom-left corner, denoted by grey in the activation map. The wavefront propagation is shown by the black arrow, which is analysed by a qualified physician. The wavefronts appear to be flat (linear) in most of the map. Using an overlapping 3×3 electrode array (e.g., the area indicated by the pink square), we construct the σ_2 map shown in Fig. 6.8 B). Generally, the normalized σ_2 is less than 0.1 (blue color), except for a few regions. It demonstrates

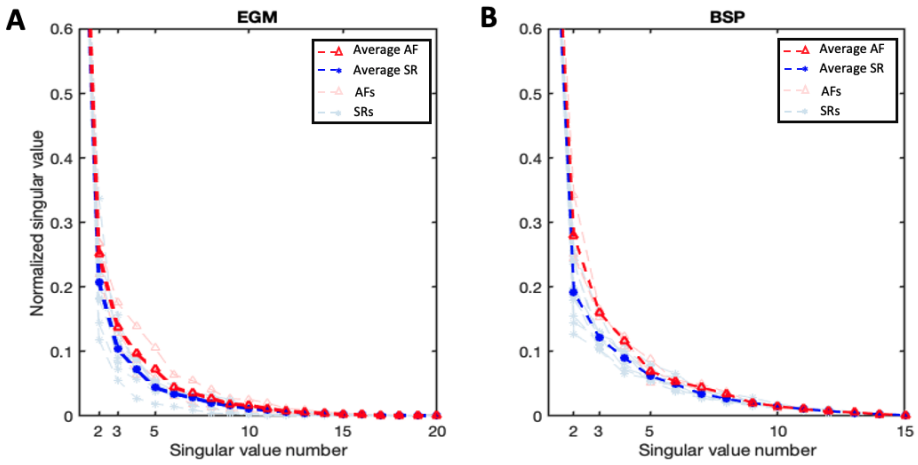

Figure 6.6: Singular values of each heartbeat during SR and AF episodes using simultaneous EGM and BSP measurements. A) EGM data at the RA1 location, B) BSP data. The bold lines show the average.

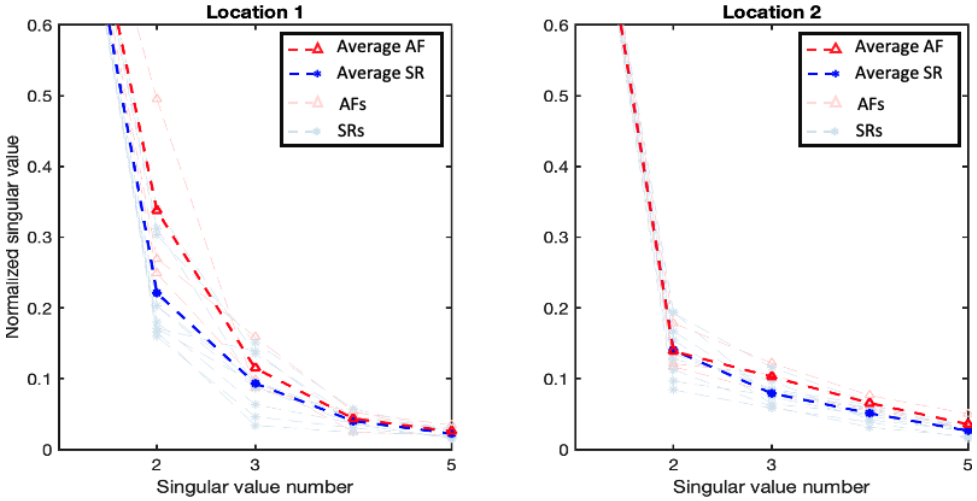

Figure 6.7: Effect of BSP electrode location on the normalized singular values for two selected subsets of 5 electrodes.

that on the areas with a flat wavefront, the rank 1 approximation in Section 5.2.4 holds. However, at location 1, the normalized σ_2 is about 0.25 (yellow color). The corresponding EGM in Fig. 6.8 C) shows that location 1 has a double potential. This abnormality is not seen in the activation map. In other words, while the LATs remain normal, the σ_2 map visually indicates areas with altered morphology.

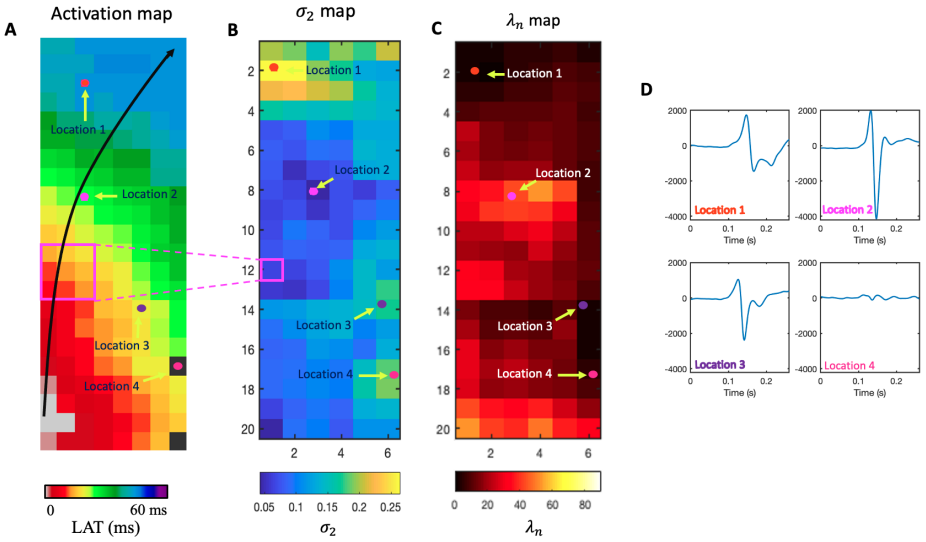

Figure 6.8: σ_2 map analysis in SR, A) activation map, B) σ_2 map, C) λ_n map [128] D) EGMs at four electrodes. The black arrow in the activation map shows the wavefront propagation.

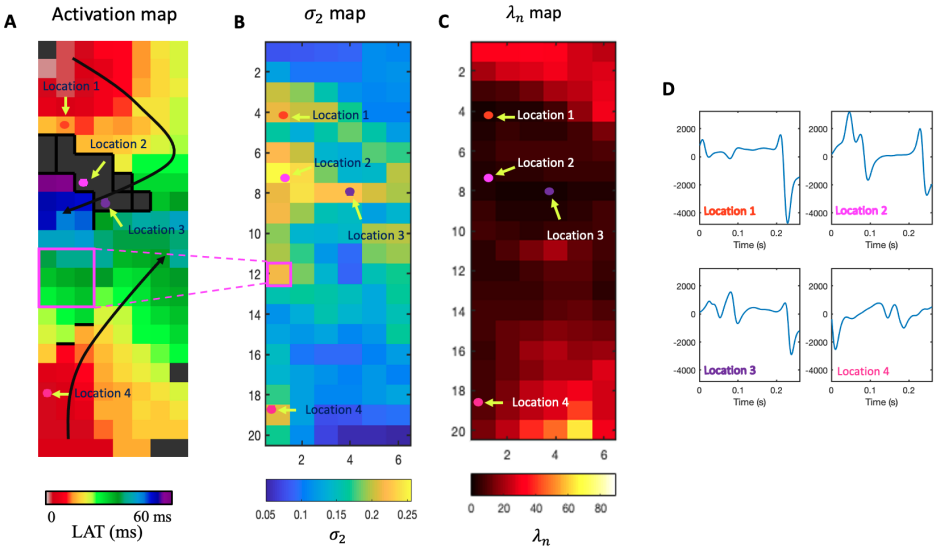

Figure 6.9: σ_2 map analysis in AF, A) activation map, B) σ_2 map, C) λ_n map [128] D) EGMs at four electrodes. The black arrows in the activation map show the wavefront propagation.

The activation map for a single heartbeat during the induced AF episode is shown in Fig. 6.9 A). It can be seen that the tissue under the electrode array starts to

be activated at multiple locations (bottom left and top left). Furthermore, some areas have conduction blocks (CB), as marked by the bold black lines. A CB is declared when the LAT difference between two adjacent electrodes is greater than or equal to 12ms [13, 14]. The σ_2 map for the same heartbeat is shown in Fig. 6.9 B). At the area with CB around locations 1, 2 and 3, we observe that $\sigma_2 \geq 0.2$ (orange/yellow color), while in the areas where the wave propagates normally, the σ_2 is less than 0.1 (blue color). Looking at the corresponding EGM examples in Fig. 6.9 C, at locations 1-3 we observe signals with a double potential followed by a single potential. It demonstrates that the double potential regions can be detected by the σ_2 map. Further, at location 4, the activation map shows normal wave propagation, while the σ_2 is greater than 0.2 (orange color). The EGMs at location 4 shows a single potential followed by a double potential. Thus, the σ_2 map can point at double potentials in some regions while these are not visible in the activation map. Conversely, the activation map shows some CB (black lines) above location 4, while the σ_2 map gives no trigger at this location.

6.3. DISCUSSION

Summarizing the results, we have shown that the normalized σ_2 of the $\boldsymbol{B}$-matrix from subsets of electrode data is sensitive to curved wavefronts, conduction blocks, and variations in AP morphology. These changes can be detected in EGMs and also in multi-lead ECGs, if the electrodes are positioned at favorable locations. Further, we have seen that the σ_2 map is a useful tool for detecting such changes, complementary to the use of activation maps.

An increased normalized σ_2 is often related to the occurrence of double potentials or simultaneous presence of multiple AP morphologies in the considered subset of electrodes. These are often associated with AF. In the clinical data, we showed that the heartbeats annotated as AF always scored higher than heartbeats in SR.

If we assume that AF initiation and progression can be modeled by a variation in the morphology of APs, then the normalized σ_2 can be a useful feature to detect such changes. The array data can be processed for each individual heartbeat, and by tracking the normalized σ_2, we can efficiently monitor the evolution of a patient over time.

Related work has been done by Riccio et al. [128], who developed "eigenvalue dominance ratio" maps, which are based on the singular values of the data matrix (or equivalently the eigenvalues of the associated sample covariance matrix) constructed from unipolar (catheter) electrograms. This data matrix contains the time-domain traces of each electrode. The method requires to time-align these traces by estimating the local activation time in each trace, which is done via an iterative process that maximizes the cross-correlations of the traces. After proper time alignment, the method detects the similarity of the AP morphologies, with the goal of the detection of fibrotic areas. The main distinction with our work is (i) it requires time-alignment, which is not always easy to achieve and relies on an underlying parametric model that does not account for fractionation; (ii) it works in the time domain rather than on the amplitude spectra, hence includes more phase

information. This makes the methods not directly comparable.

To compare both methods, Fig. 6.8 C) and Fig. 6.9 C) show the maps produced by the method of Riccio et al. (we will call it λ_n map). Note that the color maps are different due to the different normalization techniques: in Riccio's method, lower numbers (black areas) correspond to abnormalities. Looking qualitatively at the localization of conduction blocks, it appears that the proposed method provides improved localization.

In our proposed method, we took the element-wise absolute values of the Fourier spectra. This removes time-delay effects and allowed us to study changes in the morphology's dispersion without estimating the LAT. At the same time, the LAT (or phase of the $\boldsymbol{D}$-matrix) can be regarded as independent, complementary information. It thus makes sense to look at both the activation map and the σ_2 map together.

6.3.1. LIMITATIONS AND FUTURE WORK

In this chapter, we took the method proposed in Chapter 5, and evaluated it on clinical data. For consistency and to avoid patient group differences between SR and AF, we used the SR and induced heartbeats from the same patients. This approach posed a limitation in our data acquisition, where the patient needed to be in SR and subsequently induced AF, which wasn't available for some mapping locations for both cases. Therefore, we evaluated our method on 5 patients without a history of AF in all 9 mapping locations and on 20 patients with a history of paroxysmal AF in one mapping location (RA2).

Furthermore, the proposed method computes the Fourier spectra of the measured signals and takes the absolute value. This step suppresses half the information present in these signals. In particular, the suppressed phase has all information on the local activation times. Thus, the proposed σ_2-map has independent information from the traditional activation maps. Future research should address the integration of these two feature maps, and relate them to the hidden electropathological parameters of the tissue such as conductivity.

Our study has shown that there are clear differences in normalized σ_2 between SR and AF-type array measurements. However, the results in Fig. 6.4 show that it is hard to propose a fixed threshold to distinguish between these two cases. Such a threshold would vary between 0.2 and 0.25 depending on location and other factors, such as the height of the electrodes above the tissue (z_0). Similarly, the BSP data (Fig. 6.7) has shown that at some locations, no difference is found. Thus, array placement is an issue that needs further study.

We have shown σ_2-maps based on 3×3 electrodes and a single beat. These highlight locations that deserve further attention. Alternatively, we have also shown plots (Fig. 6.2 and Fig. 6.6) where the normalized σ_2 of the entire array is computed (in a sense, averaging over space), and we could average that over multiple beats. That allows to compress a larger data set into a single feature. An open question is whether this averaging will dilute the differences between SR and AF such that this feature is not sufficiently discriminative anymore.

In this respect, Fig. 6.6. A and Fig. 6.6. B show that the difference between the normalized singular values during AF and SR heartbeats is higher for the BSP

(or ECG) data than for the EGM data. Our hypothesis for this observation is that the ECG captures the entire cardiac electrical activity while EGM only measures a subset of the heart. Therefore, areas of abnormalities may not be captured through the EGM measurement at a single location. Note that this hypothesis needs further investigation before arriving at a definitive conclusion.

For the σ_2-maps such as Fig. 6.8 and 6.9, we have shown that areas of increased σ_2 correspond to EGMs with double potentials or related irregularities. We did not demonstrate the reverse, namely that *all* irrregular EGMs are highlighed in the σ_2-map.

6.4. CONCLUSION

In Chapter 5, we developed a method for analyzing EGM and multi-lead ECG data. In this chapter, we evaluated the performance of the developed method on clinical data. The method is non-parametric and requires little preprocessing. We have shown that the singular values of the processed data matrix give information on inhomogeneity of the AP morphologies, and the related σ_2-map points at areas subject to fractionation and block. The method gives a clear distinction between heartbeats in SR and AF.

Further, experiments using simultaneous EGM and multi-lead ECG measurements showed that the singular values of the heartbeats during AF are higher than during SR, and that this difference is more pronounced for the ECG data than for the EGM data, if the electrodes are positioned at favorable locations. Our related results show that the proposed singular value features can be a useful indicator to evaluate AF. In the next chapter, we present a clinical application of the proposed method to differentiate between paroxysmal and persistent AF using singular-value-based features.

7

SEVERITY DETECTION OF ATRIAL FIBRILLATION: DURING SINUS RHYTHM

In Chapter 5 and Chapter 6, we developed a method to analyze the spatial variation of the atrial activity in the heart and evaluated the method on clinical data. In this chapter, we study a specific case of AF severity detection in patients with atrial fibrillation history during an SR episode. As discussed in Section 2.2.3, although the exact mechanism of AF is unclear, electropathology of atrial tissue is one contributing factor. Electropathological characteristics derived from intra-operative epicardial measurements, such as conduction block (CB) and continuous conduction delay and block (cCDCB), can be used to assess the severity of AF. In sinus rhythm, however, these parameters do not indicate significant difference between different development stages of AF, such as paroxysmal and persistent AF. Therefore, we propose a methodology to improve AF severity detection using intra-operative electrograms. We will propose a tool that describes the spatial diversity of atrial potential waveforms during a single beat on the multi-channel electrograms to discriminate between paroxysmal and persistent AF. Based on this method, we will derive two novel features.

7.1. INTRODUCTION

Severity detection of atrial fibrillation becomes more challenging in two specific scenarios. The first one is when the data collected from the patient only contains AF episodes. We have addressed this question in Chapter 4 by extracting features based on morphological and rhythmic changes. The second challenge is when the collected data only contains SR episodes, but the patient has a history of atrial

This chapter is based on a paper published as "H. Moghaddasi, R. C. Hendriks, A. J. van der Veen, N. M. S. de Groot, and B. Hunyadi, *Novel Rank-based Features of Atrial Potentials for the Classification Between Paroxysmal and Persistent Atrial Fibrillation*, Computing in Cardiology (CinC) conference, 2022, IEEE."

fibrillation. In this case, while the surface ECG indicates a normal sinus rhythm, the intra-operative electrograms at various recording locations may not necessarily demonstrate normal patterns. In this work, we go one step deeper from the surface of the body (i.e., from ECGs) to the surface of the heart (i.e., to electrograms) to gain more insights into the electropathology of AF.

AF is classified into four categories based on the duration of an episode: paroxysmal, persistent, long-standing persistent, and permanent AF [28]. In this chapter, we focus, in particular, on the classification between paroxysmal AF (PAF) and persistent AF (PsAF) to investigate the development stages of AF. Typically, classification based on intra-operative epicardial measurements is done using features like conduction block (CB) and continuous conduction delay and block (cCDCB). Looking at Fig. 2.9, let Δ be the difference between local activation times of two adjacent cells. CB is defined as $\Delta \geq 12$ms, and CD is defined as $6 < \Delta < 12$ms. When CB reaches CD (or vice versa), the resulting line is referred to as cCDCB. However, these parameters do not clearly differentiate PAF and PsAF in sinus rhythm [12, 13]. Van der Does et al. showed that among all locations shown in Fig. 6.1, only at Bachmann's bundle (BB) there is a higher number of cCDCB line (p-value=0.040) [12]. However, the CB and cCDCB rely on an estimate of the local activation time (LAT). On the other hand, from the potential morphological viewpoint, Ye et al. demonstrated that the R/S ratio of single potentials (SPs) might be a useful characteristic for investigating the development stages of AF [14]. Therefore, we propose in this chapter a complimentary feature, related to the morphology of the signal, based on the underlying idea that AF progression can be related to variations in the atrial potential waveforms (APW).

7

7.2. METHODOLOGY

7.2.1. DATA AND PRE-PROCESSING

In this study, patients with normal sinus rhythm (NSR) who had a history of PAF or PsAF were included. We used multi-site high-resolution electrograms (EGMs) measured during open-heart surgery, at a sample rate of 1 kHz. The EGM data was collected at the Erasmus Medical Center (EMC). One ECG is measured simultaneously with the EGMs (188 electrodes) to detect the R peak location for heartbeat segmentation. Using a wavelet-based ECG delineator technique [103], we segmented the atrial activity of each EGM to concentrate on the atrial activity (AA). We used a fixed window with a length of 260 ms, between 320 ms and 60 ms, before the R peak. We excluded the electrically atrial silent patients or beats in the pre-screening step. We used 3-6 beats per patient from 11 PAF patients and 11 PsAF patients from three atrial regions. Altogether we included 132 beats from PAF patients and 161 beats from PsAF patients. More details on the mapping scheme and atrial regions are explained in [13].

7.2.2. SIGNAL MODEL

We have seen in Chapter 2 that the electrograms at the epicardial level can be modeled by the weighted summation of the transmembrane current shown in Eq.

2.2. Then, in Chapter 5, we developed a model where the normalized second singular value analysis can detect the degree of the spatial variation of atrial activity. In Chapter 5, we analyzed different scenarios that could increase the rank of the data matrix. This chapter focuses on a specific case where the patient is in a sinus rhythm. For simplification, we summarize our method explained in Chapter 5 and mention the necessary equations related to the SR scenario. Afterward, in Section 7.2.3, we extract features that are able to distinguish between PAF and PsAF.

The heart's electrical activity is initiated by the sinoatrial node and propagates across the atrium. We assume that in SR, all cells generate the same action potential. In that case, each electrode measures the attenuated-delayed version of the same reference AA. For the mth electrode this can be modelled as

$$y_m(t) = a_m s(t) * \delta(t - \tau_m) \tag{7.1}$$

where $s(t)$ is the reference AA, a_m models the positive real attenuation and $\delta(t-\tau_m)$ is the delay of the AA at electrode m compared to the reference AA, and $*$ is the convolution operator. In the frequency domain, Eq. (7.1) can be written as

$$\tilde{y}_m(\omega) = \int_{-\infty}^{+\infty} y_m(t) e^{-j\omega t} dt = a_m \tilde{s}(\omega) e^{-j\omega\tau_m} \tag{7.2}$$

where $\tilde{(\cdot)}$ denotes the frequency domain and we take N samples in frequency domain. The matrix $\tilde{\boldsymbol{Y}} \in \mathbb{C}^{M\times N}$ is constructed by stacking all the AAs for all electrodes and frequencies, where $m \in \{1,2,\cdots,M\}$ is the number of electrodes and $\omega \in \{\omega_1,\omega_2,\cdots,\omega_N\}$ denotes the angular frequency samples. Let us denote the absolute value of $\tilde{y}_m$ by

$$|\tilde{y}_m| = a_m |\tilde{s}| \tag{7.3}$$

then we define $\boldsymbol{B} \in \mathbb{C}_{\rho}^{M\times N}$ as a matrix with the element-wise absolute values of $\tilde{\boldsymbol{y}}_{\boldsymbol{m}} = [\tilde{y}_m(1), \tilde{y}_m(2), \cdots, \tilde{y}_m(N)]$, where ρ is the rank of matrix $\boldsymbol{B}$. In the case that the AA shows little variation, i.e., the action potentials are the same up to a delay, each electrode only measures the AA from the atrial site beneath it, and the propagation follows a flat wavefront, $\boldsymbol{B}$ is a low-rank matrix. In case of more complex underlying physiology - such as differences in AP morphology, abnormal wavefront propagation, simultaneous presence of multiple action potentials morphologies, and conduction blocks- the data matrix has a higher rank, and the AA will be different on some electrodes and the rank of $\boldsymbol{B}$ will be higher. Thus, when there is variation across the atrial regions resulting in $\rho \leq M$ different APWs, $\boldsymbol{B}$ will be a rank-ρ matrix. In this work, we assume that there are a limited number of different APWs. Therefore, $\boldsymbol{B}$ is a low-rank matrix and we can decompose it into a sum of rank-1 matrices. Using

the singular value decomposition (SVD), as seen in Eq. 5.4, matrix $\boldsymbol{B}$ is factorized as

$$\boldsymbol{B} = \boldsymbol{U}\boldsymbol{\Sigma}\boldsymbol{V}^H = \boldsymbol{U} \left[\begin{array}{ccc|ccc} \sigma_1 & 0 & \cdots & & \cdots & 0 \\ 0 & \sigma_2 & & & & \\ \vdots & & \ddots & & & \\ & & & \sigma_\rho & & \\ \hline & & & 0 & & \\ \vdots & & & & \ddots & \\ 0 & & & & & 0 \end{array}\right] \boldsymbol{V}^H \tag{7.4}$$

where $\boldsymbol{U}$ and $\boldsymbol{V}$ are orthogonal matrices, $\boldsymbol{\Sigma}$ is a non-negative diagonal matrix that contains the singular values of matrix $\boldsymbol{B}$ in a descending order. The rank is determined by the number of non-zero singular values of $\boldsymbol{B}$. However, in practice, the measurements are rather noisy and we need to divide the data matrix into signal subspace and noise subspace and determine the rank of the signal subspace. Given ρ, we can truncate the SVD to its first ρ terms and estimate the least square optimal $\boldsymbol{B}$ matrix that is

$$\hat{\boldsymbol{B}} = \boldsymbol{U}_{\mathscr{R}}\boldsymbol{\Sigma}_{\boldsymbol{\rho}\times\boldsymbol{\rho}}\boldsymbol{V}_{\mathscr{R}}^{\boldsymbol{H}} \tag{7.5}$$

where matrices $\boldsymbol{U}_{\mathscr{R}}$ and $\boldsymbol{V}_{\mathscr{R}}$ are the range spaces of $\boldsymbol{U}$ and $\boldsymbol{V}$, respectively, and $\boldsymbol{\Sigma}_{\boldsymbol{\rho}\times\boldsymbol{\rho}}$ is the truncated version of $\boldsymbol{\Sigma}$ to its first ρ singular values . The rank of $\boldsymbol{B}$ thus directly says something about the variation in AA and thus about the severity of AF. However, rank estimation with noisy and limited data records is rather challenging. Therefore, we propose two rank-related features that can be used to discriminate between PAF and PsAF.

7

7.2.3. PROPOSED FEATURES

We can measure the amount of energy in the matrix captured by each singular value by computing the norm of the rank-1 reconstruction divided by the norm of the whole data matrix. This ratio shows the importance of each singular value in the reconstruction. Thus, we propose feature I_1 based on the overall energy in the matrix captured by the first ρ singular values such that these first ρ singular values capture about 80% data energy in the matrix. We choose the energy in the matrix threshold of 80%, as this value achieved the highest classification accuracy on our dataset. Feature I_1 is then given by

$$I_1 = \arg\min_{\rho_1} \left| \frac{\sum_{i=1}^{\rho_1} \left|\left| \boldsymbol{u}_i \sigma_i \boldsymbol{v}_i^H \right|\right|^2}{\sum_{j=1}^{M} \left|\left| \boldsymbol{u}_j \sigma_j \boldsymbol{v}_j^H \right|\right|^2} - 0.8 \right| = \arg\min_{\rho_1} \left| \frac{\sum_{i=1}^{\rho_1} \sigma_i^2}{\sum_{j=1}^{M} \sigma_j^2} - 0.8 \right| \tag{7.6}$$

where $\boldsymbol{u}_i$ and $\boldsymbol{v}_i$ are the ith left and right singular vectors of $\boldsymbol{B}$. The higher I_1, the more diverse the atrial potential morphologies in the $\boldsymbol{B}$ matrix. Note that $\boldsymbol{B}$ matrix contains the absolute frequency spectrum of the EGMs measured at each electrode.

With the second feature, we focus on the relative importance of the singular values in the data matrix reconstruction. We define the ratio between the consecutive singular values σ_i and σ_{i+1} as

$$\varrho_i = \frac{\sigma_i}{\sigma_{i+1}}. \tag{7.7}$$

In Chapter 5, we only considered normalized second singular value, which is basically the inverse of ϱ_1. We suggested that the normalized second singular value could be an indicator to distinguish between SR and AF. Here, we suggest a larger number of ϱ_1 to be taken into account to differentiate different types of AF. Our motivation for looking at a higher number of ratios is that when there is variation in the atrial potential morphology due to any of the reasons, such as differences in AP morphology, abnormal wavefront propagation, simultaneous presence of multiple action potentials morphologies, and conduction blocks, the rank of the data matrix is higher than 1. Therefore, more than one singular value ratio could be used to extract the contributing factors in distinguishing different severity of the arrhythmia.

The rate of change as a function of i in the ϱ ratio is related to the relative importance of the singular values. It means that when the rate of change is low, increasing the rank for the reconstruction will not change the overall energy in the matrix of the data considerably. Therefore, the singular value can be considered to belong to the noise subspace. In Fig 7.1, the ϱ ratio is shown. The ϱ ratio for PAF patients shows a monotonic descending pattern but not in PsAF for the first components. Instead, there is a ratio increase on the third ratio (σ_3 to σ_4) demonstrating that the relative importance of σ_3 is much higher than that of σ_4. Moreover, looking at the ϱ ratios from the third ratio onward, PAF patients and PsAF patients show the same pattern with different rates of change. Taking these two points into account, we propose to take the first three singular value ratios (ϱ_1,ϱ_2 and ϱ_3) as features to extract the dominant components. Furthermore, to quantify the rate of change of ϱ_i as a function of i, we propose a feature that captures the

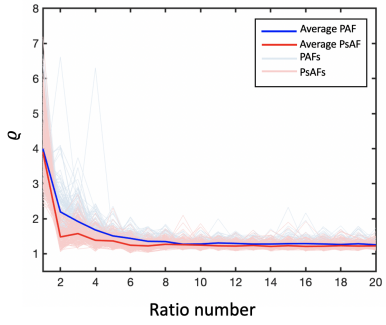

Figure 7.1: The average of the first 20 singular value ratios across all patients and all beats in PAF and PsAF

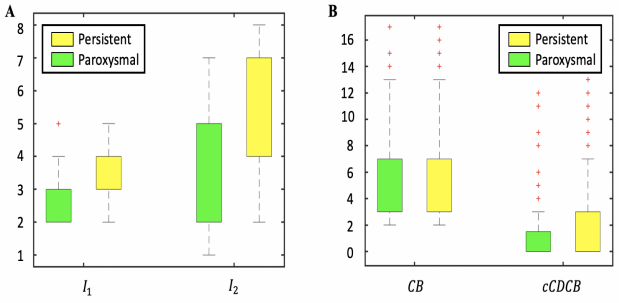

Figure 7.2: Box plots of the features, A) proposed features, B) state-of-the-art features.

bending point around the plateau as

$$I_2 = \arg\min_i \quad \left|\left(\left|\log\left(\varrho_{i+1}\right) - \log\left(\varrho_i\right)\right| - \epsilon\right)\right| \\ \text{s.t.} \quad 1 \leq \varrho_{i+1} \leq 1.5. \tag{7.8}$$

where ϵ was set to 0.1. The condition in Eq. 7.8 is set to identify the index near the plateau (i.e., 1), preventing early stopping on indexes with a high ϱ_i ratio and low rate of change. Similarly to the energy threshold parameter, these parameters were optimized based on the whole dataset in order to achieve maximal accuracy. Using log operator leads to I_2 approximating the second derivative between the consecutive singular values in the log domain. Indeed, a higher I_2 demonstrates the higher rate of change in the ϱ ratio which shows a higher number of important subspaces, i.e higher number of different APWs in the signal subspace.

Table 7.1: The performance of the SVM and RF classifiers on the features

Features \ Classifiers	RF	SVM
CB, cCDCB	57.02	58.34
$\boldsymbol{I_1}$	70.39	69.51
$\boldsymbol{I_2}$	74.52	74.26
$\boldsymbol{I_2, \varrho_1, \varrho_2, \varrho_3}$	76.21	75.94
$\boldsymbol{I_1, I_2, \varrho_1, \varrho_2, \varrho_3}$	78.42	77.63

7.3. RESULTS

This section presents a comparison of the performance of the proposed features with the reference features (CB and cCDCB). From a total of 293 heartbeats, we used the five proposed features, namely $I_1, I_2, \varrho_1, \varrho_2, \varrho_3$. Fig 7.2.A shows the box plots of

the proposed I_1 and I_2 features. Comparing I_1 and I_2 between PAF and PsAF, I_1 and I_2 are larger for PsAF than for PAF. It shows that a higher variation of APWs across the atrial regions is present in PsAF than in PAF. We compared the classification performance of the proposed features with the electropathological characteristics based on the CB. These parameters are calculated based on the LAT. The LAT is defined as the steepest deflection of the electrogram. A CB is defined as ΔLAT of adjacent electrodes ≥ 12ms. Comparing CB between PAF and PsAF in Fig 7.2.B, there is no considerable difference between these two groups. Moreover, we use two classifiers to evaluate the performance of the proposed features. First, a support vector machine (SVM) with radial basis function (RBF) kernel function and kernel parameter $\sigma = 1.5$ has been employed. The parameter has been chosen empirically based on our dataset. Second, a random forest (RF), an ensemble method, has been employed with a bagged ensemble of 30 classification trees. For validation, we used a 5-fold cross-validation approach on 293 heartbeats. Table 7.1(green rows) shows the performance of the classifiers on the proposed features. To investigate the importance of each feature, we trained the classifiers using features separately. Using all the proposed features (i.e., $I_1, I_2, \varrho_1, \varrho_2, \varrho_3$), we achieved 78.42% accuracy with the RF classifier, while CB and cCDCB could reach an accuracy of 58.34%. The proposed features improve the classification accuracy between PAF and PsAF. Furthermore, using all the proposed features, RF slightly outperforms SVM in PAF and PsAF classification.

7.4. DISCUSSION

This chapter proposes rank-related features to discriminate between PAF and PsAF. Rank estimation on the real dataset is challenging due to many reasons. Measured noise on the real data is the most important reason for misdetection in the rank estimation. The noise can affect the underlying structure of the data, posing challenges for rank estimation. The rank estimation problem has been addressed in many studies. Minimum description length (MDL) [135] and Aikaike's information criterion (AIC) [136] are two well-known methods in this context. These techniques, however, assume that the variance of the sensor self-noise for all sensors is the same, which is not the case in our database. Hence, in this study, rather than focusing on rank estimation, we concentrated on rank-related features aiming to distinguish between two types of atrial fibrillation. These features capture the spatial variation of atrial activity by using the morphology of the atrial potentials. Compared with the conductivity-based parameters, i.e., CB and cCDCB, van der Does et al. and Lanters et al. showed that in patients with a history of paroxysmal or persistent AF, there is no significant difference between these parameters during sinus rhythm [12, 13]. Looking at Table 7.1, the proposed features outperformed the conductivity-based parameters in the classification between paroxysmal and persistent AF.

The conductivity-based parameters are based on the local activation time estimation, which becomes challenging in the case of atrial potential fractionation. On the other hand, van Schie et al. and Ye et al. focused on the morphology of the atrial potentials and proposed the R/S ratio of the single potentials (SPs)

as valuable indicators for the severity detection of atrial fibrillation [14, 15]. Our morphological features are in line with the R/S ratio of the SPs and can extend this indicator to more challenging cases with double potentials and fractionations. Our proposed features could capture differences in AP morphology, abnormal wavefront propagation, the simultaneous presence of multiple action potential morphologies, and conduction blocks leading to AF.

Note that a few parameters that were used to calculate our features, such as the energy in the matrix threshold in Eq. (7.6), were optimized on the full available dataset. Future work should investigate whether our parameter settings generalize well to an independent dataset and, hence, can maintain classification accuracy.

7.5. CONCLUSION

In this chapter, we demonstrated one specific application of the method developed in Chapter 5. More specifically, we tested whether the proposed method is suitable for distinguishing patients with PAF or PsAF, using intra-operative EGMs during the sinus rhythm. We quantified the degree of electropathology using features related to the rank of the matrix containing the absolute frequency spectrum of the EGMs measured at each electrode. Feeding an RF classifier with the proposed features, we achieved 78.42% accuracy for the classification of PAF versus PsAF.

8

CONCLUSIONS AND FUTURE WORK

In this concluding chapter, we revisit the research questions introduced in Chapter 1, presenting our answers to these pivotal questions. We then explain the limitations of our study. Finally, we provide our suggestions for improvements in future studies, providing a pathway for further refinement and advancement in the field.

8.1. CONCLUSION

This thesis's main purpose was to improve the severity detection of atrial fibrillation, which we have addressed by answering three main questions. For this purpose, we have started with non-invasive measurements, i.e., multi-lead ECGs. Therefore, we investigated whether the severity of AF is detectable from the body surface measurements. This severity detection is helpful in monitoring the evolution of this arrhythmia from short-lasting AF to long-lasting AF. The extracted features are able to show the progression of the disease. However, due to the low-resolution measurements, variation of the electrical activity across the tissue can not be fully captured. Therefore, we went deeper from the surface of the body to the surface of the heart to have access to the high-resolution epicardial measurement, leading to deeper analysis of the electrical activity in the heart. Here, we developed a tool which is able to explain the atrial potential variations, areas of double potentials, the simultaneous presence of multiple AP morphologies, and conduction blocks. Using this tool, we proposed a marker based on the singular value decomposition of the data matrix, which is able to find these areas of interest using epicardial measurements. Moreover, we have shown that this marker is able to differentiate between SR and AF using both epicardial and body surface measurements. In the final step, we have demonstrated another application of the proposed method in the clinical environment where differentiating between different stages of AF during SR is challenging.

In the following sections, we subdivide the conclusion based on the initial research questions in Section 1.2, summarize our response to these questions, and highlight the key findings.

8.1.1. SEVERITY DETECTION OF ATRIAL FIBRILLATION USING MULTI-LEAD ECG

We started researching the characteristics of AF by monitoring the progression of AF from the mild stage to the more severe stage using multi-lead ECG measurements. Several studies have been done on the classification between SR and AF. However, due to its complications, the severity detection of AF is not well-addressed in the literature. Therefore, the first research question is:

Q1. Can we distinguish different stages of AF progression using multi-lead ECG measurements?

We subdivided this question into two questions and addressed them in Chapter 3 and Chapter 4.

A1. In the severity detection of AF, the key point is determining the time episode for the classification. Therefore, we have started from a general framework where the multi-lead ECG contains both SR and AF episodes. For differentiating between two stages of AF, namely paroxysmal and persistent AF, we developed a method discussed in Chapter 3, based on tensor decomposition, focusing on the morphological differences between different stages of AF. We then moved to the more complex case, excluding the SR episodes and only concentrating on the AF episode. On AF episodes, severity detection is not possible for cardiologists by visual inspection of the ECG. In Chapter 4, based on the nature of AF, we proposed three groups of features, namely, rhythm-based features, vectorcardiogram-based features, and frequency-based features, to capture both rhythmic and morphological differences from the multi-lead ECGs. Our findings showed that these features are discriminative between different stages of AF progression using multi-lead ECG. However, due to the low-resolution recordings (i.e., multi-lead ECG), the analysis of the electrical activity in the heart, leading to AF, could not be gained from these sub-sampled recordings.

8.1.2. A SINGULAR-VALUE-BASED MARKER FOR THE DETECTION OF ATRIAL FIBRILLATION

The analysis of wavefront propagation and areas of conduction blocks could be informative to explain the chaotic pattern observed in the ECG (see Fig. 4.5 and Section 4.2.4) and could help in AF severity detection. Therefore, we raised a question as :

Q2. Can we develop a simple and practical method to effectively capture the differences in atrial potential morphology or abnormal wavefront propagation, thereby enabling the identification of electropathological areas specific to AF?

A2. We have shown in Chapter 5 that we can develop an interpretable tool where the differences in AP morphology, abnormal wavefront propagation, and conduction blocks can be detected from it. We also posed two subsequent questions based on the developed signal model as:

Q2.1. Can we propose discriminative features based on the model to effectively detect electropathological regions on the epicardial measurements?

A2.1. We have shown in Chapter 5 that electropathological regions could

be described by changes in the data matrix's singular values constructed by the epicardial electrograms. We also introduced a location-dependent map called σ_2 map that is able to indicate the abnormal morphologies, inhomogeneities, and blocks in the tissue. Furthermore, the normalized σ_2 value has been shown as a valuable feature to capture the variation in the AP morphology or abnormal wavefront propagation, resulting in discrimination between SR and AF.

We then posed the second sub-question, related to the simultaneous epicardial and body surface potential measurements as

Q2.2. Can we use the same features to distinguish between SR and AF using body surface potentials?

A2.2. We have shown in Chapter 6 that the normalized second singular value of the data matrix constructed by the body surface potentials can be used as an indicator to classify AF. Using the same marker extracted from both the epicardial electrograms and the body surface potential measurements opens the room for developing more practical methods for detecting AF severity and unraveling AF electropathology non-invasively.

8.1.3. SEVERITY DETECTION OF ATRIAL FIBRILLATION DURING SINUS RHYTHM

We developed a model in Chapter 5 that can be used to find the electropathological regions in the tissue leading to AF. However, when attempting to assess the severity of AF using epicardial electrograms, the situation can get more complicated, especially if the patient is experiencing a sinus rhythm episode but has a history of AF in varying stages (such as paroxysmal or persistent). In other words, in patients with a history of AF who are currently in sinus rhythm, the ECG shows a normal sinus rhythm. At the same time, there are some regions in the tissue where the epicardial electrodes measure abnormal electrical activities. Therefore, in the final part, we wanted to demonstrate the proposed method's broad applicability and highlight its usefulness in addressing a more complex clinical challenge. Through this demonstration, we aimed to highlight the method's adaptability and effectiveness in clinical scenarios, thus enhancing its potential influence and significance. We have shown in Chapter 5 that one extracted feature from the model is the normalized second singular value. Therefore, we posed a question as:

Q3. Can we derive relevant features based on the proposed method to accurately assess the severity of AF during SR?

A3. We have shown in Chapter 7 that the variation of atrial potential waveforms can be detected by two features based on the singular value decomposition of the data matrix using the absolute frequency spectrum of the epicardial electrograms.

The features that have been extracted show a clear relationship with the rank of the data matrix, which implies potential applicability to other contexts with rank-related characteristics. Note that some parameters are empirically set based on the dataset. It is important to undertake thorough parameter tuning tailored to the specific dataset and intended applications to ensure optimal performance and relevance.

8.2. RELATION BETWEEN ECG-BASED AND EGM-BASED FEATURES

This thesis mainly focused on the severity detection of atrial fibrillation using multi-lead ECGs and high-resolution EGMs. As a closing remark, it is valuable to see how these severity detections could be related to each other. This connection is shown in Fig. 8.1. In Chapter 5, we have shown that double potentials, abnormal wavefront propagation, simultaneous presence of multiple action potentials morphologies, and conduction blocks could increase the rank of the data matrix leading to AF. In Chapter 7, we have seen that as the severity increases from mild (e.g., PAF) to severe (e.g., PsAF), more components are needed to reconstruct the total energy in the data matrix derived from the EGMs. We can relate the characteristics derived from the EGM measurements to those from the ECG measurements.

In Chapter 4, we have seen that multiple frequencies are involved in characterizing ECG signals. As the severity of AF increases from mild (e.g., *de novo* POAF) to severe (e.g., PsAF), the number of frequency components also increases (shown in Fig. 4.11). The increase in the number of frequency components caused by AF could be equivalent to multiple wavefronts or variation in the action potential on the electrogram level. Furthermore, the chaotic pattern in the vectorcardiogram is due to the ECG's fibrillatory waves, which is based on the uncoordinated atrial activity. We hypothesize that the chaotic pattern could be due to the simultaneous presence of multiple action potential morphologies or wavefront directions that are not aligned, causing a chaotic pattern on the ECG signals. Note that this hypothesis needs more investigation on clinical data. Finally, the order of the AR model introduced in Section 4.2.3 increases with the severity of AF. This index could be related to the increase in the σ_2 value in Chapter 5 and the increase in the rank of the data matrix in Chapter 7 due to the abnormal wavefront propagation, the simultaneous presence of multiple action potential morphologies, and conduction blocks.

8.3. LIMITATIONS AND FUTURE WORK

In this section, we outline some of the restrictions that appeared during our research, providing insights into the areas where limitations were experienced. We also offer suggestions for potential improvements that would encourage ongoing development of the research framework. We also point out some unanswered questions that have come up as a result of our research, opening up new lines of inquiry and discovery.

In Chapter 4 and Chapter 6, we proposed a feature-engineering framework for AF severity detection. However, our ability to thoroughly fine-tune and validate the method on an independent dataset was constrained due to limited data availability. Consequently, our parameter tuning process remains tailored to our specific dataset, which, in turn, necessitates further adjustments of parameter tuning when applied to different datasets.

An additional limitation resulting from the insufficiency of available data is the impossibility of comprehensively comparing our proposed methodology with deep-learning-based methods. While our primary goal was to develop interpretable

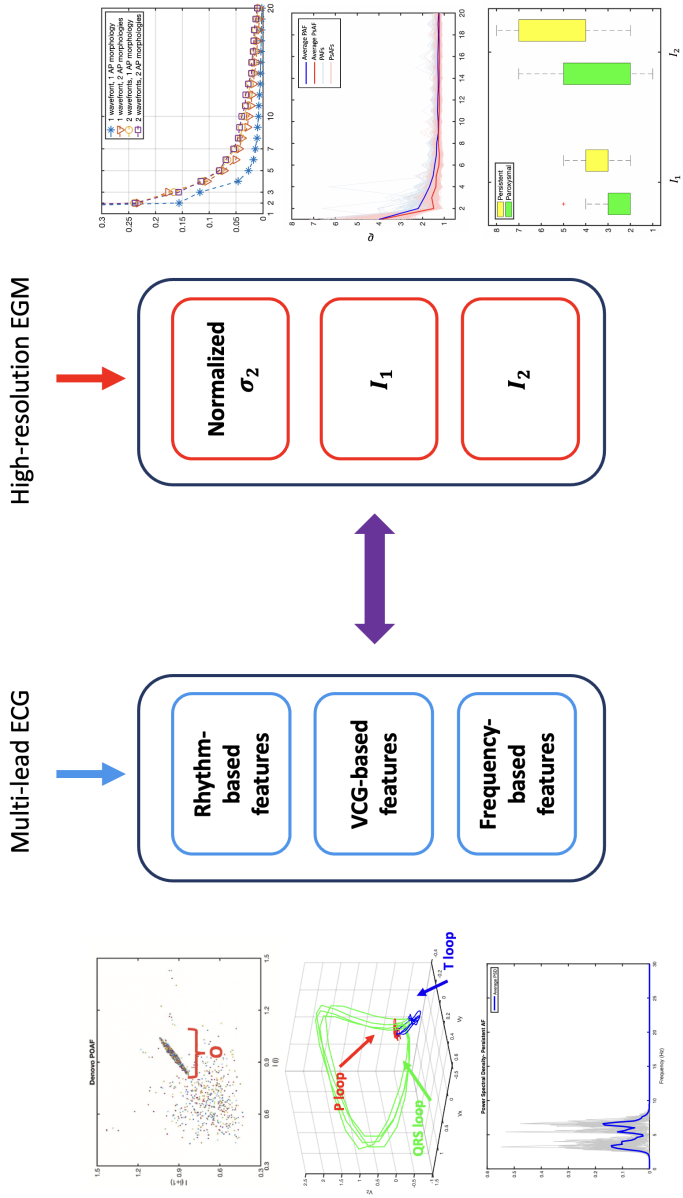

Figure 8.1: Relation between the ECG-based findings and EGM-based findings

features to distinguish between different stages of AF, comparing a handcrafted approach with a deep learning approach could yield valuable insights for

methodological evaluation. More specifically, integrating processed data with a deep learning approach could improve the accuracy of AF severity detection methods.

In Chapter 4, we proposed vectorcardiogram-based features using multi-lead ECGs. However, ECG recording is related to body mass index (BMI). To the best of our knowledge, the effect of BMI on the ECG signal is not quantified in the literature. Therefore, more research in this area will be helpful to compare the surface of the QRS loops in the 3D VCG more effectively, leading to more accurate features.

In Chapter 5, we focused on the morphology of the electrograms to detect the spatial variation of atrial potential morphology. For this purpose, we discard the phase information of the measured electrograms. However, discarding the phase leads to suppressing half of the information hidden in the epicardial/body surface measurements, which could be used as a complementary tool. Our method's independence from the LAT estimation is its main advantage. However, the approach loses temporal information, making it incomparable to activation maps. Therefore, integrating the σ_2 map with the activation map could help unveil the tissue's electropathological parameters more effectively.

Furthermore, in Chapter 5 and Chapter 7, we stacked the absolute frequency spectrum of the epicardial/body surface potentials in a matrix. However, this stacking approach leads to losing the spatial relationship between the electrodes. This problem is subtle using a subset of the electrode array. However, it is more pronounced using the full electrode array measurements, where electrode placements and the connections between the electrodes become more critical. Therefore, constructing a 3-order tensor could also help to take the spatial information into account. In this way, the first and second dimensions of the tensor would be the coordination of the electrodes (in comparison with a reference electrode), and the third dimension would be the absolute frequency spectrum of the epicardial/body surface potentials. Using a tensor decomposition, such as multilinear singular value decomposition (MLSVD) [137], could lead to decomposing the original matrix into the components where the spatial connection between electrodes is taken into account, leading to further improvement in the severity detection of AF.

In addition to the potential improvements in the methodology of the developed AF severity detection methods, there are a few steps that must be undertaken to make the developed methods clinically applicable. Firstly, in this thesis, the parameters of the classifiers, such as the kernel parameter in the SVM and the number of classification trees in the RF, are chosen empirically based on our dataset. To make the methods developed in Chapter 4 and Chapter 7 more appropriate for the clinical environment, it is recommended to tune these parameters based on a more extensive and diverse dataset from different medical centers. Furthermore, as can be seen in Fig. 6.4, the threshold for distinguishing between SR and AF varies between different mapping locations. Therefore, finding a location-dependent threshold for the classification between SR and AF or even different severities of AF based on a larger and independent dataset could facilitate using the developed method in Chapter 5 in the clinical environment. Moreover, the designed vest in Chapter 6 is used in the experimental setup in combination with the high-resolution epicardial measurement. If a built-in recording setup is designed to measure the real-time

BSP data, this vest could be used as a valuable diagnostic tool in the clinical environment. Finally, we have seen that the methods developed in Chapter 5 and Chapter 6 are tested with electrograms recorded from a rectangular electrode array. Here, one can use catheter electrodes and apply the developed method in Chapter 5 to localize the abnormal regions as potential target sites of ablation therapy. The normalized second singular values of the sub-matrices (e.g., catheter electrodes) could be used to find the target sites.

BIBLIOGRAPHY

[1] D. M. Lloyd-Jones, T. J. Wang, E. P. Leip, M. G. Larson, D. Levy, R. S. Vasan, R. B. D'Agostino, J. M. Massaro, A. Beiser, P. A. Wolf, *et al.* "Lifetime risk for development of atrial fibrillation: the Framingham Heart Study". In: *Circulation* 110.9 (2004), pp. 1042–1046.

[2] L. Sörnmo and P. Laguna. *Bioelectrical signal processing in cardiac and neurological applications*. Vol. 8. Academic press, 2005.

[3] A. M. Katz. *Physiology of the Heart*. Lippincott Williams & Wilkins, 2010.

[4] S. Nattel. "New ideas about atrial fibrillation 50 years on". In: *Nature* 415.6868 (2002), pp. 219–226.

[5] M. Allessie, J. Ausma, and U. Schotten. "Electrical, contractile and structural remodeling during atrial fibrillation". In: *Cardiovascular research* 54.2 (2002), pp. 230–246.

[6] A. Yaksh, C. Kik, P. Knops, J. Roos-Hesselink, A. Bogers, F. Zijlstra, M. Allessie, and N. De Groot. "Atrial fibrillation: to map or not to map?" In: *Netherlands Heart Journal* 22 (2014), pp. 259–266.

[7] M. Lewis, D. Parker, C. Weston, and M. Bowes. "Screening for atrial fibrillation: sensitivity and specificity of a new methodology". In: *British Journal of General Practice* 61.582 (2011), pp. 38–39.

[8] R. Alcaraz and J. J. Rieta. "Sample entropy of the main atrial wave predicts spontaneous termination of paroxysmal atrial fibrillation". In: *Medical engineering & physics* 31.8 (2009), pp. 917–922.

[9] F. Chiarugi, M. Varanini, F. Cantini, F. Conforti, and G. Vrouchos. "Noninvasive ECG as a tool for predicting termination of paroxysmal atrial fibrillation". In: *IEEE Transactions on Biomedical Engineering* 54.8 (2007), pp. 1399–1406.

[10] R. Alcaraz and J. J. Rieta. "The application of nonlinear metrics to assess organization differences in short recordings of paroxysmal and persistent atrial fibrillation". In: *Physiological measurement* 31.1 (2009), p. 115.

[11] S. Nattel, B. Burstein, and D. Dobrev. "Atrial remodeling and atrial fibrillation: mechanisms and implications". In: *Circulation: Arrhythmia and Electrophysiology* 1.1 (2008), pp. 62–73.

[12] W. F. van der Does et al. "Conduction disorders during sinus rhythm in relation to atrial fibrillation persistence". In: *Journal of Clinical Medicine* 10.13 (2021), p. 2846.

[13] E. A. Lanters et al. "Spatial distribution of conduction disorders during sinus rhythm". In: *International Journal of Cardiology* 249 (2017), pp. 220–225.

[14] Z. Ye, M. S. van Schie, and N. M. de Groot. “Signal fingerprinting as a novel diagnostic tool to identify conduction inhomogeneity”. In: *Frontiers in Physiology* 12 (2021), p. 652128.

[15] M. S. van Schie et al. “Classification of sinus rhythm single potential morphology in patients with mitral valve disease”. In: *EP Europace* 22.10 (2020), pp. 1509–1519.

[16] M. K. Steven. “Fundamentals of statistical signal processing”. In: *PTR Prentice-Hall, Englewood Cliffs, NJ* 10.151045 (1993), p. 148.

[17] J. E. Hall and M. E. Hall. *Guyton and Hall textbook of medical physiology e-Book*. Elsevier Health Sciences, 2020.

[18] R. O. Bonow, D. L. Mann, D. P. Zipes, and P. Libby. *Braunwald's heart disease e-book: A textbook of cardiovascular medicine*. Elsevier Health Sciences, 2011.

[19] P. A. Iaizzo. *Handbook of cardiac anatomy, physiology, and devices*. Springer Science & Business Media, 2010.

[20] ECGwaves. *Cardiac electrophysiology: Membrane potential, action potential, automaticity, and electrical vectors*. URL: https://ecgwaves.com/topic/cardiac-electrophysiology-ecg-action-potential-automaticity-vector/.

[21] ECGwaves. *ECG entrepretation: definition, criteria, and characteristics of normal ECG waves, intervals, durations and rhythm*. URL: https://ecgwaves.com/topic/ecg-normal-p-wave-qrs-complex-st-segment-t-wave-j-point/.

[22] F. Shaffer and J. P. Ginsberg. “An overview of heart rate variability metrics and norms”. In: *Frontiers in public health* (2017), p. 258.

[23] A. Bakhai, H. Darius, R. De Caterina, A. Smart, J.-Y. Le Heuzey, R. J. Schilling, J. L. Zamorano, M. Shah, P. Bramlage, and P. Kirchhof. “Characteristics and outcomes of atrial fibrillation patients with or without specific symptoms: results from the PREFER in AF registry”. In: *European Heart Journal–Quality of Care and Clinical Outcomes* 2.4 (2016), pp. 299–305.

[24] M. Streur, S. J. Ratcliffe, D. Callans, M. B. Shoemaker, and B. Riegel. “Atrial fibrillation symptom clusters and associated clinical characteristics and outcomes: A cross-sectional secondary data analysis”. In: *European Journal of Cardiovascular Nursing* 17.8 (2018), pp. 707–716.

[25] C. A. Sanoski. “Clinical, economic, and quality of life impact of atrial fibrillation”. In: *Journal of Managed Care Pharmacy* 15.6 Supp B (2009), pp. 4–9.

[26] S. Petrutiu, J. Ng, G. M. Nijm, H. Al-Angari, S. Swiryn, and A. V. Sahakian. “Atrial fibrillation and waveform characterization”. In: *IEEE engineering in medicine and biology magazine* 25.6 (2006), pp. 24–30.

[27] A. F. Members, V. Fuster, L. E. Rydén, D. S. Cannom, H. J. Crijns, A. B. Curtis, K. A. Ellenbogen, J. L. Halperin, J.-Y. Le Heuzey, G. N. Kay, *et al.* "Acc/aha/esc 2006 guidelines for the management of patients with atrial fibrillation–executive summary: A report of the american college of cardiology/american heart association task force on practice guidelines and the european society of cardiology committee for practice guidelines (writing committee to revise the 2001 guidelines for the management of patients with atrial fibrillation) developed in collaboration with the european heart rhythm association and the heart rhythm society". In: *European Heart Journal* 27.16 (2006), pp. 1979–2030.

[28] C. T. January, L. S. Wann, H. Calkins, L. Y. Chen, J. E. Cigarroa, J. C. Cleveland Jr, P. T. Ellinor, M. D. Ezekowitz, M. E. Field, K. L. Furie, *et al.* "2019 AHA/ACC/HRS focused update of the 2014 AHA/ACC/HRS guideline for the management of patients with atrial fibrillation: a report of the American College of Cardiology/American Heart Association Task Force on Clinical Practice Guidelines and the Heart Rhythm Society in collaboration with the Society of Thoracic Surgeons". In: *Circulation* 140.2 (2019), e125–e151.

[29] R. S. Wijesurendra and B. Casadei. "Mechanisms of atrial fibrillation". In: *Heart* 105.24 (2019), pp. 1860–1867.

[30] M. S. Guillem, A. M. Climent, M. Rodrigo, F. Fernández-Avilés, F. Atienza, and O. Berenfeld. "Presence and stability of rotors in atrial fibrillation: evidence and therapeutic implications". In: *Cardiovascular research* 109.4 (2016), pp. 480–492.

[31] G. Moe and J. Abildskov. "Atrial fibrillation as a self-sustaining arrhythmia independent of focal discharge". In: *American heart journal* 58.1 (1959), pp. 59–70.

[32] J. L. Cox, T. E. Canavan, R. B. Schuessler, M. E. Cain, B. D. Lindsay, C. Stone, P. K. Smith, P. B. Corr, and J. P. Boineau. "The surgical treatment of atrial fibrillation: II. Intraoperative electrophysiologic mapping and description of the electrophysiologic basis of atrial flutter and atrial fibrillation". In: *The Journal of thoracic and cardiovascular surgery* 101.3 (1991), pp. 406–426.

[33] G. K. Moe, W. C. Rheinboldt, and J. Abildskov. "A computer model of atrial fibrillation". In: *American heart journal* 67.2 (1964), pp. 200–220.

[34] G. K. Moe. "On the multiple wavelet hypothesis of atrial fibrillation". In: *Arch. Int. Pharmacodyn Theory* 140 (1962), pp. 183–188.

[35] N. de Groot, L. Van Der Does, A. Yaksh, E. Lanters, C. Teuwen, P. Knops, P. van de Woestijne, J. Bekkers, C. Kik, A. Bogers, *et al.* "Direct proof of endo-epicardial asynchrony of the atrial wall during atrial fibrillation in humans". In: *Circulation: Arrhythmia and Electrophysiology* 9.5 (2016), e003648.

[36] H. Moghaddasi, R. C. Hendriks, A.-J. van der Veen, N. M. de Groot, and B. Hunyadi. "Classification of De novo post-operative and persistent atrial fibrillation using multi-channel ECG recordings". In: *Computers in Biology and Medicine* 143 (2022), p. 105270.

[37] A. J. Walkey, S. K. Bashar, M. B. Hossain, E. Ding, D. Albuquerque, M. Winter, K. H. Chon, and D. D. McManus. “Development and validation of an automated algorithm to detect atrial fibrillation within stored intensive care unit continuous electrocardiographic data: observational study”. In: *JMIR cardio* 5.1 (2021), e18840.

[38] D. Marinucci, A. Sbrollini, I. Marcantoni, M. Morettini, C. A. Swenne, and L. Burattini. “Artificial neural network for atrial fibrillation identification in portable devices”. In: *Sensors* 20.12 (2020), p. 3570.

[39] Y. Yue, C. Chen, P. Liu, Y. Xing, and X. Zhou. “Automatic detection of short-term atrial fibrillation segments based on frequency slice wavelet transform and machine learning techniques”. In: *Sensors* 21.16 (2021), p. 5302.

[40] J. Wang, P. Wang, and S. Wang. “Automated detection of atrial fibrillation in ECG signals based on wavelet packet transform and correlation function of random process”. In: *Biomedical Signal Processing and Control* 55 (2020), p. 101662.

[41] I. H. Bruun, S. M. Hissabu, E. S. Poulsen, and S. Puthusserypady. “Automatic atrial fibrillation detection: A novel approach using discrete wavelet transform and heart rate variability”. In: *2017 39th Annual International Conference of the IEEE Engineering in Medicine and Biology Society (EMBC)*. IEEE. 2017, pp. 3981–3984.

[42] S. Mandal and N. Sinha. “Prediction of atrial fibrillation based on nonlinear modeling of heart rate variability signal and SVM classifier”. In: *Research on Biomedical Engineering* 37 (2021), pp. 725–736.

[43] M. Robnik-Šikonja and I. Kononenko. “Theoretical and empirical analysis of ReliefF and RReliefF”. In: *Machine learning* 53.1-2 (2003), pp. 23–69.

[44] J. Tang, S. Alelyani, and H. Liu. “Feature selection for classification: A review”. In: *Data classification: Algorithms and applications* (2014), p. 37.

[45] H. Liu, M. Zhou, and Q. Liu. “An embedded feature selection method for imbalanced data classification”. In: *IEEE/CAA Journal of Automatica Sinica* 6.3 (2019), pp. 703–715.

[46] C. Cortes and V. Vapnik. “Support-vector networks”. In: *Machine learning* 20 (1995), pp. 273–297.

[47] L. Breiman. “Random forests”. In: *Machine learning* 45 (2001), pp. 5–32.

[48] J. MacQueen *et al.* “Some methods for classification and analysis of multivariate observations”. In: *Proceedings of the fifth Berkeley symposium on mathematical statistics and probability*. Vol. 1. 14. Oakland, CA, USA. 1967, pp. 281–297.

[49] C. J. Watkins and P. Dayan. “Q-learning”. In: *Machine learning* 8 (1992), pp. 279–292.

[50] Y.-Y. Jo, Y. Cho, S. Y. Lee, J.-m. Kwon, K.-H. Kim, K.-H. Jeon, S. Cho, J. Park, and B.-H. Oh. “Explainable artificial intelligence to detect atrial fibrillation using electrocardiogram”. In: *International journal of cardiology* 328 (2021), pp. 104–110.

[51] X. Chen, Z. Cheng, S. Wang, G. Lu, G. Xv, Q. Liu, and X. Zhu. "Atrial fibrillation detection based on multi-feature extraction and convolutional neural network for processing ECG signals". In: *Computer Methods and Programs in Biomedicine* 202 (2021), p. 106009.

[52] A. Fabbri, M. Fantini, R. Wilders, and S. Severi. "Computational analysis of the human sinus node action potential: model development and effects of mutations". In: *The Journal of physiology* 595.7 (2017), pp. 2365–2396.

[53] M. Courtemanche, R. J. Ramirez, and S. Nattel. "Ionic mechanisms underlying human atrial action potential properties: insights from a mathematical model". In: *American Journal of Physiology-Heart and Circulatory Physiology* 275.1 (1998), H301–H321.

[54] C.-h. Luo and Y. Rudy. "A model of the ventricular cardiac action potential. Depolarization, repolarization, and their interaction." In: *Circulation research* 68.6 (1991), pp. 1501–1526.

[55] N. Virag, V. Jacquemet, C. Henriquez, S. Zozor, O. Blanc, J.-M. Vesin, E. Pruvot, and L. Kappenberger. "Study of atrial arrhythmias in a computer model based on magnetic resonance images of human atria". In: *Chaos: An Interdisciplinary Journal of Nonlinear Science* 12.3 (2002), pp. 754–763.

[56] A. Yaksh, L. J. van der Does, C. Kik, P. Knops, F. Oei, P. C. van de Woestijne, J. A. Bekkers, A. J. Bogers, M. A. Allessie, and N. de Groot. "A novel intra-operative, high-resolution atrial mapping approach". In: *Journal of Interventional Cardiac Electrophysiology* 44.3 (2015), pp. 221–225.

[57] S. Honarbakhsh, R. Schilling, M. Orini, R. Providencia, M. Finlay, E. Keating, P. Lambiase, A. Chow, M. Earley, S. Sporton, *et al.* "Left atrial scarring and conduction velocity dynamics: rate dependent conduction slowing predicts sites of localized reentrant atrial tachycardias". In: *International journal of cardiology* 278 (2019), pp. 114–119.

[58] Ö. N. Onak, T. Erenler, and Y. S. Dogrusoz. "A novel data-adaptive regression framework based on multivariate adaptive regression splines for electrocardiographic imaging". In: *IEEE Transactions on Biomedical Engineering* 69.2 (2021), pp. 963–974.

[59] C. Kik, E. M. Mouws, A. J. Bogers, and N. M. S. de Groot. "Intra-operative mapping of the atria: the first step towards individualization of atrial fibrillation therapy?" In: *Expert review of cardiovascular therapy* 15.7 (2017), pp. 537–545.

[60] D. Wallmann, D. Tüller, K. Wustmann, P. Meier, J. Isenegger, M. Arnold, H. P. Mattle, and E. Delacrétaz. "Frequent atrial premature beats predict paroxysmal atrial fibrillation in stroke patients: an opportunity for a new diagnostic strategy". In: *Stroke* 38.8 (2007), pp. 2292–2294.

[61] K. Jiang, C. Huang, S.-m. Ye, and H. Chen. "High accuracy in automatic detection of atrial fibrillation for Holter monitoring". In: *Journal of Zhejiang University SCIENCE B* 13 (2012), pp. 751–756.

[62] R. Alcaraz, F. Sandberg, L. Sörnmo, and J. J. Rieta. “Classification of paroxysmal and persistent atrial fibrillation in ambulatory ECG recordings”. In: *IEEE Transactions on Biomedical Engineering* 58.5 (2011), pp. 1441–1449.

[63] F. Rincón, P. R. Grassi, N. Khaled, D. Atienza, and D. Sciuto. “Automated real-time atrial fibrillation detection on a wearable wireless sensor platform”. In: *2012 Annual international conference of the IEEE engineering in medicine and biology society*. IEEE. 2012, pp. 2472–2475.

[64] S. Padhy and S. Dandapat. “Third-order tensor based analysis of multilead ECG for classification of myocardial infarction”. In: *Biomedical Signal Processing and Control* 31 (2017), pp. 71–78.

[65] S. Padhy and S. Dandapat. “Exploiting multi-lead electrocardiogram correlations using robust third-order tensor decomposition”. In: *Healthcare technology letters* 2.5 (2015), pp. 112–117.

[66] M. Boussé, G. Goovaerts, N. Vervliet, O. Debals, S. Van Huffel, and L. De Lathauwer. “Irregular heartbeat classification using Kronecker product equations”. In: *2017 39th Annual International Conference of the IEEE Engineering in Medicine and Biology Society (EMBC)*. IEEE. 2017, pp. 438–441.

[67] G. Goovaerts, C. Varon, B. Vandenberk, R. Willems, and S. Van Huffel. “Tensor-based detection of T wave alternans in multilead ECG signals”. In: *Computing in Cardiology 2014*. IEEE. 2014, pp. 185–188.

[68] S. Geirnaert, G. Goovaerts, S. Padhy, M. Boussé, L. De Lathauwer, and S. Van Huffel. “Tensor-based ECG signal processing applied to atrial fibrillation detection”. In: *2018 52nd Asilomar Conference on Signals, Systems, and Computers*. IEEE. 2018, pp. 799–805.

[69] G. F. Rosner, J. A. Reiffel, and K. Hickey. “The concept of “burden” in atrial fibrillation”. In: *Journal of Atrial Fibrillation* 4.5 (2012).

[70] I. Beraza and I. Romero. “Comparative study of algorithms for ECG segmentation”. In: *Biomedical Signal Processing and Control* 34 (2017), pp. 166–173.

[71] R. Bolton and L. Westphal. “Preliminary results in display and abnormality recognition of Hilbert transformed ecgs”. In: *Medical and Biological Engineering and Computing* 19 (1981), pp. 377–384.

[72] D. Benitez, P. Gaydecki, A. Zaidi, and A. Fitzpatrick. “The use of the Hilbert transform in ECG signal analysis”. In: *Computers in biology and medicine* 31.5 (2001), pp. 399–406.

[73] V. N. Varghees and K. Ramachandran. “A novel heart sound activity detection framework for automated heart sound analysis”. In: *Biomedical Signal Processing and Control* 13 (2014), pp. 174–188.

[74] M. Johansson. “The hilbert transform”. In: *Mathematics Master’s Thesis. Växjö University, Suecia. Disponible en internet: http://w3. msi. vxu. se/exarb/mj_ex. pdf, consultado el* 19 (1999).

[75] L. Muda, M. Begam, and I. Elamvazuthi. “Voice recognition algorithms using mel frequency cepstral coefficient (MFCC) and dynamic time warping (DTW) techniques”. In: *arXiv preprint arXiv:1003.4083* (2010).

[76] B. Hunyadi, P. Dupont, W. Van Paesschen, and S. Van Huffel. “Tensor decompositions and data fusion in epileptic electroencephalography and functional magnetic resonance imaging data”. In: *Wiley Interdisciplinary Reviews: Data Mining and Knowledge Discovery* 7.1 (2017), e1197.

[77] T. G. Kolda and B. W. Bader. “Tensor decompositions and applications”. In: *SIAM review* 51.3 (2009), pp. 455–500.

[78] J. B. Kruskal. “Three-way arrays: rank and uniqueness of trilinear decompositions, with application to arithmetic complexity and statistics”. In: *Linear algebra and its applications* 18.2 (1977), pp. 95–138.

[79] N. D. Sidiropoulos and R. Bro. “On the uniqueness of multilinear decomposition of N-way arrays”. In: *Journal of Chemometrics: A Journal of the Chemometrics Society* 14.3 (2000), pp. 229–239.

[80] L. S. Wann *et al.* “2011 ACCF/AHA/HRS focused update on the management of patients with atrial fibrillation”. In: *Journal of the American College of Cardiology* 57.2 (2011), pp. 223–242.

[81] E. Mansoor. “De novo atrial fibrillation post cardiac surgery: the Durban experience”. In: *Cardiovascular journal of Africa* 25.6 (2014), p. 282.

[82] R. W. Rho. “The management of atrial fibrillation after cardiac surgery”. In: *Heart* 95.5 (2009), pp. 422–429.

[83] J. Park, S. Lee, and M. Jeon. “Atrial fibrillation detection by heart rate variability in Poincare plot”. In: *Biomedical engineering online* 8.1 (2009), p. 38.

[84] J. Sepulveda-Suescun, J. Murillo-Escobar, R. Urda-Benitez, D. Orrego-Metaute, and A. Orozco-Duque. “Atrial fibrillation detection through heart rate variability using a machine learning approach and Poincare plot features”. In: *VII Latin American Congress on Biomedical Engineering CLAIB 2016, Bucaramanga, Santander, Colombia, October 26th-28th, 2016*. Springer. 2017, pp. 565–568.

[85] C. Huang, S. Ye, H. Chen, D. Li, F. He, and Y. Tu. “A novel method for detection of the transition between atrial fibrillation and sinus rhythm”. In: *IEEE Transactions on Biomedical Engineering* 58.4 (2010), pp. 1113–1119.

[86] D. E. Lake and J. R. Moorman. “Accurate estimation of entropy in very short physiological time series: the problem of atrial fibrillation detection in implanted ventricular devices”. In: *American Journal of Physiology-Heart and Circulatory Physiology* 300.1 (2011), H319–H325.

[87] D. Dharmaprani, L. Dykes, A. D. McGavigan, P. Kuklik, K. Pope, and A. N. Ganesan. “Information theory and atrial fibrillation (AF): a review”. In: *Frontiers in physiology* 9 (2018), p. 957.

[88] A. Mukherjee, A. D. Choudhury, S. Datta, C. Puri, R. Banerjee, R. Singh, A. Ukil, S. Bandyopadhyay, A. Pal, and S. Khandelwal. "Detection of atrial fibrillation and other abnormal rhythms from ECG using a multi-layer classifier architecture". In: *Physiological measurement* 40.5 (2019), p. 054006.

[89] S. K. Bashar, E. Ding, D. Albuquerque, M. Winter, S. Binici, A. J. Walkey, D. D. McManus, and K. H. Chon. "Atrial Fibrillation Detection in ICU Patients: A Pilot Study on MIMIC III Data". In: *2019 41st Annual International Conference of the IEEE Engineering in Medicine and Biology Society (EMBC)*. IEEE. 2019, pp. 298–301.

[90] J. Sacha. "Interaction between heart rate and heart rate variability". In: *Annals of Noninvasive Electrocardiology* 19.3 (2014), pp. 207–216.

[91] A. Kennedy, D. D. Finlay, D. Guldenring, R. R. Bond, K. Moran, and J. McLaughlin. "Automated detection of atrial fibrillation using RR intervals and multivariate-based classification". In: *Journal of electrocardiology* 49.6 (2016), pp. 871–876.

[92] S. K. Bashar, M. B. Hossain, E. Ding, A. J. Walkey, D. D. McManus, and K. H. Chon. "Atrial fibrillation detection during sepsis: study on MIMIC III ICU data". In: *IEEE Journal of Biomedical and Health Informatics* 24.11 (2020), pp. 3124–3135.

[93] S. Babaeizadeh, R. E. Gregg, E. D. Helfenbein, J. M. Lindauer, and S. H. Zhou. "Improvements in atrial fibrillation detection for real-time monitoring". In: *Journal of electrocardiology* 42.6 (2009), pp. 522–526.

[94] Y. Chen, X. Wang, Y. Jung, V. Abedi, R. Zand, M. Bikak, and M. Adibuzzaman. "Classification of short single-lead electrocardiograms (ECGs) for atrial fibrillation detection using piecewise linear spline and XGBoost". In: *Physiological measurement* 39.10 (2018), p. 104006.

[95] D. Lai, Y. Bu, Y. Su, X. Zhang, and C.-S. Ma. "Non-Standardized Patch-Based ECG Lead Together With Deep Learning Based Algorithm for Automatic Screening of Atrial Fibrillation". In: *IEEE Journal of Biomedical and Health Informatics* 24.6 (2020), pp. 1569–1578. DOI: 10.1109/JBHI.2020.2980454.

[96] I. H. Bruun, S. M. S. Hissabu, E. S. Poulsen, and S. Puthusserypady. "Automatic Atrial Fibrillation detection: A novel approach using discrete wavelet transform and heart rate variability". In: *2017 39th Annual International Conference of the IEEE Engineering in Medicine and Biology Society (EMBC)*. 2017, pp. 3981–3984. DOI: 10.1109/EMBC.2017.8037728.

[97] E. Essa and X. Xie. "An Ensemble of Deep Learning-Based Multi-Model for ECG Heartbeats Arrhythmia Classification". In: *IEEE Access* 9 (2021), pp. 103452–103464. DOI: 10.1109/ACCESS.2021.3098986.

[98] G. Hirsch, S. H. Jensen, E. S. Poulsen, and S. Puthusserypady. "Atrial fibrillation detection using heart rate variability and atrial activity: A hybrid approach". In: *Expert Systems with Applications* 169 (2021), p. 114452.

[99] N. Ortigosa, A. Galbis, C. Fernández, and Ó. Cano. "Gabor frames for classification of paroxysmal and persistent atrial fibrillation episodes". In: *Medical engineering & physics* 39 (2017), pp. 31–37.

[100] P. Kligfield *et al.* “Recommendations for the standardization and interpretation of the electrocardiogram: part I: the electrocardiogram and its technology”. In: *Journal of the American College of Cardiology* 49.10 (2007), pp. 1109–1127.

[101] J. Kozumplık and I. Provaznık. “Fast time-varying linear filters for suppression of baseline drift in electrocardiographic signals”. In: *Biomedical engineering online* 16.1 (2017), pp. 1–16.

[102] K.-M. Chang. “Arrhythmia ECG noise reduction by ensemble empirical mode decomposition”. In: *Sensors* 10.6 (2010), pp. 6063–6080.

[103] J. P. Martınez, R. Almeida, S. Olmos, A. P. Rocha, and P. Laguna. “A wavelet-based ECG delineator: evaluation on standard databases”. In: *IEEE Transactions on biomedical engineering* 51.4 (2004), pp. 570–581.

[104] M. Malik. “Heart Rate Variability: Standards of Measurement, Physiological Interpretation, and Clinical Use”. In: *Annals of Noninvasive Electrocardiology* 1.2 (1996), pp. 151–181.

[105] M. Brennan, M. Palaniswami, and P. Kamen. “Do existing measures of Poincare plot geometry reflect nonlinear features of heart rate variability?” In: *IEEE Transactions on Biomedical Engineering* 48.11 (2001), pp. 1342–1347.

[106] M. H. Hayes. *Statistical digital signal processing and modeling*. ISBN: 0-471 59431-8. New York: John Wiley and Sons, 1996.

[107] H. Akaike. “Fitting autoregressive models for prediction”. In: *Annals of the Institute of Statistical Mathematics* 21.1 (1969), pp. 243–247.

[108] E. Frank. “An accurate, clinically practical system for spatial vectorcardiography”. In: *circulation* 13.5 (1956), pp. 737–749.

[109] E. Prabhakararao and S. Dandapat. “Automated Detection of Posterior Myocardial Infarction From VCG Signals Using Stationary Wavelet Transform Based Features”. In: *IEEE Sensors Letters* 4.6 (2020), pp. 1–4.

[110] T. Ojala, M. Pietikäinen, and D. Harwood. “A comparative study of texture measures with classification based on featured distributions”. In: *Pattern recognition* 29.1 (1996), pp. 51–59.

[111] T. Ahonen, A. Hadid, and M. Pietikainen. “Face description with local binary patterns: Application to face recognition”. In: *IEEE transactions on pattern analysis and machine intelligence* 28.12 (2006), pp. 2037–2041.

[112] C. Shan, S. Gong, and P. W. McOwan. “Facial expression recognition based on local binary patterns: A comprehensive study”. In: *Image and vision Computing* 27.6 (2009), pp. 803–816.

[113] H. Moghaddasi and S. Nourian. “Automatic assessment of mitral regurgitation severity based on extensive textural features on 2D echocardiography videos”. In: *Computers in biology and medicine* 73 (2016), pp. 47–55.

[114] A. Balodi, R. Anand, M. Dewal, and A. Rawat. “Severity Analysis of Mitral Regurgitation Using Discrete Wavelet Transform”. In: *IETE Journal of Research* (2020), pp. 1–11.

[115] T. Ojala, M. Pietikainen, and T. Maenpaa. “Multiresolution gray-scale and rotation invariant texture classification with local binary patterns”. In: *IEEE Transactions on pattern analysis and machine intelligence* 24.7 (2002), pp. 971–987.

[116] S. Asgari, A. Mehrnia, and M. Moussavi. “Automatic detection of atrial fibrillation using stationary wavelet transform and support vector machine”. In: *Computers in biology and medicine* 60 (2015), pp. 132–142.

[117] N. Larburu, T. Lopetegi, and I. Romero. “Comparative study of algorithms for atrial fibrillation detection”. In: *2011 Computing in Cardiology*. IEEE. 2011, pp. 265–268.

[118] B. Weng, J. J. Wang, F. Michaud, and M. Blanco-Velasco. “Atrial fibrillation detection using stationary wavelet transform analysis”. In: *2008 30th Annual International Conference of the IEEE Engineering in Medicine and Biology Society*. IEEE. 2008, pp. 1128–1131.

[119] J. Rieta, J. Millet-Roig, V. Zarzoso, F. Castells, C. Sanchez, R. Garcia-Civera, and S. Morell. “Atrial fibrillation, atrial flutter and normal sinus rhythm discrimination by means of blind source separation and spectral parameters extraction”. In: *Computers in Cardiology*. IEEE. 2002, pp. 25–28.

[120] T. K. Ho. “A data complexity analysis of comparative advantages of decision forest constructors”. In: *Pattern Analysis & Applications* 5.2 (2002), pp. 102–112.

[121] A. Fernández, S. Garcıa, M. Galar, R. C. Prati, B. Krawczyk, and F. Herrera. *Learning from imbalanced data sets*. Vol. 10. Springer, 2018.

[122] J. Wang, Q. Chen, and Y. Chen. “RBF kernel based support vector machine with universal approximation and its application”. In: *International symposium on neural networks*. Springer. 2004, pp. 512–517.

[123] S. Petrutiu, A. V. Sahakian, and S. Swiryn. “Abrupt changes in fibrillatory wave characteristics at the termination of paroxysmal atrial fibrillation in humans”. In: *Europace* 9.7 (2007), pp. 466–470.

[124] N. Ortigosa, C. Fernández, A. Galbis, and Ó. Cano. “Phase information of time-frequency transforms as a key feature for classification of atrial fibrillation episodes”. In: *Physiological measurement* 36.3 (2015), p. 409.

[125] B. Safarbali and S. M. R. H. Golpayegani. “Nonlinear dynamic approaches to identify atrial fibrillation progression based on topological methods”. In: *Biomedical Signal Processing and Control* 53 (2019), p. 101563.

[126] M. A. Allessie, N. M. de Groot, R. P. Houben, U. Schotten, E. Boersma, J. L. Smeets, and H. J. Crijns. “Electropathological substrate of long-standing persistent atrial fibrillation in patients with structural heart disease: longitudinal dissociation”. In: *Circulation: Arrhythmia and Electrophysiology* 3.6 (2010), pp. 606–615.

[127] H. Moghaddasi et al. “Novel Rank-based Features of Atrial Potentials for the Classification Between Paroxysmal and Persistent Atrial Fibrillation”. In: *2022 Computing in Cardiology (CinC)*. Vol. 498. 2022, pp. 1–4. DOI: 10.22489/CinC.2022.326.

[128] J. Riccio et al. “Atrial fibrosis identification with unipolar electrogram eigenvalue distribution analysis in multi-electrode arrays”. In: *Medical & Biological Engineering & Computing* 60.11 (2022), pp. 3091–3112.

[129] V. Jacquemet et al. “Analysis of electrocardiograms during atrial fibrillation”. In: *IEEE Engineering in Medicine and Biology Magazine* 25.6 (2006), pp. 79–88.

[130] B. Abdi et al. “A compact matrix model for atrial electrograms for tissue conductivity estimation”. In: *Computers in Biology and Medicine* 107 (2019), pp. 284–291.

[131] J. W. de Vries et al. “Estimation of Cardiac Fibre Direction Based on Activation Maps”. In: *IEEE International Conference on Acoustics, Speech, and Signal Processing (ICASSP)* (2023).

[132] J. W. de Vries et al. *https://sps.ewi.tudelft.nl/Repository/repitem.php?id=44ti=16*. 2022. URL: https://sps.ewi.tudelft.nl/Repository/repitem.php?id=44&ti=16.

[133] H. Moghaddasi et al. “Tensor-based Detection of Paroxysmal and Persistent Atrial Fibrillation from Multi-channel ECG”. In: *2020 28th European Signal Processing Conference (EUSIPCO)*. IEEE. 2021, pp. 1155–1159.

[134] J. Pan and W. J. Tompkins. “A real-time QRS detection algorithm”. In: *IEEE Transactions on Biomedical Engineering* 3 (1985), pp. 230–236.

[135] J. Rissanen. “Modeling By Shortest Data Description”. In: *Automatica* 14.5 (1978), pp. 465–471.

[136] H. Akaike. “A New Look At The Statistical Model Identification”. In: *IEEE transactions on automatic control* (1974), pp. 716–723.

[137] L. De Lathauwer, B. De Moor, and J. Vandewalle. “A multilinear singular value decomposition”. In: *SIAM journal on Matrix Analysis and Applications* 21.4 (2000), pp. 1253–1278.

ACKNOWLEDGEMENTS

Since I have reached the end of my Ph.D. journey, I would like to take this opportunity to thank the people who have been a part of it and made it memorable.

First, I would like to thank my supervisors, Prof. Alle-Jan van der Veen, Prof. Natasja de Groot, and Dr. Borbála Hunyadi, for the opportunity they gave me to engage in this project. Alle-Jan, it was beyond my honor to work with you, enhancing my expertise in signal processing. I knew right after my first interview that I was eager to work with you. Every meeting with you was like a lesson that gave me valuable knowledge that would be helpful for the rest of my work. Besides the technical skills, I admire your positive attitude, fairness, and support, which made my Ph.D. unforgettable. Indeed, working with you was valuable in my personal and scientific growth. Natasja, I was a junior researcher in the field of cardiology when I started my Ph.D. Working with you as an expert cardiologist with a strong attitude helped me to learn and boost my knowledge in this field. I would like to thank you for all your support, constructive feedback, and help during these years. Bori, it was truly a pleasure to work with you. Over the years, I have recognized you as a strong woman in engineering who consistently has a clear vision of her goals and remarkable management skills. Thank you for all the freedom and support you gave me, which benefited my growth as a researcher. Furthermore, your biomedical viewpoint in our discussions helped me to value and grow more on this aspect of my work.

Also, I would like to thank Dr. Richard Hendriks for our nice collaboration and the valuable feedback you have given to me.

I also would like to thank my friends and colleagues who were with me on this journey. Bahareh Behboodi, you have been beyond a friend to me. I consider myself incredibly fortunate to have met you at high school and to have you as my lifelong friend. Although we live too far from each other, your unwavering presence in my life has provided me with comfort and support during the moments when I needed it most. Thank you for everything! Mario, you are truly a great person and friend! Thank you for all the help and support you have given to me. You are a perfect role model for being an independent researcher, and I learned a lot from that. I will always remember you said, "The stronger trees are those who take their time to grow." Taraneh, we passed through many difficulties in these years, supporting each other along the way. I am truly happy to have crossed paths with you. You became one of the most important people in my life. Elmira, from the first days of my arrival in the Netherlands, you became a friend I can always rely on and talk to about anything. Thank you for all your advice, kindness, incredible support, and for being a great friend of mine. To Taraneh, Richard, Hasti, and Mohammad, thank you for the great memories we made together and for becoming like our family in

the Netherlands.

Bahareh, Aydin, and Jamal, my Iranian friends in the office, thank you for all the great memories we have made together, full of fun and joy. Bahareh, I appreciate your help, guidance and kindness during these years. Aybüke and Tarik, thank you for all the support and help and for being our great friends. Aybüke, starting and ending the Ph.D. journey together with you made it memorable for me. It was great to meet you and become one of my best friends. Roxy, Maurits, and Nina thank you for all the wonderful and joyful moments we've experienced together. Roxy, it was great to meet you. From the very start of our friendship, it felt like we had known each other for ages. Your presence has made the Netherlands feel more like home to me. Nina, sweetheart, being your auntie is a great feeling. From the moment I was informed that I would become an auntie, I knew that my love for you would be boundless.

Alberto, Metin, and Anurodh, guys, you are amazing! Thank you for always being there for me and supporting me. Talking with you was always a relief. My office mates Didem, Sofia, and Miao, I really enjoyed our working environment and will miss you girls! Ellen, I appreciate all your positive attitude, help, and kindness. To all my friends at SPS, Seline, Giovanni, Yanbin, Costas, Ids, David, Changheng, Jordi, Ruben, Yanbo, Cristian, Yujie, Zhonggang, Peiyuan, and Isi, thank you for all the moments we spent together, dinners, hangouts, coffee breaks. I appreciate that you made SPS an enjoyable and fulfilling working place for me. Laura, I appreciate all your fast responses, management, and follow-ups, which made everything so smooth for everyone. SPS is so happy to have you! I also thank my old colleagues at CAS, Pim, Patrick, Elvin, Andreas, and Raj. Your company assisted me in becoming integrated into the group and learning the group culture; thanks, guys! Irma, thank you for all your kindness, care, and support and for teaching me Dutch traditions.

I also would like to thank my friends at the Erasmus MC. Jorik, Sanne, Nawin, and Eris, I appreciate all the happy moments, scientific discussions, and your efforts in teaching me Dutch. Not sure how much I was successful, though! Rohit, your help in answering my medical questions helped me enhance my understanding of this field; thank you! Mathijs, I appreciate all your efforts in data sharing and our scientific discussions. Paul, I appreciate the time you dedicated to data recording and helping me in testing the vest. To my EMC friends and colleagues, Ye, Lu, Annejet, Willemijn, Lianne, Can, Ljuba, Danny, Hongxian, Lisa, Mark, Chunsheng, and Marteen, it has been an incredible journey interacting with you, engaging in scientific discussions, and sharing moments throughout my Ph.D. studies.

Finally, I want to extend my heartfelt appreciation to my beloved family. To my mother and father, Rabieh and Mokhtar, thank you for the can-do attitude you grew in me. Feeling your unconditional love and support, always by my side, made me a strong person. To my brother, Hamed, thank you for all the encouragement, care, and support you have given to me. I'm so grateful for the bond we share and your presence in my life. To my uncle Ali, your thoughtful advice and insightful guidance have been invaluable in my decisions. I'm grateful for the positive impact your presence has had on my life. Your influence is truly appreciated! To my parents-in-law, Manizheh and Mansour, thank you for all the unwavering support

and love in these years. I'm so happy to have you as my second family. To my dear husband, Ali, I can't even imagine an end to this thesis without you. Thank you for your kindness, patience, support, and conscious guidance that you have always given to me. Having you encouraging me to follow my dreams makes all impossibles possible.

Hanie
The Hague, October 2023

CURRICULUM VITÆ

Hanie Moghaddasi was born in Ghazvin, Iran. She studied biomedical engineering in her B.Sc. and M.Sc. at the Amirkabir University of Technology, Tehran, Iran. During her master's program, she undertook a project focused on heart acoustic imaging using a microphone array, marking her first professional experience in signal processing and machine learning in the field of cardiology. In May 2019, she embarked on her Ph.D. journey, delving further into this field to study the progression of atrial fibrillation. She became part of a collaborative project between TU Delft and Erasmus MC. Currently, she is a postdoctoral researcher at the University of Oxford, the UK, where she works on a project entitled "Defining Translational Approaches for the Identification of Fetal Alcohol Spectrum Disorder". Her research interests are signal processing, image processing, and machine learning for biomedical pattern recognition. More specifically, she is passionate about enhancing computer-aided diagnosis algorithms to facilitate timely detection and treatment.